Functional connectomics reveals general wiring rule in mouse visual cortex

Zhuokun Ding[1-4,*], Paul G. Fahey[1-4,*], Stelios Papadopoulos[1-4,*], Eric Y. Wang[1], Brendan Celii[1,5], Christos Papadopoulos[1], Andersen Chang[1], Alexander B. Kunin[1,6], Dat Tran[1], Jiakun Fu[1], Zhiwei Ding[1], Saumil Patel[1-4], Lydia Ntanavara[1-4], Rachel Froebe[1-4], Kayla Ponder[1], Taliah Muhammad[1], J. Alexander Bae[7,8], Agnes L. Bodor[9], Derrick Brittain[9], JoAnn Buchanan[9], Daniel J. Bumbarger[9], Manuel A. Castro[7], Erick Cobos[1], Sven Dorkenwald[7,10], Leila Elabbady[9], Akhilesh Halageri[7], Zhen Jia[7,10], Chris Jordan[7], Dan Kapner[9], Nico Kemnitz[7], Sam Kinn[9], Kisuk Lee[7,11], Kai Li[10], Ran Lu[7], Thomas Macrina[7,10], Gayathri Mahalingam[9], Eric Mitchell[7], Shanka Subhra Mondal[7,8], Shang Mu[7], Barak Nehoran[7,10], Sergiy Popovych[7,10], Casey M. Schneider-Mizell[9], William Silversmith[7], Marc Takeno[9], Russel Torres[9], Nicholas L. Turner[7,10], William Wong[7], Jingpeng Wu[7], Wenjing Yin[9], Szi-chieh Yu[7], Dimitri Yatsenko[1,12], Emmanouil Froudarakis[1,13,14], Fabian Sinz[1,15,16], Krešimir Josić[17], Robert Rosenbaum[18], H. Sebastian Seung[7], Forrest Collman[9], Nuno Maçarico da Costa[9], R. Clay Reid[9], Edgar Y. Walker[19,20], Xaq Pitkow[1,5,21-23], Jacob Reimer[1,✉], and Andreas S. Tolias[1-4,5,24,✉]

[1]Department of Neuroscience & Center for Neuroscience and Artificial Intelligence, Baylor College of Medicine, Houston, TX, USA
[2]Department of Ophthalmology, Byers Eye Institute, Stanford University School of Medicine, Stanford, CA, USA
[3]Stanford Bio-X, Stanford University, Stanford, CA, USA
[4]Wu Tsai Neurosciences Institute, Stanford University, Stanford, CA, USA
[5]Department of Electrical and Computer Engineering, Rice University, Houston, USA
[6]Department of Mathematics, Creighton University, Omaha, USA
[7]Princeton Neuroscience Institute, Princeton University, Princeton, USA
[8]Electrical and Computer Engineering Department, Princeton University, Princeton, USA
[9]Allen Institute for Brain Science, Seattle, USA
[10]Computer Science Department, Princeton University, Princeton, USA
[11]Brain & Cognitive Sciences Department, Massachusetts Institute of Technology, Cambridge, USA
[12]DataJoint Inc., Houston, TX, USA
[13]Department of Basic Sciences, Faculty of Medicine, University of Crete, Heraklion, Greece
[14]Institute of Molecular Biology and Biotechnology, Foundation for Research and Technology Hellas, Heraklion, Greece
[15]Institute for Bioinformatics and Medical Informatics, University Tübingen, Tübingen, Germany
[16]Institute for Computer Science and Campus Institute Data Science, University Göttingen, Göttingen, Germany
[17]Departments of Mathematics, Biology and Biochemistry, University of Houston, Houston, USA
[18]Departments of Applied and Computational Mathematics and Statistics and Biological Sciences, University of Notre Dame, Notre Dame, USA
[19]Department of Neurobiology & Biophysics, University of Washington, Seattle, USA
[20]Computational Neuroscience Center, University of Washington, Seattle, USA
[21]Department of Computer Science, Rice University, Houston, TX, USA
[22]Neuroscience Institute, Carnegie Mellon University, Pittsburgh, PA, USA
[23]Department of Machine Learning, Carnegie Mellon University, Pittsburgh, PA, USA
[24]Department of Electrical Engineering, Stanford University, Stanford, CA, USA
[*]co-first author

Understanding the relationship between circuit connectivity and function is crucial for uncovering how the brain implements computation. In the mouse primary visual cortex (V1), excitatory neurons with similar response properties are more likely to be synaptically connected, but previous studies have been limited to within V1, leaving much unknown about broader connectivity rules. In this study, we leverage the millimeter-scale MICrONS dataset to analyze synaptic connectivity and functional properties of individual neurons across cortical layers and areas. Our results reveal that neurons with similar responses are preferentially connected both within and across layers and areas — including feedback connections — suggesting the universality of the 'like-to-like' connectivity across the visual hierarchy. Using a validated digital twin model, we separated neuronal tuning into feature (what neurons respond to) and spatial (receptive field location) components. We found that only the feature component predicts fine-scale synaptic connections, beyond what could be explained by the physical proximity of axons and dendrites. We also found a higher-order rule where postsynaptic neuron cohorts downstream of individual presynaptic cells show greater functional similarity than predicted by a pairwise like-to-like rule. Notably, recurrent neural networks (RNNs) trained on a simple classification task develop connectivity patterns mirroring both pairwise and higher-order rules, with magnitude similar to those in the MICrONS data. Lesion studies in these RNNs reveal that disrupting 'like-to-like' connections has a significantly greater impact on performance compared to lesions of random connections. These findings suggest that these connectivity principles may play a functional role in sensory processing and learning, highlighting shared principles between biological and artificial systems.

functional connectomics | visual cortex | digital twin | MICrONS
Correspondence: ***tolias@stanford.edu, reimer@bcm.edu***

Introduction

In the late 1800's, Santiago Ramón y Cajal — while poring over the structure of Golgi-stained neurons using only light microscopy — imagined the Neuron Doctrine, the idea that individual neurons are the fundamental units of the nervous system (Ramón y Cajal, 1911). Implicit in the Neuron Doctrine is the idea that the function of individual neurons — their role in what we would now call neural computation — is inextricably linked to their connectivity in neural circuits. A variety of influential proposals about the relationship between connectivity and function have been advanced in the past century. For example, Donald Hebb's cell assembly hypothesis (Hebb, 1949) — colloquially stated as "neurons that fire together, wire together" — predicted that

interconnected neuronal subnetworks "reverberate" to stabilize functionally relevant activity patterns. In the cortical visual system, Hubel and Wiesel proposed that the hierarchical organization of connected neurons might build more complex feature preferences from simpler ones; for example the position invariance of orientation-selective complex cells might be derived from convergent inputs of like-oriented simple cells with spatially scattered receptive fields (Hubel and Wiesel, 1962; Reid, 2012).

Testing these predictions has been difficult because of the challenges of measuring neural activity and synaptic-scale connectivity in the same population of neurons. In the mammalian visual cortex, evidence for several varieties of like-to-like connectivity (i.e. increased connectivity for cells with similar response preferences) has been found via spine imaging (Iacaruso et al., 2017), combined *in vivo* imaging and *in vitro* multipatching (Ko et al., 2011, 2013; Cossell et al., 2015; Znamenskiy et al., 2024), combined *in vivo* imaging and rabies monosynaptic retrograde tracing (Wertz et al., 2015; Rossi et al., 2020), and combined *in vivo* imaging with electron microscopy (EM) reconstruction (Lee et al., 2016; Scholl et al., 2021). However, a caveat of these important early studies is that they have mostly been limited to small volumes, usually single lamina of primary visual cortex (except see Wertz et al. 2015; Rossi et al. 2020), mostly due to the challenge of identifying synaptic connections between functionally-characterized neurons across distances larger than a few hundred microns. Thus, many questions remain unanswered about how these rules generalize across areas and layers.

The MICrONS dataset is the largest functionally-imaged EM dataset to date (MICrONS Consortium et al., 2021), with mesoscopic calcium imaging (Sofroniew et al., 2016) performed *in vivo* and subsequent EM imaging (Yin et al., 2020; Phelps et al., 2021) and dense reconstruction (Turner et al., 2020; Dorkenwald et al., 2022b; Mitchell et al., 2019; Lu et al., 2021; Wu et al., 2021; Dorkenwald et al., 2022a; Lee et al., 2017) for an approximately $1\,\mathrm{mm}^3$ volume spanning visual cortical areas V1, LM, AL, and RL in a single mouse. In contrast with previous studies that have selectively reconstructed presynaptic or postsynaptic partners of a small set of functionally-characterized target cells (Lee et al., 2016; Bock et al., 2011), the MICrONS volume is densely reconstructed, offering access to segmentation of all neurons in the volume, and enabling analyses that are not possible in targeted sparse reconstructions. Here, we take advantage of the dense reconstruction to compare the functional similarity of connected pairs with unconnected "bystanders" — pairs of neurons with closely-apposed axons and dendrites that had the opportunity to form synaptic connections, yet didn't.

Our analysis of functional similarity builds on recent advances in using machine learning to characterize the response properties of neurons in visual cortex. By training a neural network to replicate the responses of recorded neurons across a rich stimulus set of natural and parametric movies (Wang et al., 2024), we produce a "digital twin" of the cortical population which can accurately predict the response of a neuron to any arbitrary visual stimulus. The digital twin makes it possible to explore a much larger stimulus space with *in silico* experiments than would be possible (due to time constraints) with *in vivo* measurements (Wang et al., 2024). We have extensively validated this approach by looping back *in vivo* and validating model predictions of the most-exciting natural images and synthetic stimuli for a neuron (Walker et al., 2019). As part of the current study, we have validated the correspondence between model predictions and empirically-observed visual response properties, including signal correlations, orientation tuning, and spatial receptive field location. These validation results are described below. Finally, the digital twin model allowed us to separate each neuron's tuning into two components: a feature component (**what** the neuron responded to), and a spatial component (**where** the neuron's receptive field is located), allowing us to dissociate these two aspects of function and their relationship to connectivity.

Results

MICrONS functional connectomic dataset. Data were collected and processed as described in the MICrONS data release publication (MICrONS Consortium et al. 2021, Fig. 1). Briefly, a single mouse expressing GCaMP6s in excitatory neurons underwent fourteen two-photon scans (awake and headfixed on treadmill) of a $1200 \times 1100 \times 500\,\mu\mathrm{m}^3$ volume (anteroposterior $\times$ mediolateral $\times$ radial depth) spanning layers 2 through 6 at the conjunction of lateral primary visual cortex (V1) and anterolateral (AL), lateromedial (LM) and rostrolateral (RL) higher visual areas (Fig. 1a). Mice rapidly acclimated to head fixation, and were able to walk, groom, and adjust their posture during imaging. We monitored treadmill velocity and collected video of the pupil to track behavioral state. Neuronal responses from 115,372 functional units representing an estimated 75,909 unique excitatory neurons were collected in response to visual stimuli composed of natural and rendered movies and parametric dynamic stimuli (Fig. 1b). A state-of-the-art deep recurrent neural network was trained to predict neural responses to arbitrary stimuli (Wang et al., 2024), and used to characterize the *in silico* functional properties of imaged neurons (Fig. 1c).

After functional imaging, the tissue was processed for electron microscopy and imaged (Yin et al., 2020) at $4 \times 4 \times 40\,\mathrm{nm}^3$ resolution (Fig. 1a). The EM images were aligned (Mitchell et al., 2019) and automatically segmented using 3D convolutional networks into "atomic" supervoxels, which were agglomerated to create objects (e.g. neurons) with corresponding 3D meshes (Lee et al., 2017; Dorkenwald et al., 2022b; Lu et al., 2021; Wu et al., 2021; Dorkenwald et al., 2022a), and synapses were automatically detected and assigned to presynaptic and postsynaptic partners (Dorkenwald et al., 2022b; Turner et al., 2020; Wu et al., 2021). The analysis presented here is restricted to the overlap of "subvolume 65" (MICrONS Consortium et al., 2021) and the two-photon functional volume (Fig. 1a), an approximately $560 \times 1100 \times 500\,\mu\mathrm{m}^3$ volume (*in vivo* dimensions) that has been both densely functionally and structurally character-

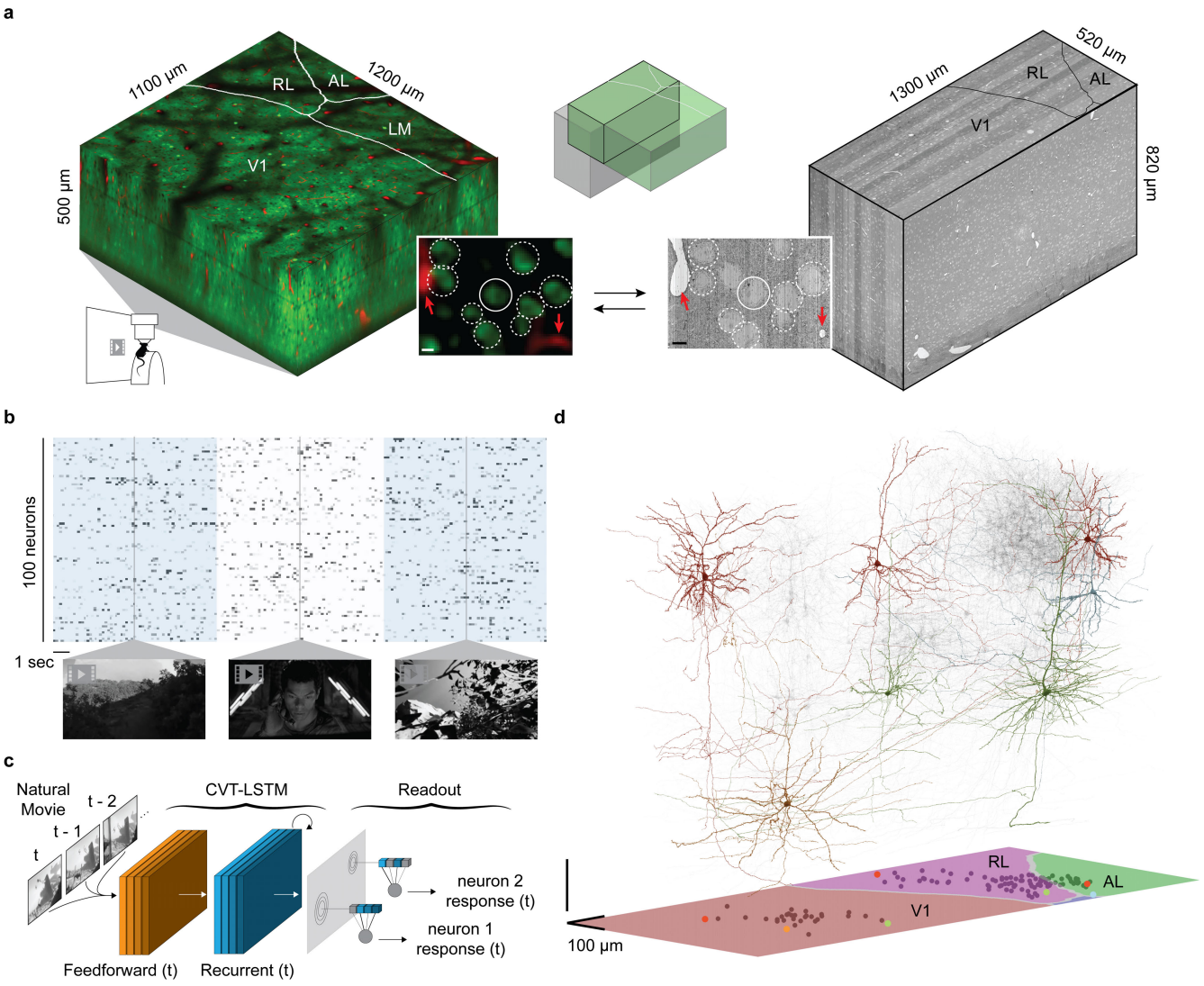

Figure 1. Overview of MICrONS Dataset. **a**, Depiction of functionally-characterized volumes (left; GCaMP6s in green, vascular label in red) and EM (right; gray). Visual areas: primary visual cortex (V1), anterolateral (AL), lateromedial (LM) and rostrolateral (RL).The overlap of the functional 2P (green) and structural EM (gray) volumes from which somas were recruited is depicted in the top inset. The bottom inset shows an example of matching structural features in the 2P and EM volumes, including a soma constellation (dotted white circles) and unique local vasculature (red arrowheads), used to build confidence in the manually assigned 2P-EM cell match (central white circle). All MICrONS data are from a single animal. Scale bars = $5\,\mu\mathrm{m}$. **b**, Deconvolved calcium traces from 100 imaged neurons. Alternating blue/white column overlay represents the duration of serial video trials, with sample frames of natural videos depicted below. Parametric stimuli (not pictured) were also shown for a shorter duration than natural videos. **c**, Schematic of the digital twin deep recurrent architecture. During training, movie frames (left) are input into a shared convolutional deep recurrent core (orange and blue layers, CVT=convolutional vision transformer, LSTM=long short-term memory) resulting in a learned representation of local spatiotemporal stimulus features. Each neuron is associated with a location (*spatial component* in the visual field (gray layer) to read out feature activations (shaded blue vectors), and the dot product with the neuron-specific learned feature weights (shaded lines, *feature component*) results in the predicted mean neural activation for that time point. **d**, Depiction of 148 manually proofread mesh reconstructions (gray), including representative samples from Layer 2/3 (red), Layer 4 (blue), Layer 5 (green), and Layer 6 (gold). Bottom panel: presynaptic soma locations relative to visual area boundaries.

ized. Of 82,247 automatically extracted neuronal nuclei in this subvolume, 45,334 were both classified as excitatory and located within the intersection of the EM reconstructed volume and functional volume.

The two-photon and EM volumes were approximately aligned (Fig. 1a, and 13,952 excitatory neurons were manually matched between the two volumes (Fig. 1a; MICrONS Consortium et al. 2021). Retinotopically-matched regions in V1 and higher visual areas AL and RL (together, HVA) were chosen to increase the likelihood of inter-area connections, and visually-responsive neurons within these regions were chosen for manual proofreading. Proofreading focused on extending axonal branches — with an emphasis on enriching projections across the V1/HVA boundary — and on removing false merges (instances where other somas, glia, axons, or dendrites were incorrectly merged into a neuron's reconstruction) (MICrONS Consortium et al. 2021, Supplemental Table 1). Postsynaptic partners of the proofread neurons were automatically cleaned of false merges with NEURD (Celii et al., 2024). In total, this resulted in a connectivity graph consisting of 148 functionally-characterized presynaptic neurons and 4811 functionally-characterized postsynaptic part-

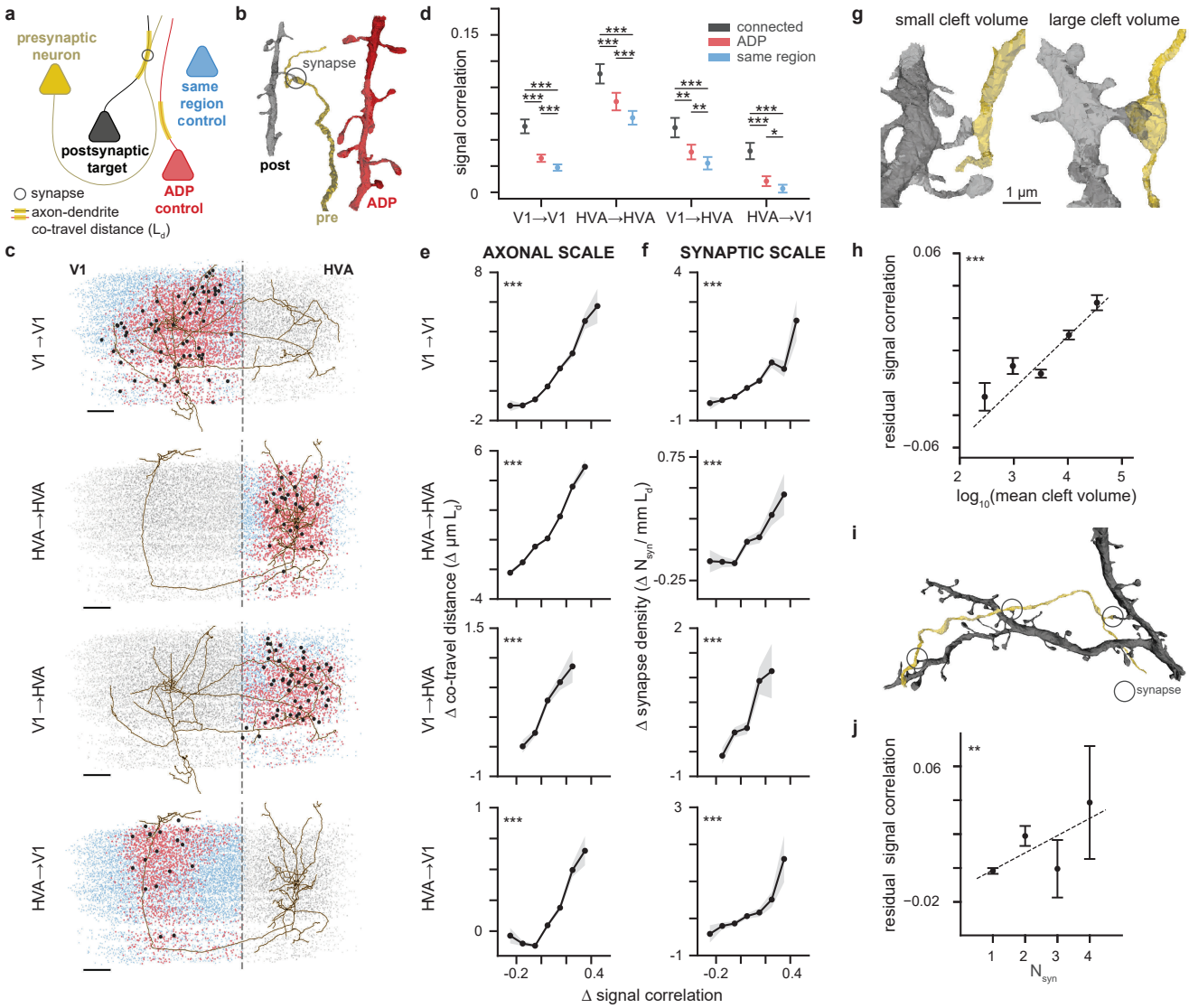

Figure 2. Neurons with higher signal correlation are more likely to form synapses. **a**, Schematic illustrating inclusion criteria for anatomical controls. For each proofread presynaptic neuron (yellow), control neurons for its true postsynaptic partners (black) are drawn either from unconnected neurons with non-zero axon-dendrite co-travel distance (Axonal-Dendritic Proximity ("ADP"), red), or unconnected neurons with zero axon-dendrite co-travel distance located in the same cortical region (blue). The axon-dendrite co-travel distance (L_d, yellow highlight on dendrites) is quantified as the total skeletal length of dendrite within 5 μm from any point on the presynaptic axon. A synapse is indicated with a gray circle. **b**, Representative meshes demonstrating a true presynaptic ("pre", yellow axon) to postsynaptic ("post", black dendrite) pair and an axonal-dendritic proximity control ("ADP", red dendrite). **c**, Presynaptic neuron axons plotted in EM cortical space for the four projection types (V1→V1, HVA→HVA, V1→HVA, HVA→V1) along with soma centroids of connected partners (black dots), ADP control neurons (red dots), same area control neurons (blue dots) and all other functionally matched neurons that are not used as controls (gray dots). The same presynaptic neuron is plotted for both the V1→V1 and V1→HVA group, and another neuron is used for both the HVA→HVA and HVA→V1 groups to demonstrate that a single presynaptic neuron can be represented in multiple projection types. Dashed line represents the boundary between V1 and HVA. Scale bar: $100\mu m$ **d**, Mean signal correlation is different (mean $\pm$ sem, paired t-test) between synaptically-connected partners (black), ADP controls (red), and same region controls (blue). This relationship was observed for within-area (V1→V1, HVA→HVA), feedforward (V1→HVA), and feedback (HVA→V1) connectivity. For details, see Supplemental Tab. 2 **e**, Axon-dendrite co-travel distance ($\mu m L_d$) increases in a graded fashion with signal correlation. ΔL_d and Δ signal correlation are the deviations from the mean for each presynaptic neuron. For reference, the mean L_d for each projection type is: V1→V1, $9.03\mu m$; HVA→HVA, $9.83\mu m$; V1→HVA, $4.17\mu m$; HVA→V1, $1.53\mu m$. For details of the analysis, see Supplemental Tab. 3, 5 The shaded regions are bootstrap-based standard deviations. **f** As in **e**, but with synapse density (N_{syn}/mmL_d). Synapse density increases in a graded fashion with signal correlation, for within-area (V1→V1, HVA→HVA), feedforward (V1→ HVA), and feedback (HVA→V1) connectivity. For reference, the mean N_{syn}/mmL_d for each projection type is: V1→V1, 1.12 synapses / mmL_d; HVA→HVA, 0.83 synapses / mmL_d; V1→HVA, 1.55 synapses / mmL_d; HVA→V1, 1.26 synapses / mmL_d. For details of the analysis, see Supplemental Tab. 4, 6 **g**, Representative meshes demonstrating synapses with small cleft volume (896 voxels, left) and large cleft volume (41716 voxels, right). **h**, Synapse size (log_{10} cleft volume in voxels) is positively correlated with signal correlation (p-values are from linear regression, residual signal correlation is obtained after regressing out the baseline effects on signal correlation due to differences in L_d). **i**, Representative meshes demonstrating a multisynaptic presynaptic (yellow) to postsynaptic (black) pair. **j**, Signal correlations increase with number of synapses (p-values are from linear regression, residual signal correlation is obtained after regressing out the baseline effects on signal correlation due to differences in L_d). (For all panels, $*$ = p-value < 0.05, $**$ = p-value < 0.01, $***$ = p-value < 0.001, multiple comparison correction by BH procedure)

ners (Fig. 1d).

Multi-tiered anatomical controls. Connectivity between neurons may be affected by numerous mechanisms, ranging from developmental processes that broadly organize neural circuits, to fine-scale plasticity mechanisms that modulate the strength of individual synaptic connections. The MICrONS

volume offers the opportunity to examine function-structure relationships at both of these scales. Because it is densely reconstructed, we not only know the distance between every pair of cell bodies in the volume, but also the relative geometry of their axons and dendrites. With this information, we can determine whether two neurons experience any fine-scale axon-dendrite proximities (ADP), with axon and dendrite coming within $5\mu m$ of each other. Furthermore, for neurons pairs with one or more ADP, we can compute the axon-dendrite co-travel distance L_d (Lee et al., 2016), a pairwise measurement which captures the total extent of postsynaptic dendritic skeleton within $5\mu m$ from any point on the presynaptic axonal skeleton.

With this metric in hand, we can define three cohorts of other neurons for functional comparisons with each presynaptic neuron (Fig. 2a-c, Supplemental Fig. 1). The first cohort are the connected postsynaptic targets of the presynaptic cell; these are neurons in the cortical region of interest that receive at least one synaptic input from the presynaptic neuron. The second group are "ADP controls", these are neurons with dendrites that come within striking range ($5\mu m$) of the presynaptic axon, but which don't actually form a synaptic connection. Finally, there are "same region controls" which are non-ADP neurons in the same cortical region (V1 or higher visual area). All connected neurons, ADP controls, and same region controls are restricted to visually responsive neurons with high-quality predictions from the digital twin (see Methods).

At the "axonal scale", we can ask how selective are axon trajectories within the volume, and whether neurons with axons and dendrites that meet and co-travel together have more similar tuning than nearby neurons that do not have any examples of axon-dendrite proximities. Selectivity at this scale could occur, for example, if a target cortical area has topographically-organized functional properties such as receptive field location (i.e. retinotopy) (Wang and Burkhalter, 2007; Garrett et al., 2014) or preferred orientation (Fahey et al., 2019; Ringach et al., 2016), and if axons preferentially target subregions with similar functional properties. In this case, we would expect functional properties between a presynaptic neuron and its ADP cohort to be more similar than random neurons selected from anywhere within the target region (same region control).

At the "synaptic scale", we can ask whether there is a relationship between functional properties and connectivity beyond the axonal scale — i.e. beyond what can be explained by the axonal trajectory and the spatial organization of functional properties within the volume. For this analysis, we compare the functional similarity between synaptically-connected neurons on the one hand, and unconnected ADP controls on the other, asking how frequently a certain amount of axon-dendrite co-travel distance is converted to a synapse. One hypothesis is that converting proximities to synapses is independent of the functional similarity between pre- and postsynaptic neurons. In this case, axon trajectories and axon-dendrite proximities would be sufficient to explain all of the observed connectivity between neurons ("Peter's rule") (Peters and Feldman, 1976; Braitenberg and Schüz, 2013; Rees et al., 2017). A competing hypothesis is that synapse formation and/or stabilization depends on the functional similarity between pre- and postsynaptic neurons. In this case, we might expect to find an additional boost in synaptic connections in similarly-tuned neurons *above and beyond* whatever selectivity already exists due to axonal trajectories and functional inhomogeneities in the volume. The densely-reconstructed MICrONS volume offers the first opportunity to distinguish between these two hypotheses at a scale spanning layers and areas.

Functional similarity is enhanced at both the axonal and synaptic scale. We tested the hypothesis of like-to-like connectivity in the context of signal correlations, a more general measure of functional similarity and a better predictor of connectivity in V1 L2/3 than orientation or direction tuning (Cossell et al., 2015). The digital twin was used to calculate the *in silico* signal correlation across a large battery of novel natural movies (250 ten-second clips). This approach was validated in a set of control experiments in a separate cohort of mice to ensure that the *in silico* signal correlation faithfully reproduced *in vivo* signal correlation measurements. In these control experiments, *in silico* signal correlations from the digital twin closely resembled the benchmark *in vivo* signal correlation matrix computed across a set of 30 movie clips each presented ten times, and in fact were more accurate than the *in vivo* signal correlation matrix computed with only six movie clips each presented ten times (which is the number of clips available in the MICrONS data, Supplemental Fig. 2). This excellent correspondence between *in vivo* and *in silico* signal correlation estimates was achieved even though none of the *in vivo* clips were used during training or testing of the digital twin.

For each proofread presynaptic neuron, we computed the mean signal correlation with postsynaptic neurons, ADP controls, and same region controls (Fig. 2d). We found that mean signal correlations were higher for connected neurons than both ADP and same region control groups, indicating that functional properties and connectivity are indeed related at the scale of individual synapses. Furthermore, signal correlations across pairs of neurons that experience at least one axon-dendrite proximity (ADP controls) were significantly higher than same region controls, indicating that there is also functional specificity at the axonal scale, with axons more likely to travel near dendrites of similarly-tuned neurons. These effects were independently observed when subsets of neuron pairs were considered within and across local V1 (V1 $\rightarrow$ V1), local HVA (HVA $\rightarrow$ HVA), feedforward (V1 $\rightarrow$ HVA) and feedback (HVA $\rightarrow$ V1) projection types (Fig. 2d, see Supp. Tab. 2 for details). In summary, we observed a functional "like-to-like" rule both at the level of axonal trajectories and for connectivity at the synaptic scale.

We explored this finding further, by asking whether there is a graded relationship between the amount of axon-dendrite co-travel distance and the corresponding boost in signal correlations (Fig. 2e).

For this analysis, to avoid confounding variability due to the

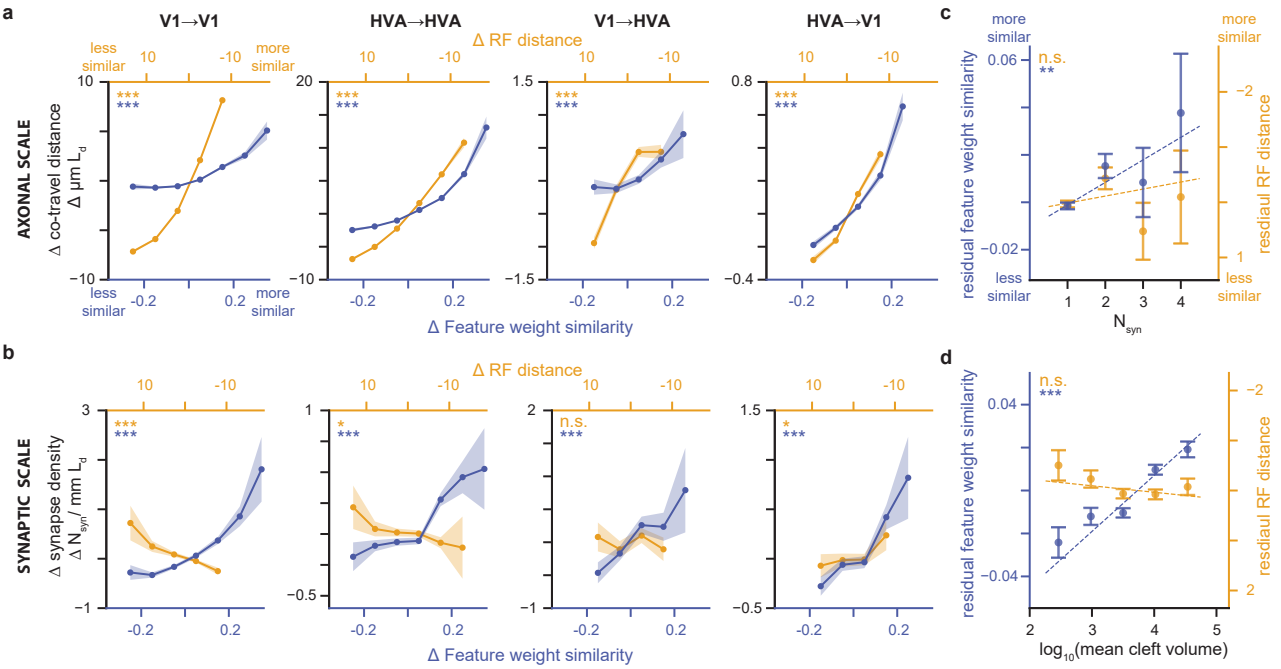

Figure 3. Feature weight similarity predicts synaptic selectivity better than receptive field center distance. **a**, Axon-dendrite co-travel distance increases with feature weight similarity and decreasing RF center distance for within-area (V1→V1, HVA→HVA), feedforward (V1→ HVA), and feedback (HVA→V1) connectivity. **b,**, Synapse density increases with feature weight similarity, but not with RF distance, except for HVAtoV1 projections. **c**, Multiple synapses are associated with increasing feature similarity, but not receptive field center distance, after regressing out L_d. **d,**, Only feature similarity (not receptive field center distance) is associated with an increase in cleft volume, after regressing out L_d. (For all panels, $*$ = p-value < 0.05, $**$ = p-value < 0.01, $***$ = p-value < 0.001, p-values are corrected for multiple comparisons using BH procedure, for details, see Supplemental Tab. 11, 13, 15, 17, 12, 14, 16, 18,)

size of each presynaptic neuron's axonal arbor and their varying mean signal correlations, for each presynaptic neuron we first computed the mean L_d and mean signal correlations across all of its ADP targets and same region control neurons. Then for each of the pairwise comparisons, we subtracted the pre-computed mean and kept only the difference from the mean for each metric. This approach has the effect of centering both the x- and y-axes in Fig. 2e (and also 2f), in order to focus on the relative effect within each presynaptic neuron and its downstream partners, removing neuron-to-neuron variability in both metrics.

Binning these differences revealed that longer-than-average L_d between a presynaptic neuron and a downstream target was associated with higher-than-average signal correlation between the two neurons. This result was significant when repeated across all projection types, and indicates that the axons and dendrites of neurons with more similar functional properties are likely to meet more often and/or travel farther together in the volume, and there is a graded relationship in this effect that is observed both within and across cortical areas.

We next performed a similar analysis for synapses, looking at connected neuron pairs. For each presynaptic neuron we first computed the mean number of synapses per millimeter of co-travel distance (synapse density, N_{syn}/mmL_d), along with mean signal correlations across all pairs of synaptic and ADP targets. Then for each of these pairwise comparisons for a single presynaptic neuron, we subtracted the mean and kept only the difference from the mean. After centering on the means for each presynaptic cell in this way, the binned differences again revealed a strong graded relationship between synaptic connectivity and functional similarity (Fig. 2f). Specifically, higher-than-average rates of synaptic density (synapses per unit co-travel length) were associated with higher-than-average functional similarity, again in a graded fashion.

Given this relationship between synapse frequency and functional similarity, we wondered whether there might be a relationship between functional similarity and either synapse size (a proxy for synaptic strength; (Holler et al., 2021)) and/or the multiplicity of synaptic connections between two neurons. Indeed, previous studies have found that functionally-similar presynaptic-postsynaptic pairs have stronger synaptic connections (Cossell et al., 2015) and larger postsynaptic densities (PSDs) (Lee et al., 2016). In the MICrONS dataset, segmented synapses were automatically annotated with the cleft volume, which is positively correlated to spine head volume, PSD area, and synaptic strength (Celii et al., 2024; Holler et al., 2021; Dorkenwald et al., 2022b) (Fig. 2g).

We found that signal correlation positively correlates with cleft volume (Fig. 2h; r = 0.032, p < 0.001). Looking at the multiplicity of connections between neurons (the number of individual synapses connecting two cells), we also found that presynaptic-postsynaptic pairs with multiple synapses also had higher signal correlations (Fig. 2i, j) when compared to monosynaptic pairs. In both Fig. 2h, j, the synaptic scale effect is isolated by regressing out the contribution of L_d to signal correlation. In summary, both the strength

(synaptic volume) and multiplicity of connections are higher when neurons are more functionally similar, consistent with an underlying Hebbian plasticity mechanism that might act to strengthen and stabilize connections between jointly-active neurons.

Lastly, to ensure the robustness of these findings, we ran the same analyses above with signal correlations measured directly from *in vivo* responses (rather than from the digital twin) and found that they replicated the like-to-like results achieved using the *in silico* signal correlations — including the graded relationships at the axonal and synaptic scale, and the relationships with synaptic cleft volume and synapse multiplicity (Supplemental Fig. 3).

Factorized *in silico* functional representation. A key advantage of the digital twin (Fig.1c, Wang et al. 2024) is the factorization of each modeled neuron's predicted response into two factors: readout **location** in visual space—a pair of azimuth/altitude coordinates; and readout **feature weights**—the relative contribution of the core's learned features in predicting the target neuron's activity. Intuitively, these learned features can be thought of as the basis set of stimulus features that the network then weighs to predict the neural responses. For each neuron, the combination of feature weights ("what") and receptive field location ("where") together encode everything the model has learned about that neuron's functional properties, and enable the model's predictive capacity for that neuron. This factorized representation allowed us to examine the extent to which these two aspects of neural selectivity independently contribute to the relationship between signal correlation and connectivity we observed in Fig. 2. Feature weight similarity was measured as the cosine similarity between the vectors of presynaptic and postsynaptic feature weights. Receptive field (RF) location similarity was measured as the visual angle difference between the center of the model readout locations, with lesser distance between the centers ("center distance") corresponding to greater location similarity. We conducted a separate series of experiments to validate the model's readout location as an estimate of RF center. These experiments demonstrated that the readout location correlates strongly with receptive field centers measured using classical sparse noise (dot-mapping) stimuli (Supplemental Fig.4a, b). Moreover, our approach outperformed classical linear *in vivo* measurements of the spatial receptive field for the significant fraction of neurons that are not responsive to the dot-mapping stimuli, even with one hour of dot-mapping data (Supplemental Fig.4c).

Both RF location similarity and feature weight similarity increase with axon-dendrite co-travel distance. Among pairs of neurons with at least one axon-dendrite proximity (ADP neurons), axon/dendrite co-traveling for longer-than-average distances was associated with higher-than-average feature similarity (Fig. 3a). Similarly, neurons with higher-than-average receptive field similarity (i.e. receptive fields closer to each other), also co-traveled for longer-than-average distances. Thus, both feature tuning and receptive field location are positively correlated with the extent of axon-dendrite proximity between pairs of neurons, and these relationships held both within and across cortical areas. This result is consistent with a scenario where axonal projections are enriched in downstream regions with similar tuning properties, either via axon guidance cues during development or via selective stabilization of axons in areas with similar functional properties, or both.

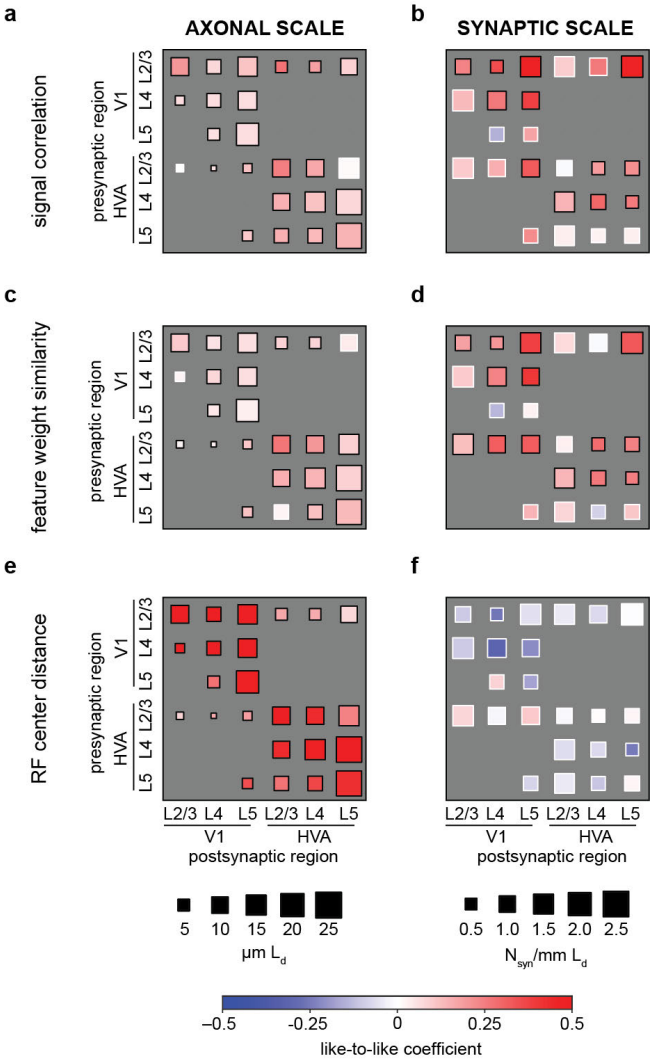

Figure 4. Like-to-like effects are widespread but vary across brain areas, cortical layers, and tuning similarity metrics. a-f, Degree of like-to-like broken down by area and layer membership measured at axonal (**a, c, e**) and synaptic scales (**b, d, f**). Colorbar: like-to-like coefficients, red is more like-to-like. For axonal scale, box size represents axon-dendrite co-travel distance ($\mu m L_d$). For synaptic scale, box size represents synapse density ($N_{syn}/mm L_d$). Like-to-like coefficients are the coefficients of GLMMs fitted to predict axon-dendrite co-travel distance or synapse density with the corresponding functional similarity. (black border = significant at p-value < 0.05, white border = p-value > 0.05, by Wald test after BH correction for multiple comparisons, for details see Supplemental Tab. 26, 25, 28, 27, 30, 29).

A like-to-like rule for feature similarity, but not spatial RF location, is observed at the scale of individual synapses. In contrast with the functional similarity in both features and RF locations associated with axon-dendrite proximity, synaptic connectivity between neurons was only positively correlated with similarity in feature preferences (Fig. 3b). Receptive field location similarity was either not

correlated with synapse density or — in the case of V1 — was anti-correlated. Thus, at the synaptic scale, only like-to-like feature preference (not smaller spatial RF center distance) is associated with increased synaptic connectivity. This is a prominent difference between axonal-scale and synaptic-scale relationships with function, and suggests that Hebbian plasticity mechanisms operating at the level of individual synapses are driven by feature similarity rather than receptive field center distance. Consistent with this view, both synapse multiplicity (Fig. 3c) and synaptic cleft volume (Fig. 3d) strongly increase with feature similarity rather than RF location similarity (after regressing out L_d as for Fig. 2h, j).

Like-to-like rule generalizes across joint layer and area membership of cells. To achieve a more detailed understanding of the organization of connections across layers and areas, for each functional similarity metric (signal correlation, feature weight similarity, and receptive field center distance), we also tested the relationship with connectivity across two areas (primary visual cortex, V1; higher visual areas AL and RL, HVA) and three layers (L2/3, L4, and L5, Fig. 4). For signal correlation (Fig. 4a, b, see Supplemental Tab. 25, 26 for details) and feature weight similarity (Fig. 4c, d, see Supplemental Tab. 27, 28 for details), like-to-like effects (red squares) were widespread across many area and layer combinations, at both the axonal and synaptic scale.

In the case of RF center distance, while like-to-like effects (red squares) were widespread at the axonal scale, these effects disappeared when considering synaptic-scale specificity. This finding is consistent with the view that selectivity for retinotopic overlap exists at the scale of axon trajectories but not at the scale of individual synapse formation (Fig. 4e, f, see Supplemental Tab. 29, 30 for details). In this analysis, individual presynaptic baselines (e.g. variable L_d, synapse rate, signal correlation), were accounted for with a generalized linear mixed model (GLMM) (see Methods for details). Distributions of all pairwise functional measurements, including *in vivo* signal correlation, *in silico* signal correlation, feature weight similarity, and receptive field distance are provided in Supplementary Fig. 10. Varying the inclusion thresholds of the above analyses across varying levels of digital twin model performance (quartiles of neurons ranked by prediction accuracy) did not substantially change the main results (Supplementary Fig. 11).

Orientation tuning is like-to-like within V1 at both axonal and synaptic scales. Many neurons in mouse primary visual cortex and higher visual areas are strongly tuned for orientation, and a number of previous functional connectivity studies have used differences in preferred orientation as a metric for visual similarity within V1. In order to compare our findings more directly with this previous work, we repeated the central analysis in Fig. 2, but now using only the difference in preferred orientation — rather than signal correlations — to determine functional similarity.

We used the digital twin to estimate orientation tuning, and we validated this approach with *in vivo* validation experiments (Supplemental Fig. 7a, b), where we compared the

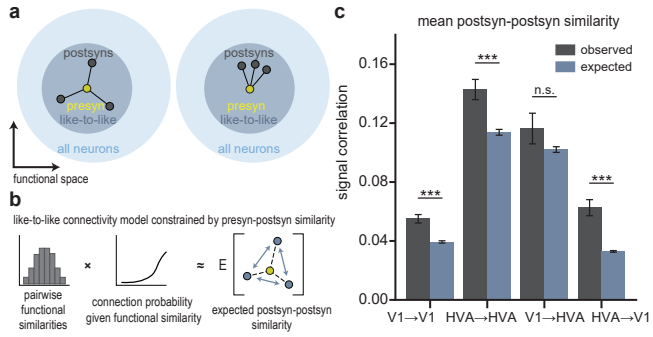

Figure 5. Postsynaptic neurons with a common input are more functionally similar to each other than expected from a pairwise like-to-like rule. **a**, Left: Schematic illustrating the null hypothesis that postsynaptic neurons (gray circles, "postsyns") of a common presynaptic neuron (yellow circle, "presyn") have no additional feature similarity with each other beyond their like-to-like similarity with their common presyn. In this scenario, postsyns are distributed uniformly around the presyn in the "like-to-like" region of functional space (dark blue region). Right: Schematic illustrating the alternative hypothesis that the postsynaptic neurons are closer in functional space than predicted from a pairwise like-to-like rule, equivalent to being clustered non-uniformly within the "like-to-like" region. **b**, Schematic illustrating the functional connectivity model used to simulate the null hypothesis in **a**. Pairwise functional measurements (left) — including signal correlations, feature weight similarity and receptive field location distance — were passed through a function relating functional similarity to connection probability. Then, within this modeled network, we computed the pairwise similarity of all postsyns downstream of a common presyn (right). In **c**, we compare the actual postsynaptic functional similarity we observed in the data (black) to the expected postsyn similarity as determined from the model (blue). In three out of four area comparisons, we find that postsyns are significantly more similar to each other than expected from a pairwise like-to-like rule.

in silico orientation tuning curve with the tuning curve estimated from the *in vivo* data. Orientation-selective responses were driven by lowpass filtered noise with coherent orientation and motion, a stimulus we have previously used to drive strong visual responses in orientation-tuned cells (Fahey et al., 2019; Wang et al., 2024). For orientation-tuned neurons (gOSI > 0.25, corresponding to more that 50% of co-registered neurons; please see methods for gOSI versus OSI comparison), the *in silico* orientation tuning curves align extraordinarily well with *in vivo* orientation tuning curves (Supplemental Fig. 7c-f).

We found that connected neurons in V1 have more similar orientation tuning than unconnected controls (Supplemental Fig. 8), as reported by previous studies (Rossi et al., 2020; Ko et al., 2011; Lee et al., 2016). However, in contrast with previous studies, we did not observe a similar significant like-to-like effect when restricting the analysis specifically to projections within V1 L2/3 excitatory neurons. To understand this deviation from previous literature, we first determined that connected neuron pairs within V1 L2/3 projections in the MICrONS dataset did indeed have similar orientation preferences (Supplemental Fig. 9), as expected. However, unconnected pairs showed the same level of similarity in orientation preference. We believe this is the result of a local orientation bias where the MICrONS volume is located in V1 (Fahey et al. 2019).

Overall, we found that the model feature weight similarity is a better predictor of connectivity than classical orientation preference, even for neurons tuned to oriented stimuli (Supplemental Fig. 6). Recent work by our group and others has

emphasized that optimal stimuli for neurons in mouse V1 can exhibit complex spatial features that deviate strikingly from Gabor-like stimuli (Walker et al., 2019; Tong et al., 2023). These results highlight the advantages of studying more complete tuning functions, such as the model feature weights that we focus on here, rather than single tuning parameters such as orientation preference.

Neurons with common input are functionally similar. If the pairwise "like-to-like" rule were the sole organizing principle of the visual cortex — implying that all postsynaptic neurons closely resemble their presynaptic partners — we would expect postsynaptic neurons to exhibit a certain degree of similarity to one another.

However, neural feature selectivity likely arises from more complex connectivity rules, so a cohort of neurons downstream of a single presynaptic neuron might, on average, be less (Fig. 5a, left) or more functionally similar to each other (Fig. 5a, right). To evaluate whether the similarity among postsynaptic neurons differs from what the "like-to-like" rule predicts, we built a simple model network, and introduced the empirical relationships between presynaptic/postsynaptic functional similarity and connectivity that we observed in our data. Specifically, we replicated the empirical distribution of signal correlations, feature weight similarities, and receptive field location distances over all model neuron pairs, and then predicted the expected number of synapses between neuron pairs — based on their functional similarity — with a Poisson linear mixed-effects model (Fig. 5b). We confirmed that this model replicated the expected functional similarity between connected neurons, indicating that it accurately captured the same pairwise "like-to-like" rule that we observed in the data (Supplemental Fig. 5). Then, we measured the similarity among all postsynaptic neurons downstream of a single presynaptic neuron, by calculating the mean pairwise signal correlations. As expected, on average, postsynaptic neurons were more functionally-similar to other postsynaptic neurons than random pairs (Supplemental Fig. 5). However, we also found that postsynaptic neurons receiving common synaptic inputs in the MICrONS dataset were even more similar than the "like-to-like" model predicted (Fig. 5c). These relationships held when tested at both axonal and synaptic scales for three out of the four projection types (Supplemental Fig. 5). This suggests the existence of higher-order functional organization beyond the simple pairwise relationships that we focused on up to this point.

Like-to-like connectivity and its functional role in artificial neural networks. A possible functional role for the like-to-like connectivity observed in our data is suggested by theoretical work on recurrent neural network (RNN) models, starting with early work on attractor-based models like Hopfield networks (Hopfield, 1982; Khona and Fiete, 2022a). In these models, like-to-like connectivity increases similarity in neural responses to similar stimuli, which aids both supervised and unsupervised learning. Artificial neural networks produce stimulus representations similar to those in primary visual cortex (Yamins et al., 2014; Cadena et al., 2019), but there have been no comparisons to date between like-to-like connectivity in biological and artificial neural networks.

To make such a comparison, we trained an RNN model on a simple image classification task (Fig. 6a; see Methods for details). The trained RNN showed increased like-to-like connectivity compared to the same model before training (Fig. 6b,c), and a small shift in the distributions of signal correlations, similar to those in our data (Supplementary Figs. 10 and 12). Intriguingly, we found that ablating like-to-like connections in the trained model decreased performance more than ablating random connections with the same connection strengths (Fig. 6d), suggesting that like-to-like connectivity plays a functional role in the model. Finally, we found that the trained model exhibits an increase in signal correlations within cohorts of postsynaptic cells defined by a shared presynaptic neuron, similar to the higher order connectivity rule that we observed in our data. (Fig. 6e). These results suggest that like-to-like connectivity — similar to the magnitude we observed in the MICrONS data — could be sufficient to subserve a functional role in sensory processing and learning.

Discussion

Discovering the principles that relate structure to function is central in the pursuit of a circuit-level mechanistic understanding of brain computations. Here, we used the MICrONS multi-area dataset — the largest of its kind — to study the relationship between the connections and functional responses of excitatory neurons in mouse visual cortex across cortical layers and visual areas. Our findings revealed that neurons with highly correlated responses to natural videos (i.e. high signal correlations) tended to be connected with each other, not only within the same cortical areas but also across multiple layers and visual areas, including feedforward and feedback connections. While the overall principle of “like-to-like” connectivity that we describe here is consistent with a number of previous studies (Ko et al., 2011, 2013; Wertz et al., 2015; Lee et al., 2016; Rossi et al., 2020), our work leverages three unique strengths of the MICrONS dataset to extend and refine these previous findings.

First, the **scale of the volume** enabled us to look at connection principles across layers 2-5 of cortex, not just within V1, but also in projections between V1 and higher visual areas. In agreement with previous findings from V1 L2/3, we found that pairs of cells with higher signal correlations were more likely to be connected (Ko et al., 2011, 2013; Cossell et al., 2015). This general principle held not just in V1 L2/3, but also in higher visual areas and for inter-area feedforward and feedback projections.

Second, we were able to take advantage of the **dense reconstruction** to ask questions about functional specificity at the axonal scale that would be difficult to address with any other data. We found that axons are more likely to co-travel with dendrites of similarly-tuned neurons, even for long-range axons spanning areas. The dense reconstruction also allowed us to compute a set of null distributions for the expected synaptic connectivity between neurons based on axon-

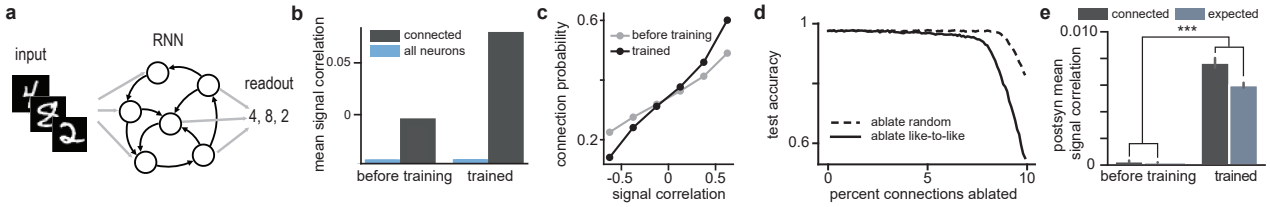

Figure 6. Like-to-like connectivity in an RNN. a, A vanilla RNN was provided images as inputs and weights were trained so that a readout of the final state identifies the input's label. **b**, Mean signal correlations among all (blue) and connected (black) neuron pairs for the same RNN before (left) and after (right) training. Neurons were classified as connected when their weights exceeded a fixed threshold. **c**, Connection probability as a function of signal correlation for the same network before (gray) and after (black) training. **d**, Test accuracy of the network as a function of the number of connections ablated when ablating random (dashed) or like-to-like (solid) connections. Connections were classified as like-to-like whenever the weight and signal correlation both exceeded a fixed threshold. **e**, Mean post-post signal correlations and the expected post-post signal correlation given a pairwise model similar to Fig. 5c before and after training.

dendrite proximities. These controls enable us to distinguish whether the relationships we observed between connectivity and function are due to the overall geometry of axonal and dendritic arbors in the volume, or whether they reflect a more precise connectivity rule at the level of individual synapses. For example, it is only with the inclusion of both same region and ADP controls that we are able to observe the diverging findings of axon trajectory level selectivity for receptive field center distance (Fig. 3 d, e, f) and synaptic level selectivity for feature weight similarity (Fig. 3 a, b, c). These different controls can be mapped onto potential developmental or adult plasticity mechanisms that may shape the coarse axon trajectory and fine-scale synaptic connectivity across the brain.

Finally, our **deep learning neural predictive modeling approach** enabled us to comprehensively characterize the tuning function of a neuron, factorize it into spatial and feature tuning components, and facilitate *in silico* exploration with neural responses to novel visual stimuli. The digital twin model allowed us to measure signal correlations over a much larger set of naturalistic videos, resulting in better connectivity predictions compared to *in vivo* measurements from a smaller stimulus set (Supplemental Fig. 6). Moreover, the model's factorized architecture provided a unique opportunity to discover distinct synaptic organizing principles for two interpretable components of neuronal tuning: what the neuron is tuned to and where its receptive fields are located. Notably, the digital twin model demonstrated excellent out-of-training-set performance (Supplemental Fig. 2) even for novel stimulus domains (Supplemental Fig. 4). This generalization ability opens exciting possibilities for future *in silico* visual experiments, although validation experiments remain essential when studying the digital twin model with new stimulus domains. Currently we treat this model as a black box, but future models could constrain the architecture in order to make internal model parameters more interpretable. Additionally, recent studies have shown that behavioral states and task variables explain a substantial portion of neural responses, even in sensory cortices (Stringer et al., 2019; Musall et al., 2019). Future digital twins could incorporate additional behavioral measurements that enable us to study more general relationships between structure and function, beyond visual processing.

Many of the analyses described in this paper evaluated pairwise relationships between one presynaptic neuron and one postsynaptic or control neuron. While our experiment in an RNN toy model shows that a pairwise like-to-like rule can have important functional consequences for task performance (Fig. 6), there is still a question of whether there exist higher-order functional motifs beyond simple, pairwise relationships. We explored one such higher-order pattern in our analysis of functional similarity among postsynaptic neurons sharing at least one common input (Fig. 5). This investigation revealed functionally similar postsynaptic cohorts, suggesting the presence of more complex organizational principles. Other studies have looked at functional similarity in presynaptic cells converging on a single common postsynaptic neuron (Bock et al., 2011; Wertz et al., 2015; Rossi et al., 2020). As proofreading in the MICrONS volume continues, it will become possible to test motifs of much higher order and complexity and their relationship to more complex functional properties. In addition to a more complete connectivity graph, another route to discovery may be to study more richly-colored graphs that include additional modalities about each neuron, including features such as morphological or transcriptomic information, or local ultrastructure. Alternatively, it may be important to investigate functional connectivity rules operating at the scale of sub-cellular compartments, for example looking at synapse clustering on dendrites.

Just as pairwise relationships might only partially reveal rules at play in higher-order motifs, the principle of "like-to-like" may only partially capture more complicated principles relating structure and function. For example, Wertz et al. found that for some networks (multiple presynaptic neurons converging onto a single postsynaptic output), the similarity of inputs differed depending on layer origin, a phenomenon they termed "feature-variant" networks (Wertz et al., 2015). Several studies have also found that there is an interplay between the geometric relationship of receptive field positions and feature preferences (Rossi et al., 2020; Marques et al., 2018; Oldenburg et al., 2024). For example, Rossi et al. found that the spatial offset between the receptive fields of excitatory and inhibitory inputs matched the postsynaptic cell's direction selectivity (Rossi et al., 2020). Future work could further discriminate along the relevant feature dimensions to find more precise rules.

Like-to-like connectivity is a recurring theme in theoretical models of neural circuit function, including Hebb's theory of

neural assemblies (Hebb, 1949), Hubel and Wiesel's theory of receptive field formation (Hubel and Wiesel, 1962), and later work by Hopfield (Hopfield, 1982) and others (Khona and Fiete, 2022b) on attractor based models. Like-to-like connectivity is often assumed *a priori* or emerges due to Hebbian plasticity in these models, but our analysis of a vanilla RNN trained by gradient descent shows that like-to-like connectivity — in addition to higher order connectivity motifs observed in our data — can arise naturally from optimizing a recurrent system for a simple visual task (Fig. 6). Theory-driven experiments will allow us to move beyond correlational to causal understanding of biological systems. Future works could study these connectivity rules further in artificial systems with greater complexity or biological realism.

Our work provides a first glimpse of principles of cortical organization that can be discovered with large datasets combining detailed functional characterization with synaptic-scale connectivity. While the incredible accuracy of machine learning-based reconstruction methods has rightly increased optimism about the potential discoveries that can be made from large EM volumes — especially when combined with functional characterization — we should also not forget the magnitude of the challenge contained in even a $1\,\mathrm{mm}^3$ volume of cortex in a single mouse. The analyses in this paper are based on only a small number of manually proofread neurons, but even this limited view of the dataset represents an impressive volume of axonal and dendritic reconstruction. Ongoing investments in proofreading, matching, and extension efforts within this volume will have exponential returns for future analyses as they yield a more complete functional connectomic graph, and reduce or eliminate potential biases in the connections. As more large-scale datasets like MICrONS are publicly released, there will be much more to discover about the organizing principles relating structure and function in other brain areas (Kuan et al., 2024) and even other model organisms (Wanner et al., 2016). Our hope is that this dataset, including both the structural anatomy and the immortalized digital twin for ongoing *in silico* experiments, will be a community resource that will yield concrete insights as well as inspiration about the scale of investigation that is now possible in neuroscience.

ACKNOWLEDGEMENTS

The authors thank David Markowitz, the IARPA MICrONS Program Manager, who coordinated this work during all three phases of the MICrONS program. We thank IARPA program managers Jacob Vogelstein and David Markowitz for co-developing the MICrONS program. We thank Jennifer Wang, IARPA SETA for her assistance.

The work was supported by the Intelligence Advanced Research Projects Activity (IARPA) via Department of Interior/ Interior Business Center (DoI/IBC) contract numbers D16PC00003, D16PC00004, and D16PC0005. The U.S. Government is authorized to reproduce and distribute reprints for Governmental purposes notwithstanding any copyright annotation thereon. XP acknowledges support from NSF CAREER grant IOS-1552868. ZD, SP, RR, KJ, XP, and AST acknowledge support from NSF NeuroNex grant 1707400. AST, XP, KJ, and JR are supported by RF1 MH130416. AST acknowledges support from National Institute of Mental Health and National Institute of Neurological Disorders And Stroke under Award Number U19MH114830 and National Eye Institute award numbers R01 EY026927 and Core Grant for Vision Research T32-EY-002520-37. ABK acknowledges support from a training fellowship from the Gulf Coast Consortia, on the NLM Training Program in Biomedical Informatics & Data Science (T15LM007093). RR acknowledges support from Air Force Office of Scientific Research (AFOSR) award number FA9550-21-1-0223. Disclaimer: The views and conclusions contained herein are those of the authors and should not be interpreted as necessarily representing the official policies or endorsements, either expressed or implied, of IARPA, DoI/IBC, or the U.S. Government.

AUTHOR CONTRIBUTIONS

We adopted the following contribution categories from CRediT (Contributor Roles Taxonomy). Authors within each category are sorted in the same order as in the author list.

Conceptualization: ZhuD, PGF, StP, XP, JR, AST
Methodology: ZhuD, PGF, StP, ErYW, BC, CP, AC, DY, EF, KJ, RR, EdYW, AST
Software: ZhuD, PGF, StP, ErYW, BC, CP, DY, EF, RR
Validation: ZhuD, PGF, StP, ErYW
Formal analysis: ZhuD, PGF, StP, AC, ABK, RR
Investigation: ZhuD, PGF, StP, ErYW, SaP, JF, ZhiD, KP, TM, RR
Resources: PGF, StP, SaP, JAB, ALB, DB, JB, DJB, MAC, EC, SD, LE, AH, ZJ, CJ, DK, NK, SK, KiL, KaL, RL, TM, GM, EM, SSM, SM, BN, SeP, CMSM, WS, MT, RT, NLT, WW, JW, WY, SY, DY, EF, FS, RR, HSS, FC, NMdC, RCR, XP, JR, AST
Data Curation: ZhuD, PGF, StP, BC, CP, ZhiD
Writing - Original Draft: ZhuD, PGF, StP, ErYW, RR, JR
Writing - Review & Editing: ZhuD, PGF, StP, AC, JF, SaP, CMSM, KJ, RR, FC, NMdC, RCR, EdYW, XP, JR, AST
Visualization: ZhuD, PGF, StP, RR
Supervision: PGF, XP, JR, AST
Project administration: ZhuD, PGF, StP, JR, AST
Funding acquisition: HSS, FC, NMdC, RCR, XP, JR, AST

COMPETING FINANCIAL INTERESTS

XP is a co-founder of UploadAI, LLC, a company in which he has financial interests. AST is co-founder of Vathes Inc., and UploadAI LLC companies in which he has financial interests. JR is co-founder of Vathes Inc., and UploadAI LLC companies in which he has financial interests.

Methods

MICrONS Dataset. MICrONS dataset was collected in a single animal as described in MICrONS Consortium et al. (2021), including neurophysiological data collection, visual stimulation, stimulus composition, EM data collection, automatic EM segmentation and reconstruction, manual EM proofreading, volume coregistration, and manual soma-soma matching between the functional and EM volumes. Neurophysiological experiments, Visual Stimulution,and Stimulus Composition sections below are specific to additional experiments described in Supplemental Fig. 7.

Neurophysiological experiments. All procedures were approved by the Institutional Animal Care and Use Committee of Baylor College of Medicine. Ten mice (Mus musculus, 3 female, 7 males, 78-190 days old at first experimental scan) expressing GCaMP6s in excitatory neurons via Slc17a7-Cre and Ai162 transgenic lines (recommended and generously shared by Hongkui Zeng at Allen Institute for Brain Science; JAX stock 023527 and 031562, respectively) were anesthetized and a 4 mm craniotomy was made over the visual cortex of the right hemisphere as described previously (Reimer et al., 2014; Froudarakis et al., 2014).

Mice were head-mounted above a cylindrical treadmill and calcium imaging was performed with a mesoscope (Sofroniew et al., 2016) as described in release (MICrONS Consortium et al., 2021), with surface power not exceeding 20 mW, depth constant of 220 µm, and greatest laser power of $\sim$ 86 mW was used at approximately 400 µm from the surface.

The cranial window was leveled with regard to the objective with six degrees of freedom. Pixel-wise responses from an ROI spanning the cortical window (3600 x 4000 µm, 0.2 px/µm, 200 µm from surface, 2.5 Hz) to drifting bar stimuli were used to generate a sign map for delineating visual areas (Garrett et al., 2014).

For the orientation tuning validation data in Supplemental Fig. 7, our target imaging site was a $1200 \times 1100\,\mu\mathrm{m}^2$ area

spanning L2-L5 at the conjunction of lateral primary visual cortex (V1) and three lateral higher visual areas: anterolateral (AL), lateromedial (LM), and rostrolateral (RL). This resulted in an imaging volume that was roughly 50% V1 and 50% higher visual area. This target was chosen in order to mimic the area membership and functional property distribution in the MICrONS animal. Each scan was performed at 6.3 Hz, collecting eight $620 \times 1100\,\mu m^2$ fields per frame at 0.4 px/μm xy resolution to tile a $1190 - 1200 \times 1100\,\mu m^2$ FOV at four depths (two planes per depth, $40 - 50\,\mu m$ overlap between coplanar fields). The four imaging planes were distributed across layers with at least $50\,\mu m$ spacing, with two planes in L2/3 (depths: $180\,\mu m, 230\,\mu m$), one in L4 ($325\,\mu m$), and one in L5 ($400\,\mu m$).

Movie of the animal's eye and face was captured throughout the experiment. A hot mirror (Thorlabs FM02) positioned between the animal's left eye and the stimulus monitor was used to reflect an IR image onto a camera (Genie Nano C1920M, Teledyne Dalsa) without obscuring the visual stimulus. The position of the mirror and camera were manually calibrated per session and focused on the pupil. Field of view was manually cropped for each session. The field of view contained the left eye in its entirety, 212-330 pixels height x 262-424 pixels width at 20 Hz. Frame times were time stamped in the behavioral clock for alignment to the stimulus and scan frame times. Video was compressed using Labview's MJPEG codec with quality constant of 600 and stored the frames in AVI file.

Light diffusing from the laser during scanning through the pupil was used to capture pupil diameter and eye movements. A DeepLabCut model (Mathis et al., 2018) was trained on 17 manually labeled samples from 11 animals to label each frame of the compressed eye video (intraframe only H.264 compression, CRF:17) with 8 eyelid points and 8 pupil points at cardinal and intercardinal positions. Pupil points with likelihood >0.9 (all 8 in 69.8-99.2% of frames per scan) were fit with the smallest enclosing circle, and the radius and center of this circle was extracted. Frames with < 3 pupil points with likelihood >0.9 (<1.1% frames per scan), or producing a circle fit with outlier > 5.5 standard deviations from the mean in any of the three parameters (center x, center y, radius, <0.1% frames per scan) were discarded (total <1.2% frames per scan). Gaps were filled with linear interpolation.

The mouse was head-restrained during imaging but could walk on a treadmill. Rostro-caudal treadmill movement was measured using a rotary optical encoder (Accu-Coder 15T-01SF-2000NV1ROC-F03-S1) with a resolution of 8000 pulses per revolution, and was recorded at ~100 Hz in order to extract locomotion velocity.

Visual stimulation. For the validation data in Supplemental Fig. 2, 4 and 7, monitor size and positioning relative to the mouse were as described in MICrONS Consortium et al. (2021), with the exception of replacing the dot stimulus for monitor positioning with 10 x 10 grid tiling a central square (approx 90 degrees width and height) with 10 repetitions of 200 ms presentation at each location.

A photodiode (TAOS TSL253) was sealed to the top left corner of the monitor, and the voltage was recorded at 10 KHz and timestamped with a 10 MHz behavior clock. Simultaneous measurement with a luminance meter (LS-100 Konica Minolta) perpendicular to and targeting the center of the monitor was used to generate a lookup table for linear interpolation between photodiode voltage and monitor luminance in cd/m^2 for 16 equidistant values from 0-255, and one baseline value with the monitor unpowered.

At the beginning of each experimental session, we collected photodiode voltage for 52 full-screen pixel values from 0 to 255 for one second trials. The mean photodiode voltage for each trial was collected with an 800 ms boxcar window with 200 ms offset. The voltage was converted to luminance using previously measured relationship between photodiode voltage and luminance and the resulting luminance vs voltage curve was fit with the function $L = B + A \cdot P^{\gamma}$ where L is the measured luminance for pixel value P, and the γ of the monitor was fit as 1.73. All stimuli were shown without linearizing the monitor (i.e. with monitor in normal gamma mode).

During the stimulus presentation, display frame sequence information was encoded in a 3 level signal, derived from the photodiode, according to the binary encoding of the display frame (flip) number assigned in-order. This signal underwent a sine convolution, allowing for local peak detection to recover the binary signal together with its behavioral time stamps. The encoded binary signal was reconstructed for >93% of the flips. Each flip was time stamped by a stimulus clock (MasterClock PCIe-OSC-HSO-2 card). A linear fit was applied to the flip timestamps in the behavioral and stimulus clocks, and the parameters of that fit were used to align stimulus display frames with scanner and camera frames. The mean photodiode voltage of the sequence encoding signal at pixel values 0 and 255 was used to estimate the luminance range of the monitor during the stimulus, with minimum values of approximately 0.003-0.60 cd/m^2 and maximum values of approximately 8.68-10.28 cd/m^2.

Preprocessing of neural responses and behavioral data. Fluorescence traces from the MICrONS dataset and the additional data for Supplemental Fig. 2, 4 and 7 were detrended, deconvolved, and aligned to stimulus and behavior as described in Wang et al. (2024), and all traces were resampled at 29.967 Hz. Possible redundant traces, where a single neuron produced segmented masks in multiple imaging fields, were all kept for downstream model training. We elected to remove one of the 14 released scans from the analysis (session 7, scan_idx 4) due to compromised optics (water ran out from under the objective for $\sim$ 20 minutes), leaving 13 scans.

Model architecture and training of the digital twin model. The model architecture and training for the digital twin model used for assessing in silico signal correlation, feature weight similarity, and receptive field center distance is the same as the cvt-lstm model described in Wang et al. (2024).

Briefly, the core network of the cvt-lstm models was trained on 8 scans collected from 8 mice with natural movie stimuli to capture cortical representations of visual stimuli shared across mice. The parameters of the core network are then frozen, and the rest of the network parameters are trained for each scan with trials where natural movies are shown in the MICrONS dataset. Trials were excluded from model training if more than 25% of their pupil frames were untrackable. This issue most commonly arose when the animal closed its eye, rendering the functional relationship between neural activity and the visible stimulus ambiguous. The number of excluded trials varied across scans, ranging from 2 to 123 per scan, representing 0.6-38.0% of total trials.

To assess orientation tuning similarity, we used a slightly different digital twin model with a conv-lstm architecture as described in Wang et al. (2024). The core network of the conv-lstm models was trained with the same 8 scans as the cvt-lstm model. The rest of the network parameters are fine-tuned with both natural movies and oriented noise stimuli available from the MICrONS dataset to reach maximum alignment between in vivo and in silico orientation tuning.

Functional unit inclusion criteria. In order to focus our analyses on neurons that are visually responsive and well modeled by the digital twin, we applied a dual functional threshold over two metrics (*in vivo* reliability and model prediction performance) prior to all analyses related to signal correlation, receptive field center distance, and feature weight similarity.

In vivo reliability threshold. In order to estimate the reliability of neuronal responses to visual stimuli, we computed the upper bound of correlation coefficients for each neuron(CC_{max}, Schoppe et al. 2016) across 60 seconds of natural movie stimuli repeated 10 times across the stimulus period (10 min total). CC_{max} was computed as:

$$CC_{max} = \sqrt{\frac{NVar(\overline{y}) - \overline{Var(y)}}{(N-1)Var(\overline{y})}},$$

where y is the *in vivo* responses, and N is the number of trials. A threshold of $CC_{max} > 0.4$ was applied. Where more than one two-photon functional unit was matched to a given EM unit, the functional trace with the higher oracle score was used for analysis.

Model prediction performance threshold. In order to focus our analyses on neurons for which adequate model performance indicated sufficiently accurate representation of the neuronal tuning features, we computed the test correlation coefficient on the withheld oracle test dataset, which was not part of the training set. Test correlation coefficients (CC_{abs}) were computed as:

$$CC_{abs} = \frac{Cov(\overline{x},\overline{y})}{\sqrt{Var(\overline{x})Var(\overline{y})}},$$

where x is the *in silico* response and y is the *in vivo* response. A threshold of $CC_{abs} > 0.2$ was applied.

144 out of 148 presynaptic neurons and 3920 out of 4811 postsynaptic neurons passed the dual functional unit inclusion criteria.

Oracle score. The oracle score was computed for all units as described in MICrONS Consortium et al. (2021). Oracle score is later used to select presynaptic neurons for morphological proofreading (see below).

Two-photon/ Electron Microscopy Matching. The matching between two-photon functional units and EM cells aligns closely with table `coregistration_manual_v4` (MICrONS Consortium et al., 2021) with some additional restrictions applied. First, the matches to the excluded scan described in Section **Preprocessing of neural responses and behavioral data** were removed. Then, two thresholds were applied directly to the table (residual < 20 and score $>$ -10).

Morphological Proofreading. While automation of the EM segmentation has progressed to where dense reconstruction is possible at the millimeter scale, even state-of-the-art methods still leave imperfections in the graph relative to human expert performance. The two categories of reconstruction error are false merges (the incorrect grouping of segmented objects, such as including an axon or dendrite that does not belong to a specific soma) and false splits (the incorrect separation of objects, such as excluding an axon or dendrite that does belong to a specific soma). These errors lead to incorrect associations between pre- and post-synaptic partners and ultimately an incorrect connectivity graph. Proofreading corrects false merges by "cleaning" the reconstruction, i.e. removing incorrectly associated segments, and corrects false splits by "extending" the reconstruction, i.e. adding back missing segments. We used two proofreading approaches in this study: manual and automatic. "Manual proofreaders" were trained to both clean and extend reconstructions to a high degree of accuracy, as validated by expert neuroanatomists. All of the presynaptic cells in this study were manually proofread. The manual proofreading protocol can be found in the primary dataset paper, (MICrONS Consortium et al., 2021). For the rest of the cells (postsynaptic and control neurons), we used the NEURD package (Celii et al., 2024) to perform automated proofreading. Automated proofreading cleans reconstructions to a high degree of accuracy relative to manual proofreaders, but it does not extend reconstructions.

Dendritic Proofreading. At baseline, reconstructed dendrites were generally complete and required little extension (Elabbady et al., 2024). However, they often contained false merges that required cleaning (Elabbady et al., 2024). The dendrites of all of the presynaptic neurons were manually cleaned and extended. The dendrites of other neurons were cleaned with NEURD (Celii et al., 2024).

Axonal Proofreading. At baseline, reconstructed axons require both cleaning and extension (Elabbady et al., 2024).

Only the axons of presynaptic neurons were manually cleaned and extended. In order to balance morphological completeness (per neuron) and coverage (across projection types), we extended axons to varying degrees of completion. Specifically, we performed full manual proofreading on a subset of neurons (n=84), which involved thoroughly cleaning and extending all axonal branches throughout the dataset. For the remaining neurons (n=64), we applied partial proofreading, focusing exclusively on extending axonal branches that were pre-screened to feedback from HVA to V1. The full list of proofread presynaptic neurons, their area and layer membership, and whether they were fully or partially proofread is included in Supplemental Table 1, and a subset of proofread axons are shown in Supplemental Fig. 1.

Presynaptic Neuron Selection. Our approach for selecting presynaptic neurons for manual proofreading was designed to enrich for higher-order connectivity motifs within and (especially) across visual areas. Because connection probability drops off with distance (Holmgren et al., 2003), we elected to initially focus proofreading efforts on spatially clustered cells in two cylindrical columns spanning cortical layers 2-5, with the first column located in V1 and the second located in RL. Column centers were chosen according to retinotopic maps, as it has been shown that inter-areal projections are retinotopically matched (Wang and Burkhalter, 2007; Marques et al., 2018). During the proofreading process we added an additional column in V1 and another spanning the RL and AL border, to increase coverage of the volume. Lastly, a few HVA cells that were postsynaptic to proofread V1 cells were chosen to enrich for higher order motifs (n=9). All neurons selected for proofreading had an oracle score greater than 0.25 and model test correlation (model predictive performance from an intermediate version of the digital twin) greater than 0.15. The first 40 neurons were selected by experienced neuroscientists unblinded to functional properties for an emphasis on functional diversity. All remaining neurons were chosen blind to functional properties.

Anatomical controls. In order to control for anatomy at the axonal scale, we recruited all visually responsive, well predicted, functionally matched excitatory neurons (CC_{max} > 0.4, CC_{abs} > 0.2) that are located in the same region as the postsynaptic target, but are not observed to form a synapse with the presynaptic neuron (same region control). Area membership labels per neuron were used from the MICrONS release (MICrONS Consortium et al., 2021). Additionally, control candidates that meet criteria for both the same region control and the ADP control (described below) will only be included in ADP control.

In order to control for anatomy at the synaptic scale, we recruited all visually responsive, well predicted, functionally matched excitatory neurons (CC_{max} > 0.4, CC_{abs} > 0.2) with a dendritic skeleton passing within $5\,\mu\mathrm{m}$ of the presynaptic neuron axonal synapse in the presynaptic axonal arbor (3D euclidean distance), but which are not observed to form a synapse with the presynaptic neuron (ADP control). Presynaptic axonal skeletons were computed using the `pcg_skel` package developed by collaborators at the Allen Institute for Brain Science (Schneider-Mizell et al., 2024; Schneider-Mizell and Collman, 2023). For postsynaptic dendritic skeletons, we used the automatically proofread and skeletonized dendritic arbors as described in Celii et al. 2024.

To compute the axon-dendrite co-travel distance (L_d) between a pair of neurons, we first discretized both the axonal skeleton of one neuron and the dendritic skeleton of the other neuron so that no edge exceeded a length of 1 μm. Next, we identified all pairs of vertices from the two skeletons that were within 5 μm of each other by performing spatial queries using KDTree's `query_ball_tree` method from the `scipy.spatial` module in SciPy (Virtanen et al., 2020). From these proximal vertices ("proximity"), we identified the associated dendritic edges. The lengths of these dendritic edges were summed to obtain L_d.

Synapses were obtained from Table `synapses_pni_2` (MICrONS Consortium et al., 2021) and were assigned to an axon-dendrite proximity if they were within 3 μm of any vertex in the proximity.

In the case of the joint area and layer analysis (Fig. 4), candidates in both the "same region" and "ADP" controls must additionally match the same layer classification as the postsynaptic target in order to be included. Layer assignment was performed as in (Weis et al., 2024).

Measuring functional similarities.

In silico response correlations. To characterize the pair-wise tuning similarity between two modeled neurons, we computed the Pearson correlation of their responses to 2500 seconds of natural movies. The natural movies were fed in to the model as trials of 10 sec. Model responses were generated at 29.967 Hz and Pearson correlations were computed after binning the responses into $500\,\mathrm{msec}$ non-overlapping bins and concatenating across trials.

In silico feature weight similarity and receptive field center distance. The digital twin model architecture includes a shared core which is trained to represent spatiotemporal features in the stimulus input, and a final layer where the spatiotemporal features at a specific readout location are linearly weighted in order to produce the predicted activity of a specific neuron at the current time point (Wang et al., 2024). The readout location and linear feature weight are independently learned for each neuron. In order to measure the feature weight similarity between two units, we extract the linear feature weights from this final step as vector of length 512, and take the cosine similarity between the two vectors. In order to measure the receptive field center distance between two units, we extract the readout location as 2D coordinates on the monitor, and take the angle between them with respect to the mouse's eye, assuming the monitor is centered on, 15 cm away from, and normal to the surface of the mouse's eye at the closest point.

In silico *difference in preferred orientation.* 240 blocks of parametric directional visual stimuli ("Monet") are shown

to the model, with each fifteen-second block consisting of 16 trials of equally distributed and randomly ordered unique directions of motion between 0-360 degrees. A modeled neuron's direction tuning curve is computed as its mean responses to 16 directions averaged across blocks. We calculated the global orientation selectivity index (gOSI) and the orientation selectivity index (OSI) from the modeled neuron's tuning curve as follows:

$$gOSI = \frac{\Sigma R_\theta e^{2i\theta}}{\Sigma R_\theta}, OSI = \frac{R_{po} - R_{ortho}}{R_{po} + R_{ortho}} \quad \textbf{(1)}$$

where θ is the direction of the stimulus, R_θ is the mean modeled response to the stimulus at direction θ, and R_{po} and R_{ortho} are the mean modeled responses at the preferred and orthogonal orientation, respectively. The gOSI metric is based on the $1 - CircVar$ metric in (Mazurek et al., 2014), which is a vector-based method designed to reduce the uncertainty in quantifying orientation selectivity of responses, especially in cases where high throughput, unbiased recording methods return many cells with low orientation selectivity, as is the case with calcium imaging. Only neurons with $gOSI > 0.25$ were included in the analyses in this paper. For neurons selected with our gOSI threshold > 0.25, the computed OSI ranges from 0.43 to 0.99, with mean of 0.56. For both thresholds, the fraction of cells considered orientation tuned (57.4% of coregistered V1 neurons has gOSI > 0.25, 62.7% of coregistered V1 neurons has OSI > 0.4) is similar to those reported in other studies (72% in V1 layer 2/3 (Ko et al., 2011), 62.9% in V1 layer 2/3 and 58.0% in V1 layer 4 (Kondo and Ohki, 2016).Unit-wise direction tuning curves are then modeled by a bivariate von Mises function with an offset:

$$\begin{aligned} f(\theta|\mu,\kappa,p) = \frac{1}{2\pi I_0(\kappa)} \{ & p\exp(\kappa\cos(\theta-\mu)) \\ & + (1-p)\exp(-\kappa\cos(\theta-\mu))\} \\ & + b \end{aligned} \quad \textbf{(2)}$$

where I_0 is the modified Bessel function, μ is the preferred direction, κ measures the concentration of the two peaks (larger κ means higher peaks thus higher orientation selectivity), p measures the relative height of the two peaks ($p = 0.5$ means two peaks of the same height, when p approaches 0 or 1, the bi-modal distribution reduces to a uni-model von Mises distribution), b is the offset. μ, κ, p, and b are fit by minimizing least squared error. The preferred orientation of a neuron is taken as the modulus of μ to 180 degrees.

Validation of the digital twin model.

Validation of* In silico *signal correlations. To validate the *in silico* signal correlations generated by our digital twin model, we first established a benchmark for *in vivo* signal correlations. We began by determining the optimal number of stimulus repetitions for measuring *in vivo* signal correlations. Two mice were presented with 6 unique 10-second natural movie clips, each repeated 60 times over a 60-minute period. Based on the results shown in Supplemental Fig. 2a, we determined that 10 repetitions per clip provided a reliable estimate of *in vivo* signal correlation while maintaining a reasonable experimental time for presenting a large number of clips in subsequent experiments.

With this optimal repetition count established, we conducted experiments with three mice using an expanded set of visual stimuli. These stimuli contained those presented in the MICrONS dataset as described in MICrONS Consortium et al. (2021), including natural movies, global directional parametric stimuli ("monet"), and local directional parametric stimuli ("trippy"). Additionally, we presented 36 unique 10-second natural movie clips, each repeated 10 times, totaling 60 minutes of stimulation. To facilitate comparison with the MICrONS dataset and establish a robust ground truth, we divided these 36 clips into two sets: a benchmark set of 30 clips repeated 10 times, serving as our "ground truth" for signal correlation, and a MICrONS-equivalent set of 6 clips repeated 10 times, mimicking the amount of repeated natural clip data available in the MICrONS dataset.

For each mouse, we trained a digital twin model using the same architecture and training data as the MICrONS digital twin. This allowed us to generate three signal correlation matrices for comparison: an *in vivo* matrix computed from the MICrONS-equivalent set, an *in silico* matrix generated by the digital twin model using 250 novel natural movie clips, and a benchmark matrix computed from the 30-clip set. To compare these matrices, we randomly sampled submatrices of signal correlations between 1000 neurons. We then performed hierarchical clustering using Ward's method on the benchmark matrix and used the resulting dendrogram to sort neurons. This sorting was applied to the MICrONS-equivalent and *in silico* matrices for visual comparison, as shown in Supplemental Fig. 2b. Following this initial comparison, we calculated the Pearson correlation coefficient between the corresponding entries in the lower triangles of the three matrices. To assess statistical significance, we employed a resampling approach, performing 1000 random splits of the benchmark and MICrONS-equivalent sets, from which we estimated the standard deviation and resampling-based p-value of the Pearson correlations. This comprehensive approach enabled us to evaluate how well our digital twin model's *in silico* signal correlations matched the ground truth compared to *in vivo* measurements with limited data, thus validating the model's performance in replicating neural response correlations.

Validation of receptive field center. To validate the receptive field estimates of our digital twin model, we conducted additional experiments and analyses comparing *in vivo* and *in silico* silico receptive field measurements. We collected three additional functional scans using an expanded set of visual stimuli. These stimuli contained those presented in the MICrONS dataset as described in MICrONS Consortium et al. (2021), including natural movies, global directional parametric stimuli ("monet"), and local directional parametric stimuli ("trippy"). Additionally, we presented 57.6 minutes of sparse noise stimuli. The sparse noise stimuli consisted of bright (pixel value 255) and dark (pixel value 0) square dots,

each approximately 6° in visual angle, presented on a grey background (pixel value 127) in a randomized order. These dots were presented at 12 positions covering 70° of visual angle along both the horizontal and vertical axes of the screen. Each presentation lasted 200 ms, and each condition was repeated 60 times.

We computed the *in vivo* spike-triggered average (STA) receptive fields by cross-correlating the visual stimuli with deconvolved calcium traces. STAs for bright dots (on-STAs) and dark dots (off-STAs) were estimated independently and then combined by taking the pixel-wise maximum of the on- and off-STAs. We then presented the same sparse noise stimuli to the digital twin model and computed *in silico* silico STA receptive fields using the model responses. To assess STA quality, we generated response predictions by multiplying each neuron's STA with the stimulus frames and compared these predictions to either the *in vivo* trial-averaged responses or model responses using Pearson correlation coefficients. Neurons with correlations greater than 0.2 were considered well-characterized. We then extracted the STA receptive field centers by fitting a 2D Gaussian to the STAs, with fits yielding an r-squared value over 0.5 considered well-fit. Our analysis revealed that 40% of all imaged neurons had well-characterized, well-fit *in vivo* STAs.

Finally, we visualized the retinotopic maps measured with either *in vivo* STA or *in silico* STA by converting the STA receptive field centers to azimuth and elevation angles, assuming the mouse was looking at the center of the monitor. To exclude partially measured STAs, we included only neurons with fitted STA centers located in the central 8x8 square of the entire 12x12 stimulus grid (27% of all imaged neurons) for the analysis presented in Supplemental Fig. 4 a, b, and c left. For the analysis in Supplemental Fig. 4 c right, we included neurons with the bottom 25% of response correlations.

Validation of orientation tuning. To validate *in silico* orientation tuning with *in vivo* orientation tuning, we collected three additional functional scans with an expanded set of stimuli. These stimuli contained those presented in the MICrONS dataset as described in MICrONS Consortium et al. (2021), including natural movies, global directional parametric stimuli ("monet"), and local directional parametric stimuli ("trippy"). In addition, each stimulus contained an additional 40 minutes of trials, randomly intermixed, as follows:

- **Unique Global Directional Parametric Stimulus ("Monet"):** 120 seeds, 15 seconds each, 1 repeat per scan, 30 minutes total. Seeds conserved across all scans.
- **Oracle Global Directional Parametric Stimulus ("Monet"):** 4 seeds, 15 seconds each, 10 repeats, 10 minutes total. Seeds conserved across all scans.

We characterized both the *in vivo* orientation tuning in response to 30 minutes of global directional parametric stimulus ("Monet", Supplemental Fig. 7a), as well as the *in silico* orientation tuning as described above for digital twin models with shared cores and readouts trained on neurons from the same scans, in response to stimuli matching the composition and duration of the MICrONS release scans (Supplemental Fig. 7b). When we applied a threshold of $gOSI > 0.25$, we found that 95% of cells had an absolute difference between their *in silico* and *in vivo* preferred orientations less than $9.77°$.

Statistical analysis of mean signal correlations. We employed paired t-tests to compare signal correlations between presynaptic neurons and three groups of potential target neurons: connected postsynaptic neurons, axon-dendrite proximity (ADP) neurons, and same-region control neurons. Our analysis focused on presynaptic neurons with more than 10 postsynaptic targets for each projection type to ensure robust comparisons. For each presynaptic neuron, we computed mean signal correlations with its synaptically connected postsynaptic targets, ADP neurons (neurons with dendrites in proximity to the presynaptic axon but not synaptically connected), and same-region control neurons (neurons in the same brain region but without proximal axon-dendrite contacts). We then performed paired t-tests to compare these mean correlations. For example, to compare connected and ADP neuron pairs, we conducted a paired t-test between each presynaptic neuron's mean signal correlation with its postsynaptic targets versus its mean signal correlation with ADP neurons. This approach allowed us to control for variability across presynaptic neurons while directly comparing their correlations with different target groups. All statistical analyses were performed using the `scipy` package in Python. We set the significance level (α) at 0.05 for all tests. To account for multiple comparisons, we adjusted p-values using the Benjamini-Hochberg (BH) procedure as implemented in the `statsmodels` package.

Visualization of the relationship between L_d, N_{syn}/L_d and the functional similarities.

Visualization of L_d. To quantify the changes in L_d as a function of functional similarities, we restrict our analysis to neuron pairs with no synaptic connections observed between them. We then follow these steps:

1. We compute the mean L_d and mean functional similarities for each presynaptic neuron across all other neurons that no synaptic connections with the presynaptic neuron were observed.
2. We subtract the presynaptic mean from each of the pairwise L_d and functional similarities between every neuron pair to compute ΔL_d and $\Delta similarity$.
3. The neurons pairs are then binned by $\Delta similarity$ and the average ΔL_d is computed for each bin.
4. The standard deviation of average ΔL_d is estimated by bootstrapping . Specifically, we resampled the neuron pairs 1000 times with replacement and repeated steps 1-3.

Only bins with more than 10 connected neuron pairs and more than 10 presynaptic neurons are included in the visualization.

Visualization of N_{syn}/L_d**.** To quantify the changes in N_{syn}/L_d as a function of functional similarities, we restrict our analysis to neuron pairs with positive L_d observed between them. We then follow these steps:

1. We compute the mean N_{syn}/L_d and mean functional similarities for each presynaptic neuron across all other neurons that no synaptic connections with the presynaptic neuron were observed.
2. We subtract the presynaptic mean from each of the pairwise N_{syn}/L_d and functional similarities between every neuron pair to compute $\Delta N_{syn}/L_d$ and $\Delta similarity$.
3. The neurons pairs are then binned by $\Delta similarity$ and the average $\Delta N_{syn}/L_d$ is computed for each bin.
4. The standard deviation of average ΔL_d is estimated through bootstrapping. Specifically, we resampled the neuron pairs 1000 times with replacement and repeated steps 1-3.

Only bins with more than 10 connected neuron pairs and more than 10 presynaptic neurons are included in the visualization.

Statistical modeling of "like-to-like" rules for different anatomical measurements.

Axon-dendrite co-travel distance (L_d***).*** L_d measures the distance dendrites of one neuron travel within 5 μm from another neuron's axon. Most pairs of neurons' axons and dendrites never come into close proximity with each other, and their L_d is zero. Thus, the L_d distribution is a non-negative continuous distribution with a substantial non-zero probability measure at zero L_d. Thus, we modeled L_d as a random variable following the Tweedie exponential dispersion family (with Tweedie index parameter $\xi \in (1,2)$). Tweedie distributions with such index parameters are Poisson mixtures of gamma distributions, commonly used to model continuous data with exact zeros. We assume two neurons' axons and dendrites travel within 5 μm at N proximity points, where $N \sim \text{Pois}(\lambda^*)$, λ^* is the mean number of axonal dendritic proximal contacts of the Poisson distribution. When $N > 0$, we assume the distance dendrites travel within five μm at each proximal point z_i $(i = 1, \ldots, N)$ follows a Gamma distribution $\text{Gam}(\mu, \phi)$. Under these assumptions, the total potential synapsing distance

$$L_d = \Sigma_{i=1}^{N} z_i,$$

where $L_d = 0$ when $N = 0$, follows a Tweedie distribution with $1 < \xi < 2$. We then model the relationship between L_d, functional similarities Sim (e.g., signal correlation, feature weight similarity, receptive field location distance between two neurons), and projection types $Proj$ using a Tweedie-distributed generalized linear mixed model (GLMM) with a log link function. For analysis at the brain area level, $Proj$ is a nominal variable with 4 categories: V1 intra-area, HVA intra-area projections, feedforward projections, and feedback projections. For analysis at the brain area and layer level, we apply GLMMs for modeling as they have been recommended for accounting for multi-level data dependencies in datasets (Yu et al., 2022), such as the projection types and presynaptic neuron proofreading progress in our study. We specify the model as follows:

$$\begin{aligned} log(L_{d_{ij}}) = \beta_0 &+ \beta_1 Sim_{ij} + \beta_2 Proj_{k(i,j)} \\ &+ \beta_3 Sim_{ij} \times Proj_{k(i,j)} + u_{k(i,j),i} \\ &+ \epsilon_{ij} \end{aligned}$$

where:

- $L_{d_{ij}}$ is the axon-dendrite co-travel distance between presynaptic neuron i and postsynaptic neuron j
- Sim_{ij} is the functional similarity between the neuron pair
- $Proj_{k(i,j)}$ is the projection type of the neuron pair (i,j)
- β_1, β_2, and β_3 are the fixed effect coefficients of the functional similarity, projection type, and their interaction term, respectively
- β_0 is the intercept
- $u_{k(i,j),i}$ is the random effect accounting for the projection type k and the proofread status associated with presynaptic neuron i
- ϵ_{ij} is the error term, following a Tweedie distribution

The coefficients β_1, β_2, and β_3 represent how functional similarities and projection types affect connectivity at the axonal scale. We fit the models for each functional similarity independently using the `glmmTMB` R package. The goodness-of-fit of the estimated models is reported as Nakagawa's R squared, computed with the `performance` R package. We define the axonal-scale like-to-like coefficients for each functional similarity and projection type as the estimated linear association between each category of functional similarity conditioned on the projection type. The coefficient estimates and the corresponding significance tests are computed for the fitted GLMM using the `emtrends` function from the `emmeans` R package.

Number of synapses (N_{syn}***).*** N_{syn} measures the number of synapses between two neurons. We model it as a $Poisson$-distributed random variable and its relationship to functional similarities as a GLMM model with the following specifications:

$$\begin{aligned} log(N_{syn_{ij}}) = \beta_0 &+ \beta_1 Sim_{ij} + \beta_2 Proj_{k(i,j)} \\ &+ \beta_3 Sim_{ij} \times Proj_{k(i,j)} + u_{k(i,j),i} \\ &+ \epsilon_{ij} \end{aligned}$$

where:

- $N_{syn_{ij}}$ is the number of synapses between presynaptic neuron i and postsynaptic neuron j
- Sim_{ij} is the functional similarity between the neuron pair
- $Proj_{k(i,j)}$ is the projection type of the neuron pair (i,j)
- β_1, β_2, and β_3 are the fixed effect coefficients of the functional similarity, projection type, and their interaction term, respectively
- β_0 is the intercept
- $u_{k(i,j),i}$ is the random effect accounting for the projection type k and the proofread status associated with presynaptic neuron i
- ϵ_{ij} is the error term, following a Poisson distribution

The coefficients β_1, β_2, and β_3 estimate how the functional similarities and projection types affect connectivity regardless of the spatial scales (i.e., axonal or synaptic). We fit the models for each functional similarity independently using the `glmmTMB` R package. The goodness-of-fit of the estimated models is reported as Nakagawa's R squared, computed with the `performance` R package. We define the axonal-scale like-to-like coefficients for each functional similarity and projection type as the estimated linear association between each category of functional similarity conditioned on the projection type. The coefficient estimates and the corresponding significance tests are computed for the fitted GLMM using the `emtrends` function from the `emmeans` R package.

Synapse conversion rate (N_{syn}/L_d). N_{syn}/L_d measures the number of synapses per millimeter axon-dendrite co-travel distance for each neuron pair. To quantify its relationship to functional similarities, we adopted the following GLMM model:

$$log(N_{syn_{ij}}) = \beta_0 + \beta_1 Sim_{ij} + \beta_2 Proj_{m(i,j)} + \beta_3 Sim_{ij} \times Proj_{k(i,j)} + u_{k(i,j),i} + \epsilon_{ij} + log(L_{d_{ij}})$$

where:

- $N_{syn_{ij}}$ is the number of synapses between presynaptic neuron i and postsynaptic neuron j
- $L_{d_{ij}}$ is the axon-dendrite co-travel distance between the neuron pair
- Sim_{ij} is the functional similarity between the neuron pair
- $Proj_{m(i,j)}$ is the projection type of the neuron pair (i,j)
- β_1, β_2, and β_3 are the fixed effect coefficients of the functional similarity, projection type, and their interaction term, respectively
- β_0 is the intercept
- $u_{k(i,j),i}$ is the random effect accounting for the projection type k and the proofread status associated with presynaptic neuron i
- ϵ^{ij} is the error term, following a Poisson distribution

The above equation can be re-arranged to:

$$log\left(\frac{N_{syn_{ij}}}{L_{d_{ij}}}\right) = \beta_0 + \beta_1 Sim_{ij} + \beta_2 Proj_{k(i,j)} + \beta_3 Sim_{ij} \times Proj_{k(i,j)} + u_{k(i,j),i} + \epsilon_{ij}$$

Thus, β_1, β_2, and β_3 model how the functional similarities affect synapse conversion rate (N_{syn}/L_d) at the synaptic scale. We fit the models for each functional similarity independently using the `glmmTMB` R package. The goodness-of-fit of the estimated models is reported as Nakagawa's R squared, computed with the `performance` R package. We define the like-to-like coefficients of each functional similarity for each projection type as the estimated linear association between each category of functional similarity conditioned on the projection type. The coefficient estimates and the corresponding significance tests are computed for the fitted GLMM using the `emtrends` function from the `emmeans` R package. To avoid fitting models to projection types with little data or dominated by few presynaptic neurons, for all the models described above, we only include and report like-to-like coefficients to projection types with more than 30 synapses observed, more than 5 presynaptic neurons, and with none of the presynaptic neurons contributing more than half of all synapses observed.

Statistical analysis of functional similarities and synaptic anatomy. We investigated the relationship between functional similarities of neurons and the anatomical features of their synaptic connections. Our analysis accounted for the confounding effect of axon-dendrite co-travel distance (L_d), which correlates with both functional similarities and synaptic measurements. To isolate the effect of synaptic anatomy on functional similarity, we employed a two-step regression approach:
First, we condition our analysis on the effect of L_d from the functional similarity measure. This process involves:

1. Fitting a linear regression model with functional similarity as the dependent variable and L_d as the independent variable.
2. Calculating the residuals from this model, which represent the variation in functional similarity that cannot be explained by L_d alone.

These residuals become our new measure of functional similarity, adjusted for the influence of L_d. Next, we constructed a linear regression model using these residuals as the dependent variable. The independent variables in this model

included anatomical measurements of synaptic connections, the total number of synapses between neuron pairs and the mean synaptic cleft volume.

This approach allows us to test whether synaptic measurements significantly predict functional similarities between neurons, beyond what can be explained by their physical proximity (as measured by L_d).

Common input analysis.

Functional similarity among all postsynaptic neurons sharing one common input. For a connectivity graph G, we define

$$\rho_G(i) = \frac{\Sigma_{j\neq i}\Sigma_{k\notin(i,j)} Sim_{jk} N_{syn_{ij}} N_{syn_{ik}}}{\Sigma_{j\neq i}\Sigma_{k\notin(i,j)} N_{syn_{ij}} N_{syn_{ik}}},$$

where i is a presynaptic neuron and j, k are any two neurons in the volume. ρ measures the average similarity of all postsynaptic neurons of the presynaptic neuron i.

Estimation of ρ expected by pairwise "like-to-like" connectivity rules. With the observed connectivity graph G, we estimated the relationship between N_{syn} and the functional similarities (in silico signal correlation, feature weight similarity, and receptive field center distance) with GLMM similar to the specifications for modeling the number of synapses described above. Instead of modeling each functional similarity independently, we included all functional similarities and their interaction with projection types in a single model to account for as much pairwise connectivity rule as possible. We then estimated the expected functional similarity among all postsynaptic neurons sharing one common input i as:

$$\rho'_G(i) = \frac{\Sigma_{j\neq i}\Sigma_{k\notin(i,j)} Sim_{jk} N'_{syn_{ij}} N'_{syn_{ik}}}{\Sigma_{j\neq i}\Sigma_{k\notin(i,j)} N'_{syn_{ij}} N'_{syn_{ik}}},$$

where $N'_{syn_{ij}}$ is the predicted number of synapses between neurons i and j given their functional similarities by the GLMM.

RNN model. The RNN model used to produce the results in Fig. 6 consisted of a vanilla RNN layer with 1000 hidden units and a hyperbolic tangent activation function simulated over 20 time steps. Static inputs were obtained by passing MNIST images through a linear layer. Outputs were obtained by passing the hidden activations at the last time step through another linear layer. All three layers were trained for 10 epochs, a batch size of 512, the categorical cross entropy loss function, and the Adam optimizer in PyTorch. A pre- and post-synaptic neuron pair was classified as connected if the associated weight was in the top 35^{th} percentile of all weights, specifically if the weight larger than 0.01. In Fig. 6d, weights were chosen as candidates for ablation if the weight was above 0.01 and the neurons' signal correlation was above 0.2. About 10.5% of the weights met these criteria, and ablated weights were selected randomly from this set. Changing the thresholds for weights and signal correlations did not change our conclusions.

Software. Experiments and analysis are carried out with custom built data pipelines. The data pipeline is developed in Matlab, Python, and R with the following tools: Psychtoolbox, ScanImage, DeepLabCut, CAIMAN, and Labview were used for data collection. DataJoint, MySQL, and CAVE were used for storing and managing data. Meshparty, NEURD, and pcg_skel were used for morphology analysis. Numpy, pandas, SciPy, statsmodels, scikit-learn, PyTorch, tidyverse, glmmTMB, performance, and emmeans were used for model training and statistical analysis. Matplotlib, seaborn, HoloViews, Ipyvolume, and Neuroglancer were used for graphical visualization. Jupyter, Docker, and Kubernetes were used for code development and deployment.

Data availability. All MICrONS data have already been released on BossDB (https://bossdb.org/project/microns-minnie, please also see https://www.microns-explorer.org/cortical-mm3 for details). Additional data including learned weights of the digital twin model and *in silico* similarity metrics will be made publicly available in an online repository latest upon journal publication. Please contact the corresponding authors for advance access.

Code availability. Custom developed code used in the analysis including digital twin architecture will be made publicly available in an online repository latest upon journal publication. Please contact the corresponding authors for advance access.

Bibliography

D. D. Bock, W.-C. A. Lee, A. M. Kerlin, M. L. Andermann, G. Hood, A. W. Wetzel, S. Yurgenson, E. R. Soucy, H. S. Kim, and R. C. Reid. Network anatomy and in vivo physiology of visual cortical neurons. *Nature*, 471(7337):177–182, Mar. 2011.

V. Braitenberg and A. Schüz. *Cortex: Statistics and geometry of neuronal connectivity*. Springer Science & Business Media, Mar. 2013.

S. A. Cadena, G. H. Denfield, E. Y. Walker, L. A. Gatys, A. S. Tolias, M. Bethge, and A. S. Ecker. Deep convolutional models improve predictions of macaque v1 responses to natural images. *PLoS computational biology*, 15(4):e1006897, 2019.

B. Celii, S. Papadopoulos, Z. Ding, P. G. Fahey, E. Wang, C. Papadopoulos, A. B. Kunin, S. Patel, J. Alexander Bae, A. L. Bodor, D. Brittain, J. Buchanan, D. J. Bumbarger, M. A. Castro, E. Cobos, S. Dorkenwald, L. Elabbady, A. Halageri, Z. Jia, C. Jordan, D. Kapner, N. Kemnitz, S. Kinn, K. Lee, K. Li, R. Lu, T. Macrina, G. Mahalingam, E. Mitchell, S. S. Mondal, S. Mu, B. Nehoran, S. Popovych, C. M. Schneider-Mizell, W. Silversmith, M. Takeno, R. Torres, N. L. Turner, W. Wong, J. Wu, S.-C. Yu, W. Yin, D. Xenes, L. M. Kitchell, P. K. Rivlin, V. A. Rose, C. A. Bishop, B. Wester, E. Froudarakis, E. Y. Walker, F. Sinz, H. Sebastian Seung, F. Collman, N. M. da Costa, R. Clay Reid, X. Pitkow, A. S. Tolias, and J. Reimer. NEURD: automated proofreading and feature extraction for connectomics. *bioRxiv*, Apr. 2024. URL https://www.biorxiv.org/content/10.1101/2023.03.14.532674v4.

L. Cossell, M. F. Iacaruso, D. R. Muir, R. Houlton, E. N. Sader, H. Ko, S. B. Hofer, and T. D. Mrsic-Flogel. Functional organization of excitatory synaptic strength in primary visual cortex. *Nature*, 518(7539):399–403, 2015.

S. Dorkenwald, C. E. McKellar, T. Macrina, N. Kemnitz, K. Lee, R. Lu, J. Wu, S. Popovych, E. Mitchell, B. Nehoran, Z. Jia, J. A. Bae, S. Mu, D. Ih, M. Castro, O. Ogedengbe, A. Halageri, K. Kuehner, A. R. Sterling, Z. Ashwood, J. Zung, D. Brittain, F. Collman, C. Schneider-Mizell, C. Jordan, W. Silversmith, C. Baker, D. Deutsch, L. Encarnacion-Rivera, S. Kumar, A. Burke, D. Bland, J. Gager, J. Hebditch, S. Koolman, M. Moore, S. Morejohn, B. Silverman, K. Willie, R. Willie, S.-C. Yu, M. Murthy, and H. S. Seung. FlyWire: online community for whole-brain connectomics. *Nat. Methods*, 19(1):119–128, Jan. 2022a.

S. Dorkenwald, N. L. Turner, T. Macrina, K. Lee, R. Lu, J. Wu, A. L. Bodor, A. A. Bleckert, D. Brittain, N. Kemnitz, W. M. Silversmith, D. Ih, J. Zung, A. Zlateski, I. Tartavull, S.-C. Yu, S. Popovych, W. Wong, M. Castro, C. S. Jordan, A. M. Wilson, E. Froudarakis, J. Buchanan, M. M. Takeno, R. Torres, G. Mahalingam, F. Collman, C. M. Schneider-Mizell, D. J. Bumbarger, Y. Li, L. Becker, S. Suckow, J. Reimer, A. S. Tolias, N. Macarico da Costa, R. C. Reid, and H. S. Seung. Binary and analog variation of synapses between cortical pyramidal neurons. *Elife*, 11, Nov. 2022b.

L. Elabbady, S. Seshamani, S. Mu, G. Mahalingam, C. Schneider-Mizell, A. L. Bodor, J. Alexander Bae, D. Brittain, J. Buchanan, D. J. Bumbarger, M. A. Castro, S. Dorkenwald, A. Halageri, Z. Jia, C. Jordan, D. Kapner, N. Kemnitz, S. Kinn, K. Lee, K. Li, R. Lu, T. Macrina, E. Mitchell, S. S. Mondal, B. Nehoran, S. Popovych, W. Silversmith, M. Takeno, R. Torres, N. L. Turner, W. Wong, J. Wu, W. Yin, S.-C. Yu, The MICrONS Consortium, H. Sebastian Seung, R. Clay Reid, N. M. Da Costa, and F. Collman. Perisomatic features enable

efficient and dataset wide Cell-Type classifications across Large-Scale electron microscopy volumes. *bioRxiv*, Jan. 2024. URL https://www.biorxiv.org/content/10.1101/2022.07.20.499976v2.

P. G. Fahey, T. Muhammad, C. Smith, E. Froudarakis, E. Cobos, J. Fu, E. Y. Walker, D. Yatsenko, F. H. Sinz, J. Reimer, and A. S. Tolias. A global map of orientation tuning in mouse visual cortex. *bioRxiv*, Aug. 2019. URL https://www.biorxiv.org/content/10.1101/745323v1.

E. Froudarakis, P. Berens, A. S. Ecker, R. J. Cotton, F. H. Sinz, D. Yatsenko, P. Saggau, M. Bethge, and A. S. Tolias. Population code in mouse V1 facilitates readout of natural scenes through increased sparseness. *Nat. Neurosci.*, 17(6):851–857, June 2014.

M. E. Garrett, I. Nauhaus, J. H. Marshel, and E. M. Callaway. Topography and areal organization of mouse visual cortex. *J. Neurosci.*, 34(37):12587–12600, Sept. 2014.

D. O. Hebb. The organization of behavior; a neuropsychological theory. *A Wiley Book in Clinical Psychology*, 62:78, 1949.

S. Holler, G. Köstinger, K. A. C. Martin, G. F. P. Schuhknecht, and K. J. Stratford. Structure and function of a neocortical synapse. *Nature*, 591(7848):111–116, Mar. 2021.

C. Holmgren, T. Harkany, B. Svennenfors, and Y. Zilberter. Pyramidal cell communication within local networks in layer 2/3 of rat neocortex. *The Journal of physiology*, 551(Pt 1):139–153, Aug. 2003. ISSN 0022-3751. doi: 10.1113/jphysiol.2003.044784. URL http://dx.doi.org/10.1113/jphysiol.2003.044784.

J. Hopfield. Neural networks and physical systems with emergent collective computational abilities. *Proc. Natl. Acad. Sci. USA*, 79(8):2554–2558, 1982.

D. H. Hubel and T. N. Wiesel. Receptive fields, binocular interaction and functional architecture in the cat's visual cortex. *J. Physiol.*, 160:106–154, Jan. 1962.

M. F. Iacaruso, I. T. Gasler, and S. B. Hofer. Synaptic organization of visual space in primary visual cortex. *Nature*, 547(7664):449–452, July 2017.

M. Khona and I. Fiete. Attractor and integrator networks in the brain. *Nat. Rev. Neurosci.*, 23(12):744–766, 2022a.

M. Khona and I. R. Fiete. Attractor and integrator networks in the brain. *Nat. Rev. Neurosci.*, 23(12):744–766, Dec. 2022b.

H. Ko, S. B. Hofer, B. Pichler, K. A. Buchanan, P. J. Sjöström, and T. D. Mrsic-Flogel. Functional specificity of local synaptic connections in neocortical networks. *Nature*, 473(7345):87–91, 2011.

H. Ko, L. Cossell, C. Baragli, J. Antolik, C. Clopath, S. B. Hofer, and T. D. Mrsic-Flogel. The emergence of functional microcircuits in visual cortex. *Nature*, 496(7443):96–100, Apr. 2013.

S. Kondo and K. Ohki. Laminar differences in the orientation selectivity of geniculate afferents in mouse primary visual cortex. *Nat. Neurosci.*, 19(2):316–319, Feb. 2016.

A. T. Kuan, G. Bondanelli, L. N. Driscoll, J. Han, M. Kim, D. G. C. Hildebrand, B. J. Graham, D. E. Wilson, L. A. Thomas, S. Panzeri, C. D. Harvey, and W.-C. A. Lee. Synaptic wiring motifs in posterior parietal cortex support decision-making. *Nature*, Feb. 2024.

K. Lee, J. Zung, P. Li, V. Jain, and H. Sebastian Seung. Superhuman accuracy on the SNEMI3D connectomics challenge. *arXiv*, May 2017.

W.-C. A. Lee, V. Bonin, M. Reed, B. J. Graham, G. Hood, K. Glattfelder, and R. C. Reid. Anatomy and function of an excitatory network in the visual cortex. *Nature*, 532(7599):370–374, Apr. 2016.

R. Lu, A. Zlateski, and H. Sebastian Seung. Large-scale image segmentation based on distributed clustering algorithms. *arXiv*, June 2021.

T. Marques, J. Nguyen, G. Fioreze, and L. Petreanu. The functional organization of cortical feedback inputs to primary visual cortex. *Nat. Neurosci.*, 21(5):757–764, May 2018.

A. Mathis, P. Mamidanna, K. M. Cury, T. Abe, V. N. Murthy, M. W. Mathis, and M. Bethge. DeepLabCut: markerless pose estimation of user-defined body parts with deep learning. *Nat. Neurosci.*, 21(9):1281–1289, Sept. 2018.

M. Mazurek, M. Kager, and S. D. Van Hooser. Robust quantification of orientation selectivity and direction selectivity. *Front. Neural Circuits*, 8:92, Aug. 2014.

MICrONS Consortium, J. Alexander Bae, M. Baptiste, A. L. Bodor, D. Brittain, J. Buchanan, D. J. Bumbarger, M. A. Castro, B. Celii, E. Cobos, F. Collman, N. M. da Costa, S. Dorkenwald, L. Elabbady, P. G. Fahey, T. Fliss, E. Froudakis, J. Gager, C. Gamlin, A. Halageri, J. Hebditch, Z. Jia, C. Jordan, D. Kapner, N. Kemnitz, S. Kinn, S. Koolman, K. Kuehner, K. Lee, K. Li, R. Lu, T. Macrina, G. Mahalingam, S. McReynolds, E. Miranda, E. Mitchell, S. S. Mondal, M. Moore, S. Mu, T. Muhammad, B. Nehoran, O. Ogedengbe, C. Papadopoulos, S. Papadopoulos, S. Patel, X. Pitkow, S. Popovych, A. Ramos, R. Clay Reid, J. Reimer, C. M. Schneider-Mizell, H. Sebastian Seung, B. Silverman, W. Silversmith, A. Sterling, F. H. Sinz, C. L. Smith, S. Suckow, Z. H. Tan, A. S. Tolias, R. Torres, N. L. Turner, E. Y. Walker, T. Wang, G. Williams, S. Williams, K. Willie, R. Willie, W. Wong, J. Wu, C. Xu, R. Yang, D. Yatsenko, F. Ye, W. Yin, and S.-C. Yu. Functional connectomics spanning multiple areas of mouse visual cortex. *bioRxiv*, July 2021. URL https://www.biorxiv.org/content/10.1101/2021.07.28.454025v3.

E. Mitchell, S. Keselj, S. Popovych, D. Buniatyan, and H. Sebastian Seung. Siamese encoding and alignment by multiscale learning with Self-Supervision. *arXiv*, Apr. 2019.

S. Musall, M. T. Kaufman, A. L. Juavinett, S. Gluf, and A. K. Churchland. Single-trial neural dynamics are dominated by richly varied movements. *Nat. Neurosci.*, 22(10):1677–1686, Oct. 2019.

I. A. Oldenburg, W. D. Hendricks, G. Handy, K. Shamardani, H. A. Bounds, B. Doiron, and H. Adesnik. The logic of recurrent circuits in the primary visual cortex. *Nature neuroscience*, 27(1):137–147, Jan. 2024. ISSN 1097-6256. doi: 10.1038/s41593-023-01510-5. URL https://www.nature.com/articles/s41593-023-01510-5.

A. Peters and M. L. Feldman. The projection of the lateral geniculate nucleus to area 17 of the rat cerebral cortex. I. general description. *J. Neurocytol.*, 5(1):63–84, Feb. 1976.

J. S. Phelps, D. G. C. Hildebrand, B. J. Graham, A. T. Kuan, L. A. Thomas, T. M. Nguyen, J. Buhmann, A. W. Azevedo, A. Sustar, S. Agrawal, M. Liu, B. L. Shanny, J. Funke, J. C. Tuthill, and W.-C. A. Lee. Reconstruction of motor control circuits in adult drosophila using automated transmission electron microscopy. *Cell*, 184(3):759–774.e18, Feb. 2021.

S. Ramón y Cajal. *Histologie du système nerveux de l'homme et des vertébrés*. 1911.

C. L. Rees, K. Moradi, and G. A. Ascoli. Weighing the evidence in peters' rule: Does neuronal morphology predict connectivity?, Feb. 2017.

R. C. Reid. From functional architecture to functional connectomics. *Neuron*, 75(2):209–217, July 2012.

J. Reimer, E. Froudarakis, C. R. Cadwell, D. Yatsenko, G. H. Denfield, and A. S. Tolias. Pupil fluctuations track fast switching of cortical states during quiet wakefulness. *Neuron*, 84(2):355–362, Oct. 2014.

D. L. Ringach, P. J. Mineault, E. Tring, N. D. Olivas, P. Garcia-Junco-Clemente, and J. T. Trachtenberg. Spatial clustering of tuning in mouse primary visual cortex. *Nat. Commun.*, 7:12270, Aug. 2016.

L. F. Rossi, K. D. Harris, and M. Carandini. Spatial connectivity matches direction selectivity in visual cortex. *Nature*, 588(7839):648–652, Dec. 2020.

C. Schneider-Mizell and F. Collman. Alleninstitute/pcg_skel: v0.3.2, Mar. 2023. URL https://doi.org/10.5281/zenodo.7703278.

C. M. Schneider-Mizell, A. L. Bodor, D. Brittain, J. Buchanan, D. J. Bumbarger, L. Elabbady, C. Gamlin, D. Kapner, S. Kinn, G. Mahalingam, S. Seshamani, S. Suckow, M. Takeno, R. Torres, W. Yin, S. Dorkenwald, J. A. Bae, M. A. Castro, A. Halageri, Z. Jia, C. Jordan, N. Kemnitz, K. Lee, K. Li, R. Lu, T. Macrina, E. Mitchell, S. S. Mondal, S. Mu, B. Nehoran, S. Popovych, W. Silversmith, N. L. Turner, W. Wong, J. Wu, MICrONS Consortium, J. Reimer, A. S. Tolias, H. S. Seung, R. C. Reid, F. Collman, and N. Maçarico da Costa. Cell-type-specific inhibitory circuitry from a connectomic census of mouse visual cortex. *bioRxiv*, Jan. 2024. URL https://www.biorxiv.org/content/10.1101/2023.01.23.525290v3.

B. Scholl, C. I. Thomas, M. A. Ryan, N. Kamasawa, and D. Fitzpatrick. Cortical response selectivity derives from strength in numbers of synapses. *Nature*, 590(7844):111–114, Feb. 2021.

O. Schoppe, N. S. Harper, B. D. B. Willmore, A. J. King, and J. W. H. Schnupp. Measuring the performance of neural models. *Frontiers in Computational Neuroscience*, 10, Feb. 2016. doi: 10.3389/fncom.2016.00010.

N. J. Sofroniew, D. Flickinger, J. King, and K. Svoboda. A large field of view two-photon mesoscope with subcellular resolution for in vivo imaging. *Elife*, 5, June 2016.

C. Stringer, M. Pachitariu, N. Steinmetz, C. B. Reddy, M. Carandini, and K. D. Harris. Spontaneous behaviors drive multidimensional, brainwide activity. *Science*, 364(6437):255, Apr. 2019.

R. Tong, R. da Silva, D. Lin, A. Ghosh, J. Wilsenach, E. Cianfarano, P. Bashivan, B. Richards, and S. Trenholm. The feature landscape of visual cortex. *bioRxiv*, 2023. doi: 10.1101/2023.11.03.565500. URL https://www.biorxiv.org/content/early/2023/11/05/2023.11.03.565500.

N. L. Turner, K. Lee, R. Lu, J. Wu, D. Ih, and H. S. Seung. Synaptic partner assignment using attentional voxel association networks. *2020 IEEE 17th International Symposium on Biomedical Imaging (ISBI)*, pages 1–5, Apr. 2020.

P. Virtanen, R. Gommers, T. E. Oliphant, M. Haberland, T. Reddy, D. Cournapeau, E. Burovski, P. Peterson, W. Weckesser, J. Bright, S. J. van der Walt, M. Brett, J. Wilson, K. J. Millman, N. Mayorov, A. R. J. Nelson, E. Jones, R. Kern, E. Larson, C. J. Carey, Polat, Y. Feng, E. W. Moore, J. VanderPlas, D. Laxalde, J. Perktold, R. Cimrman, I. Henriksen, E. A. Quintero, C. R. Harris, A. M. Archibald, A. H. Ribeiro, F. Pedregosa, P. van Mulbregt, and SciPy 1.0 Contributors. SciPy 1.0: fundamental algorithms for scientific computing in python. *Nat. Methods*, 17(3):261–272, Mar. 2020.

E. Y. Walker, F. H. Sinz, E. Cobos, T. Muhammad, E. Froudarakis, P. G. Fahey, A. S. Ecker, J. Reimer, X. Pitkow, and A. S. Tolias. Inception loops discover what excites neurons most using deep predictive models. *Nat. Neurosci.*, 22(12):2060–2065, Dec. 2019.

E. Y. Wang, P. G. Fahey, Z. Ding, S. Papadopoulos, K. Ponder, M. A. Weis, A. Chang, T. Muhammad, S. Patel, Z. Ding, D. Tran, J. Fu, C. M. Schneider-Mizell, R. C. Reid, F. Collman, N. M. da Costa, K. Franke, A. S. Ecker, J. Reimer, X. Pitkow, F. H. Sinz, and A. S. Tolias. Foundation model of neural activity predicts response to new stimulus types and anatomy. *bioRxiv*, Aug. 2024. URL https://www.biorxiv.org/content/10.1101/2023.03.21.533548v4.

Q. Wang and A. Burkhalter. Area map of mouse visual cortex. *J. Comp. Neurol.*, 502(3):339–357, May 2007.

A. A. Wanner, C. Genoud, T. Masudi, L. Siksou, and R. W. Friedrich. Dense EM-based reconstruction of the interglomerular projectome in the zebrafish olfactory bulb. *Nat. Neurosci.*, 19(6):816–825, June 2016.

M. A. Weis, S. Papadopoulos, L. Hansel, T. Lüddecke, B. Celii, P. G. Fahey, E. Y. Wang, J. A. Bae, A. L. Bodor, D. Brittain, J. Buchanan, D. J. Bumbarger, M. A. Castro, F. Collman, N. M. da Costa, S. Dorkenwald, L. Elabbady, A. Halageri, Z. Jia, C. Jordan, D. Kapner, N. Kemnitz, S. Kinn, K. Lee, K. Li, R. Lu, T. Macrina, G. Mahalingam, E. Mitchell, S. S. Mondal, S. Mu, B. Nehoran, S. Popovych, R. C. Reid, C. M. Schneider-Mizell, H. S. Seung, W. Silversmith, M. Takeno, R. Torres, N. L. Turner, W. Wong, J. Wu, W. Yin, S.-C. Yu, J. Reimer, P. Berens, A. S. Tolias, and A. S. Ecker. An unsupervised map of excitatory neurons' dendritic morphology in the mouse visual cortex. *bioRxiv*, Apr. 2024. URL https://www.biorxiv.org/content/10.1101/2022.12.22.521541v3.

A. Wertz, S. Trenholm, K. Yonehara, D. Hillier, Z. Raics, M. Leinweber, G. Szalay, A. Ghanem, G. Keller, B. Rózsa, K.-K. Conzelmann, and B. Roska. PRESYNAPTIC NETWORKS. single-cell-initiated monosynaptic tracing reveals layer-specific cortical network modules. *Science*, 349(6243):70–74, July 2015.

J. Wu, W. M. Silversmith, K. Lee, and H. S. Seung. Chunkflow: hybrid cloud processing of large 3D images by convolutional nets. *Nat. Methods*, 18(4):328–330, Apr. 2021.

D. Yamins, H. Hong, C. Cadieu, E. A. Solomon, D. Seibert, and J. DiCarlo. Performance-optimized hierarchical models predict neural responses in higher visual cortex. *Proc. Natl. Acad. Sci. USA*, 111(23):8619–8624, 2014.

W. Yin, D. Brittain, J. Borseth, M. E. Scott, D. Williams, J. Perkins, C. S. Own, M. Murfitt, R. M. Torres, D. Kapner, G. Mahalingam, A. Bleckert, D. Castelli, D. Reid, W.-C. A. Lee, B. J. Graham, M. Takeno, D. J. Bumbarger, C. Farrell, R. C. Reid, and N. M. da Costa. A petascale automated imaging pipeline for mapping neuronal circuits with high-throughput transmission electron microscopy. *Nat. Commun.*, 11(1):4949, Oct. 2020.

Z. Yu, M. Guindani, S. F. Grieco, L. Chen, T. C. Holmes, and X. Xu. Beyond t test and ANOVA: applications of mixed-effects models for more rigorous statistical analysis in neuroscience research. *Neuron*, 110(1):21–35, Jan. 2022.

P. Znamenskiy, M.-H. Kim, D. R. Muir, M. F. Iacaruso, S. B. Hofer, and T. D. Mrsic-Flogel. Functional specificity of recurrent inhibition in visual cortex. *Neuron*, 112(6):991–1000.e8, Mar. 2024.

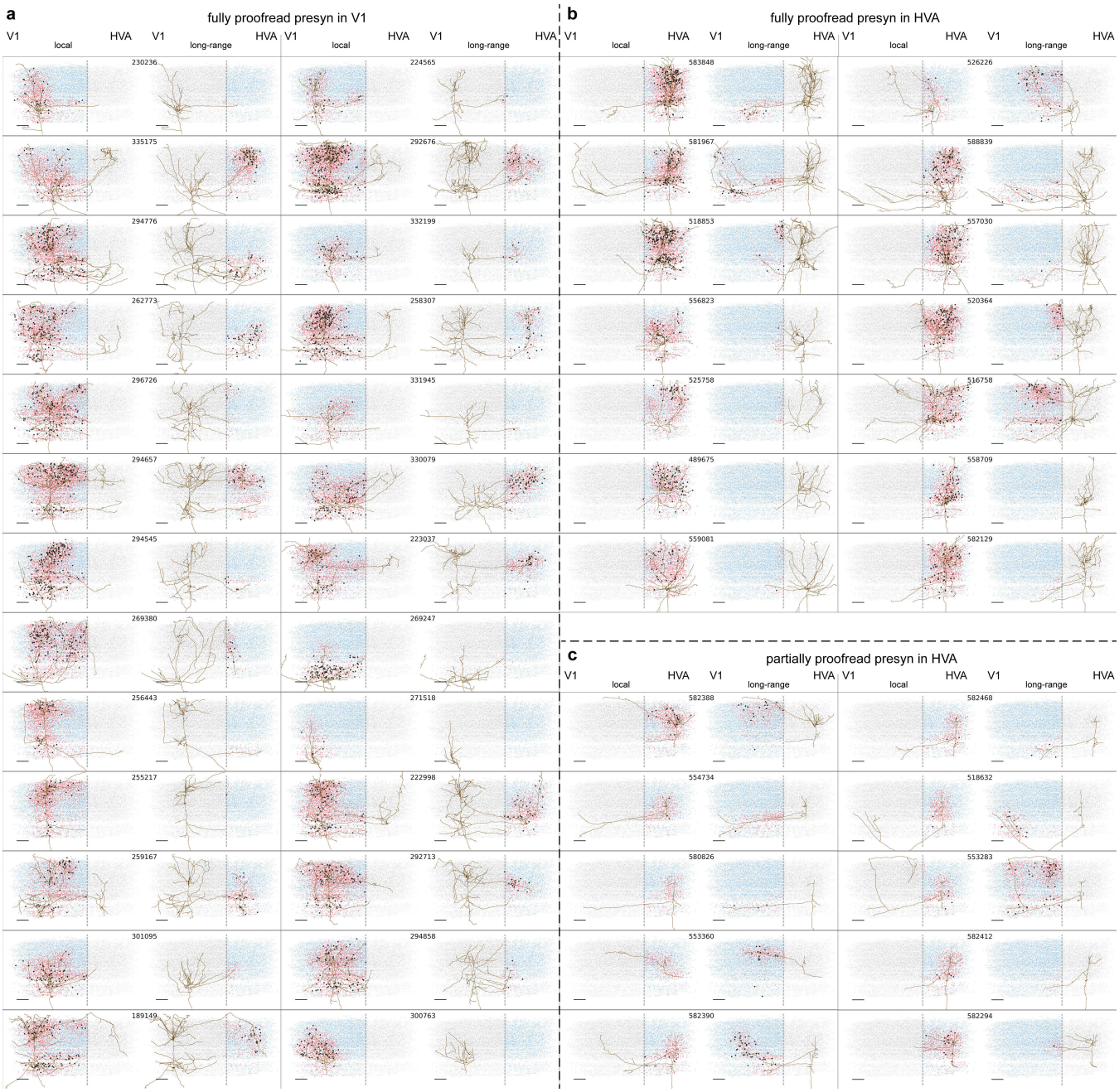

Supplemental Figure 1. Example proofread presynaptic axons in EM cortical space and their connected, ADP, and same region controls. The axon for every presynaptic (presyn) neuron is shown twice, once as a "local" projection type and again as a "long-range" type (even if the neuron has no local or long-range projections). The six digit ID from Table “nucleus_detection_v0" (MICrONS Consortium et al., 2021) is displayed above both plots. For each plot, the soma centroids of connected neurons, ADP controls, and same region controls are plotted in black, red, and blue, respectively. Gray dots are soma centroids of all other functionally matched neurons not used as controls for that presyn. The dashed gray line represents the V1-HVA boundary. Scale bar = $100\mu m$. **a**, Example fully proofread presynaptic axons with somas in V1. “Fully proofread” neurons are those where a proofreader attempted to extend every axonal branch to completion. **b**, Example fully proofread presynaptic axons with somas in HVA **c**, Example partially proofread presynaptic axons with somas in HVA. “Partially proofread” neurons are those where a proofreader only extended axonal branches that were pre-screened for whether they projected inter-areally (specifically to enrich for feedback connections).

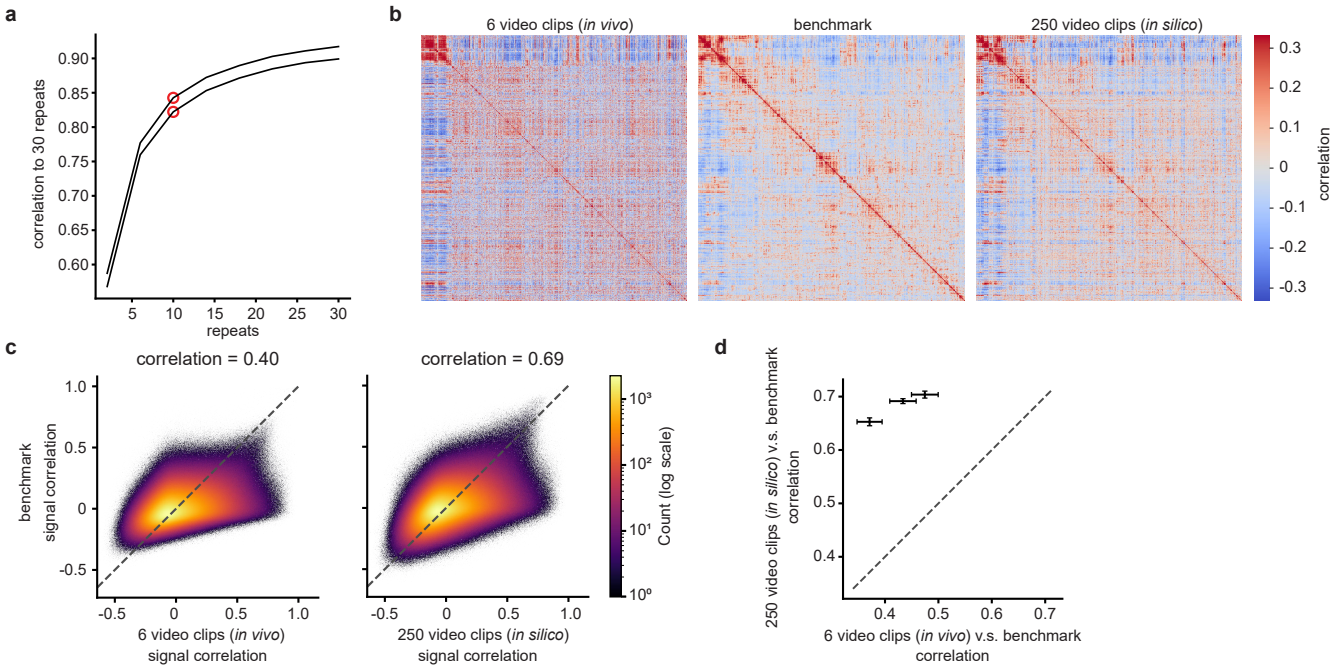

Supplemental Figure 2. The digital twin signal correlations align better with the *in vivo* benchmark than *in vivo* signal correlations generated with less data. **a**, Correlation of *in vivo* signal correlations generated with 6 video clips and varying numbers of repeats to *in vivo* signal correlations generated with 6 clips and 30 repeats, for two animals. 10 repeats (red marker) reasonably approximates the saturation point and is the number used for all other analyses. **b**, Signal correlation matrices of 1000 neurons generated from *in vivo* responses to 6 video clips (left), *in vivo* responses to 30 video clips (benchmark, middle) and digital twin responses to 250 video clips (*in silico*, right). The benchmark matrix is ordered by ward's hierarchical clustering. The *in vivo* and *in silico* signal correlation matrices are ordered in the same order as the benchmark matrix. The fine structure of the *in silico* matrix is qualitatively more similar to the benchmark than the *in vivo* matrix generated with 6 video clips is to the benchmark. **c**, 2D heatmaps of signal correlations from the benchmark (same benchmark as in **b**) vs *in vivo* responses to 6 video clips (left) and *in silico* responses to 250 clips (right). The correlation of *in silico* signal correlations to the benchmark is higher than the correlation of *in vivo* signal correlations generated with 6 video clips to the benchmark (0.69 vs 0.40). Colorbar: 2D bin counts in log scale. **d**, The correlation of *in silico* signal correlations to the benchmark vs the correlation of *in vivo* signal correlations generated with 6 video clips to the benchmark for three animals. Error bars are standard deviations estimated through resampling. All data points are in the upper left corner indicating that *in silico* signal correlations outperform *in vivo* signal correlations generated with 6 video clips. (p-value < 0.001 for all three animals)

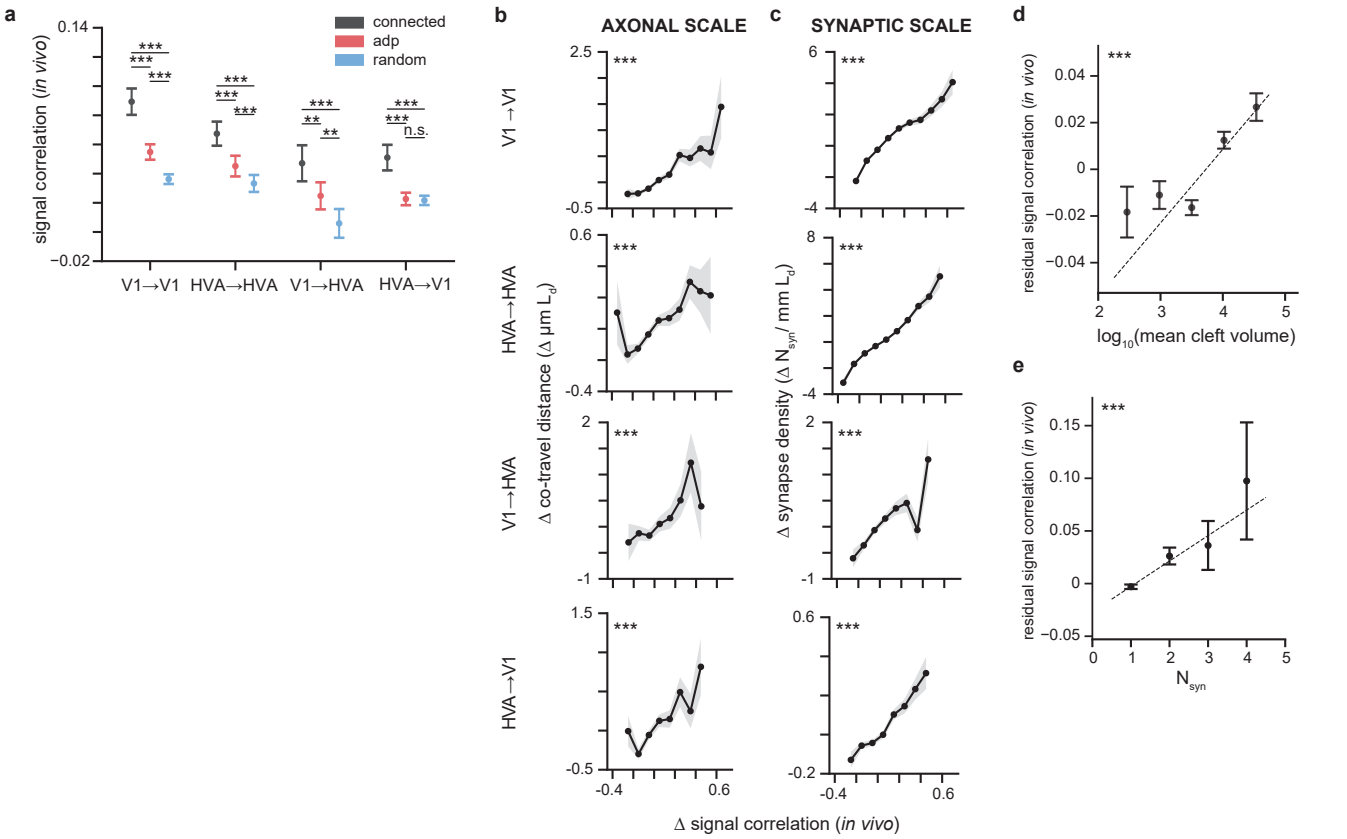

Supplemental Figure 3. Synaptic connectivity increases with empirical signal correlations measured directly *in vivo* rather than via the digital twin. a, Mean *in vivo* signal correlation is different (mean ± sem, paired t-test) for connected pairs, ADP controls, and same area controls for all projection types, as in Fig 2d. **b**, Axon-dendrite co-travel distance ($\mu m L_d$) increases in a graded fashion with *in vivo* signal correlation for all projection types, as in Fig 2e. **c** Synapse density ($N_{syn}/mm L_d$) increases in a graded fashion with signal correlation, for all projection types, as in Fig 2f. The shaded regions in **b** and **c** are bootstrap-based standard deviation. **d**, Synapse size (log_{10} cleft volume in voxels) is positively correlated with *in vivo* signal correlation after regressing out L_d (p-value by linear regression), as in Fig 2h. **e**, *In vivo* signal correlations increases with number of synapses after regressing out L_d (p-values by linear regression), as in Fig 2j. (For all panels, $*$ = p-value < 0.05, $**$ = p-value < 0.01, $***$ = p-value < 0.001, multiple comparison correction by BH procedure)

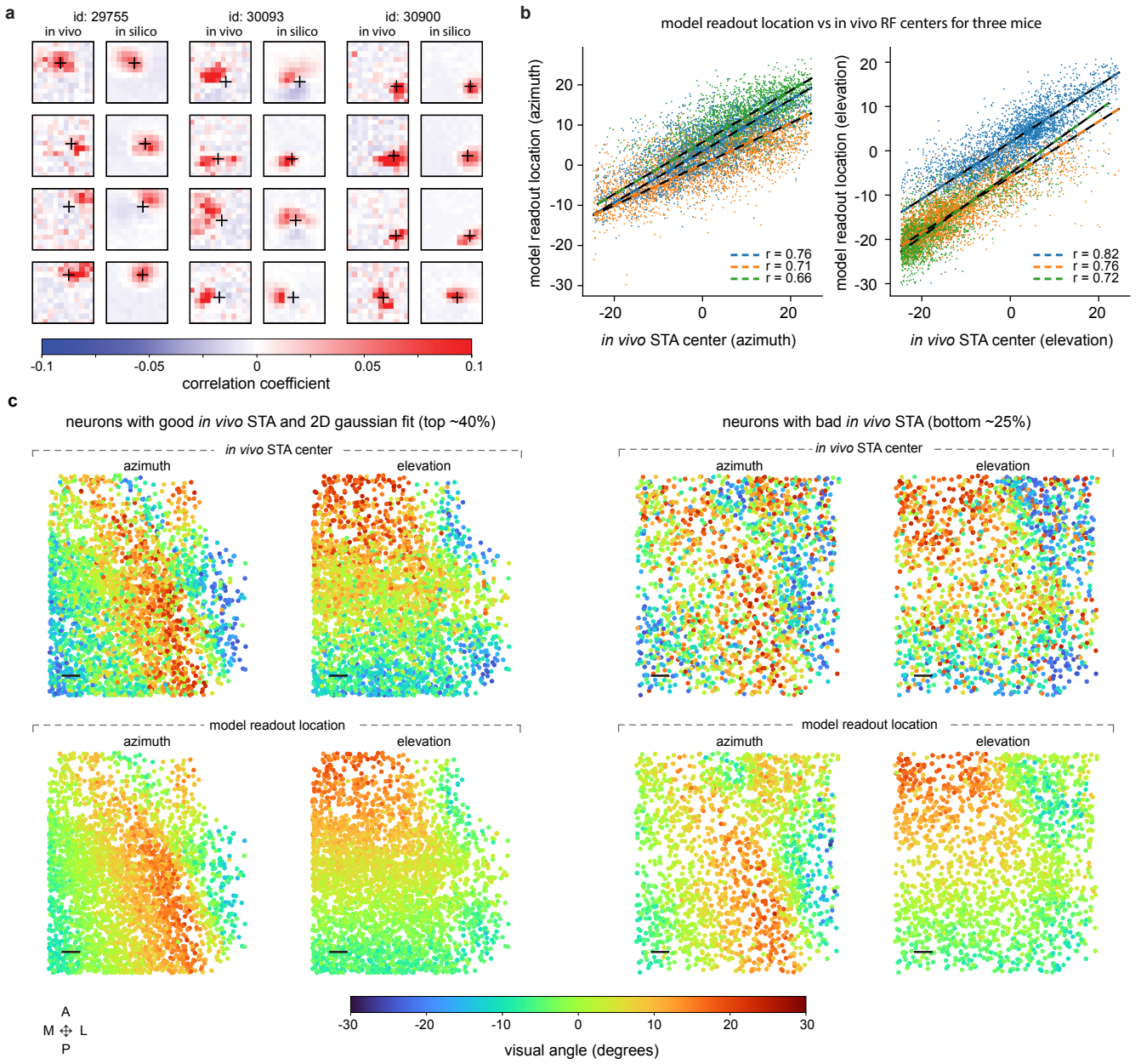

Supplemental Figure 4. Model readout center aligns with receptive field center measured *in vivo* with sparse noise stimuli. **a**, Visual comparison of STAs generated from *in vivo* responses to a sparse noise stimulus (left) vs STAs generated from *in silico* responses to the same stimulus (right) for three animals (blue, orange, and green). The black cross represents the model readout location. Examples are randomly chosen from the top ≈ 40% of neurons remaining after a threshold on *in vivo* STA quality is applied. **b**, Model readout location vs *in vivo* STA center for azimuth coordinate (left) and elevation coordinate (right). **c**, Retinotopic maps for animal id: 29755. Left: Maps generated with top ≈ 40% of neurons after an *in vivo* STA quality threshold is applied. Right: Maps for the bottom ≈ 25% of neurons. Top row: maps generated from *in vivo* STA's centers. Bottom row: maps generated from the digital twin model readout location. The maps generated from the model are qualitatively less noisy, even for maps generated from neurons with poor STA quality. Colorbar: degree of visual angle for both azimuth and elevation coordinates. Anatomical axes: A = anterior, P = posterior, M = medial, L = lateral. Scale bar: 100 μm.

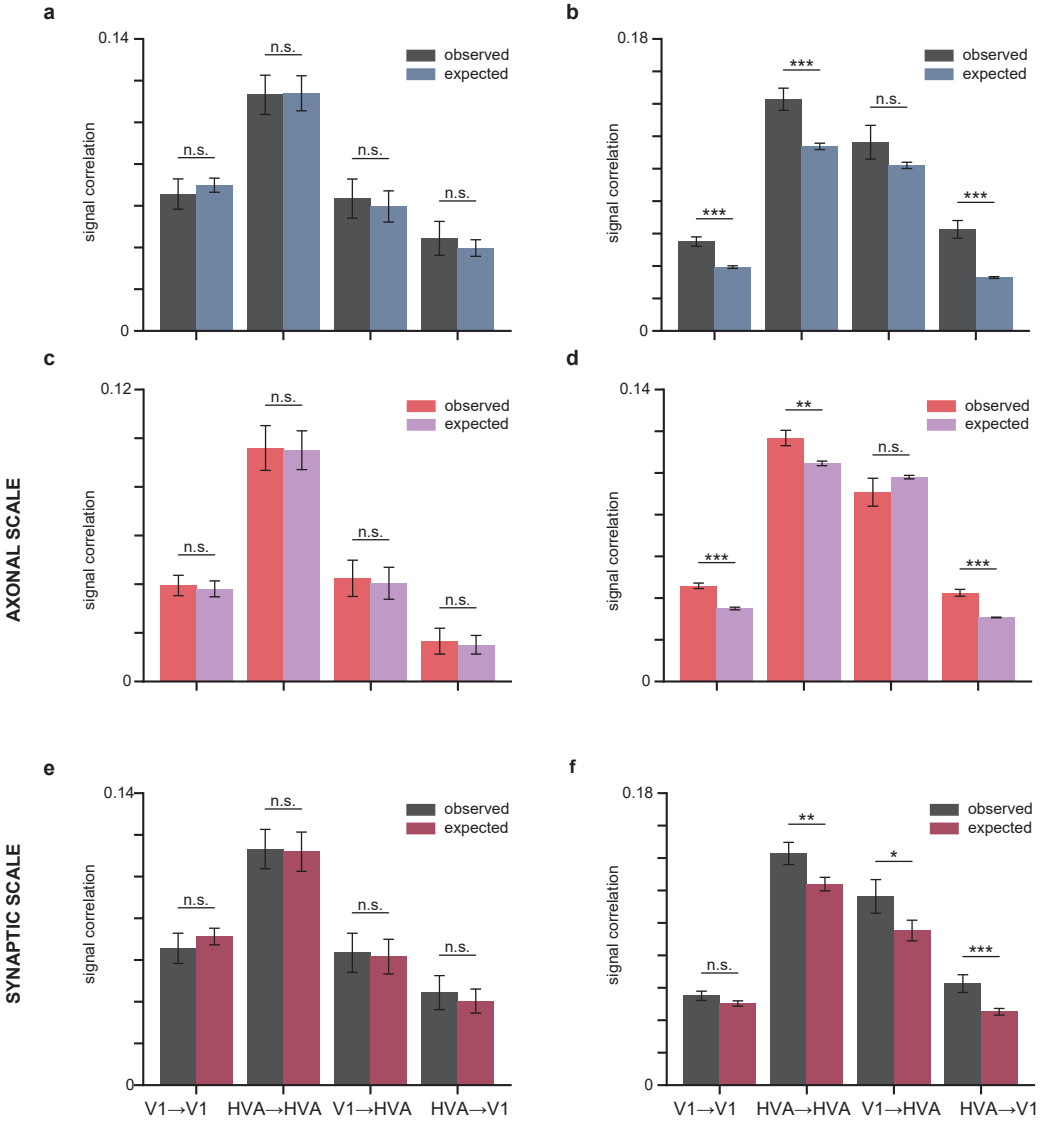

Supplemental Figure 5. Postsyns with a common input are more similar to each other than expected by a pairwise like-to-like rule at both axonal and synaptic scale. a, Mean pre-post signal correlations in the data (dark gray, "observed") and the model (blue, "expected") are not significantly different, indicating that the model reproduces the expected pairwise like-to-like rule **b**, Mean pairwise *in silico* signal correlation of postsyns, reproduced from Fig 5c. The observed data shows significantly higher postsyn to postsyn similarity than predicted by the model fit with only a pairwise rule, for three out of four projection types. **c**, As in **a**, but at “Axonal" scale. **d**, As in **b**, but at “Axonal" scale. **e**, As in **c**, but at “Synaptic" scale. **f**, As in **d**, but at “Synaptic" scale.

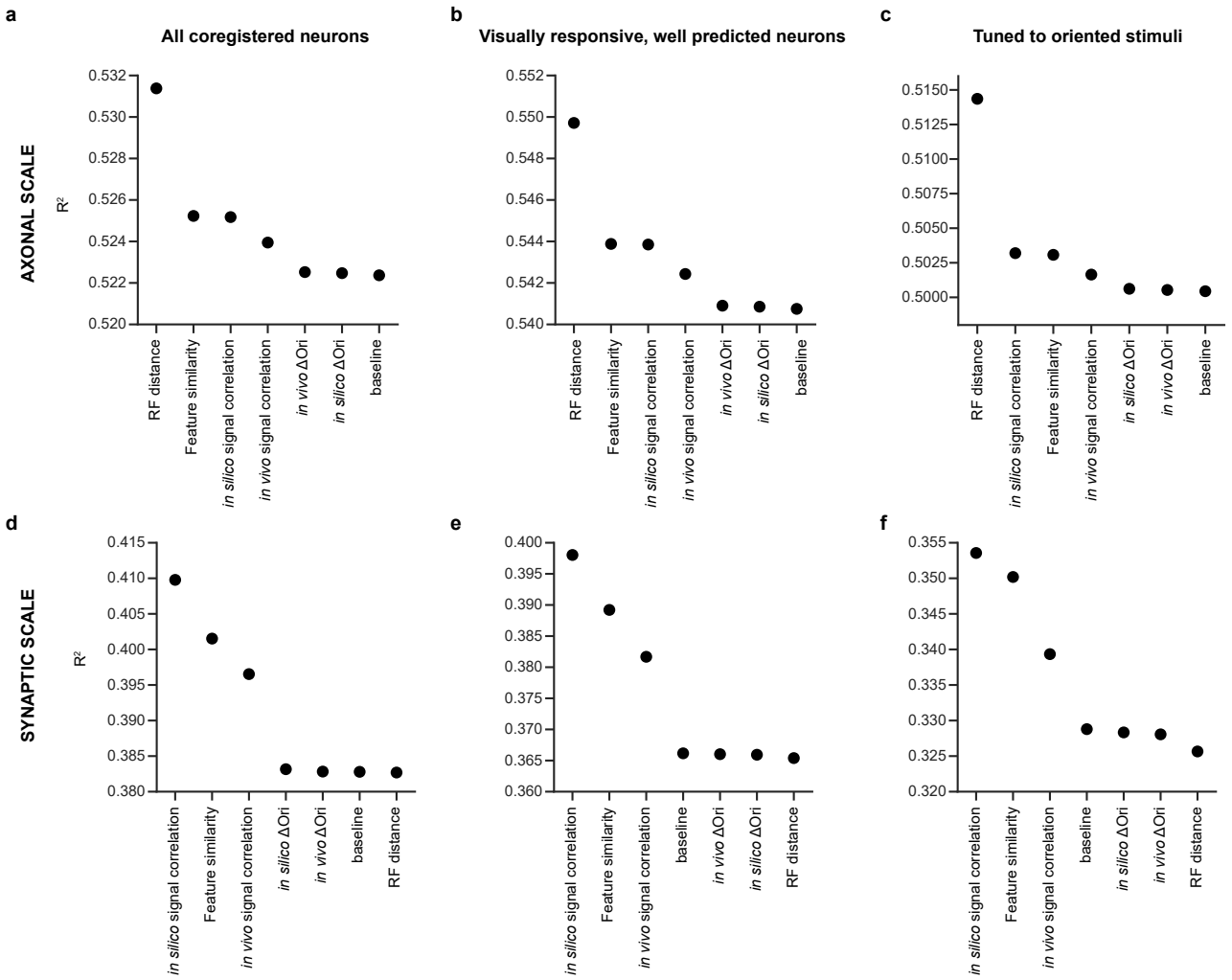

Supplemental Figure 6. Performance of various functional metrics in predicting axon-dendrite co-travel distance (L_d, Axonal scale) or synapse density (N_{syn}/mmL_d, Synaptic scale). Model performance of GLMMs (Nakagawa's conditional R^2) for predicting axon-dendrite co-travel distance (L_d): **a**, **b**, **c** and synapse density (N_{syn}/mmL_d): **d**, **e**, **f**, for all coregistered neurons: **a**, **d**, all visually responsive, well predicted neurons: **b**, **e**, and neurons tuned to oriented stimuli: **c**, **f**. The GLMMs are fit to predict axon-dendrite co-travel distance or synapse density independently with each functional metric, the projection type, and the interaction between the two while considering the interaction term of projection type and presynaptic neuron identity as random effects. The baseline models were not fitted with information about functional metrics. They predict axon-dendrite co-travel distance or synapse density with the projection type alone while considering the interaction term of projection type and presynaptic neuron identity as random effects.

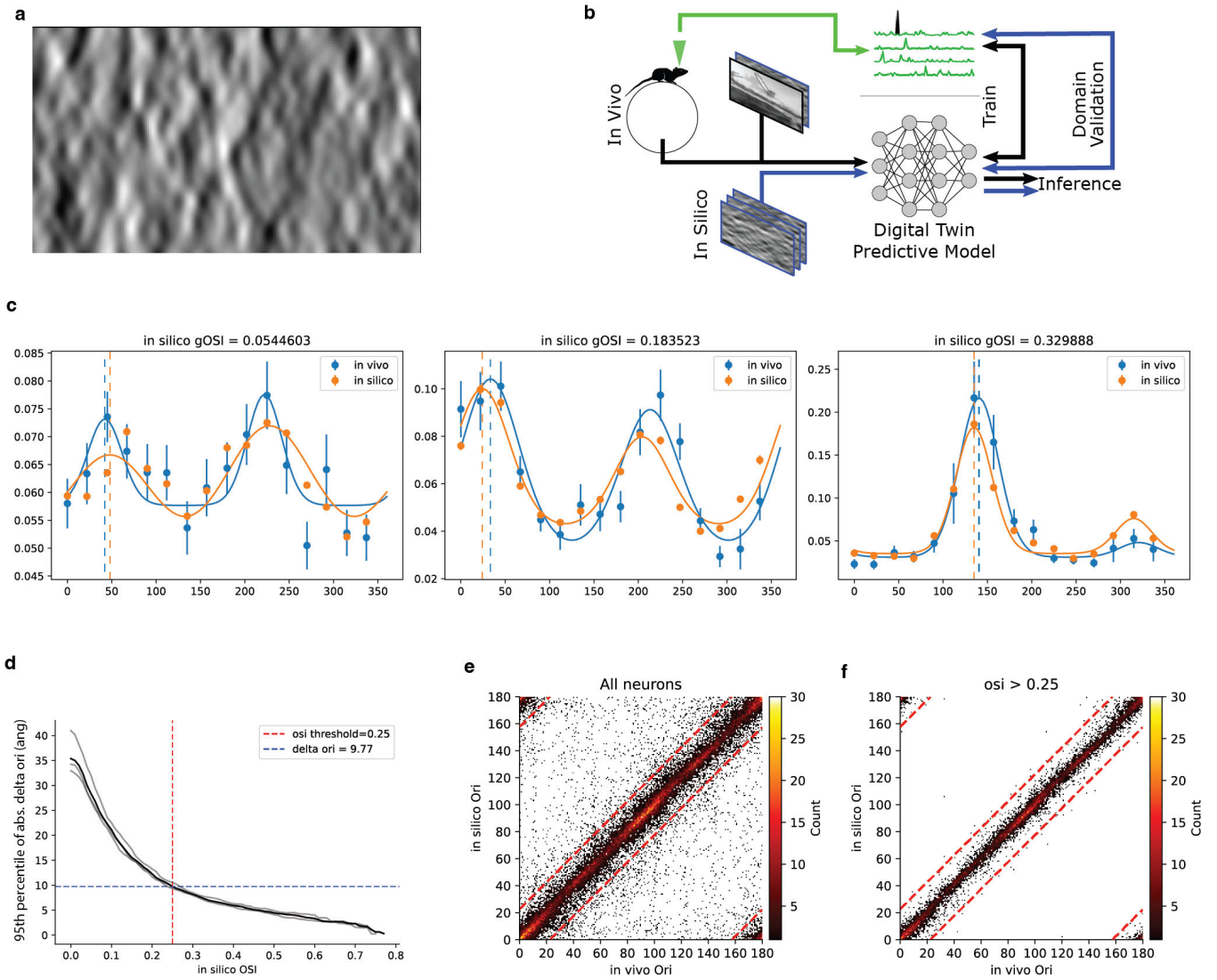

Supplemental Figure 7. In silico orientation tuning is consistent with in vivo orientation tuning a, Sample frame from global directional parametric stimulus ("Monet") used to characterize orientation and direction selectivity. Directional motion was orthogonal to orientation, and was tested at 22.5°intervals. **b**, Schematic of domain validation experimental design. In a single scan in a new animal, neuronal responses are collected in response to sufficient stimuli to both train the digital twin model (natural stimuli) and characterize orientation tuning (Monet) from *in vivo* responses. Later, *in silico* orientation tuning is extracted from model responses to parametric stimuli, and compared against *in vivo* orientation tuning for the same neurons. **c**, Comparison of *in silico* and *in vivo* mean responses per stimulus direction (mean $\pm$ SEM), fitted tuning curves (lines), and extracted preferred orientation (dotted lines) for three neurons. **d**, 95th percentile difference in preferred orientation between *in silico* and *in vivo* fitted responses as a function of gOSI threshold. Dotted lines correspond to gOSI > 0.25 threshold applied for all analyses and resulting 95th percentile difference in preferred orientation $\approx 9.77°$ across all three animals imaged. Lines correspond to individual animals (gray) or cumulative across all animals (black). **e, f**, Two-dimensional histogram of *in silico* versus *in vivo* preferred orientation for all neurons across three animals (**e**) and only neurons with gOSI > 0.25 (**f**).

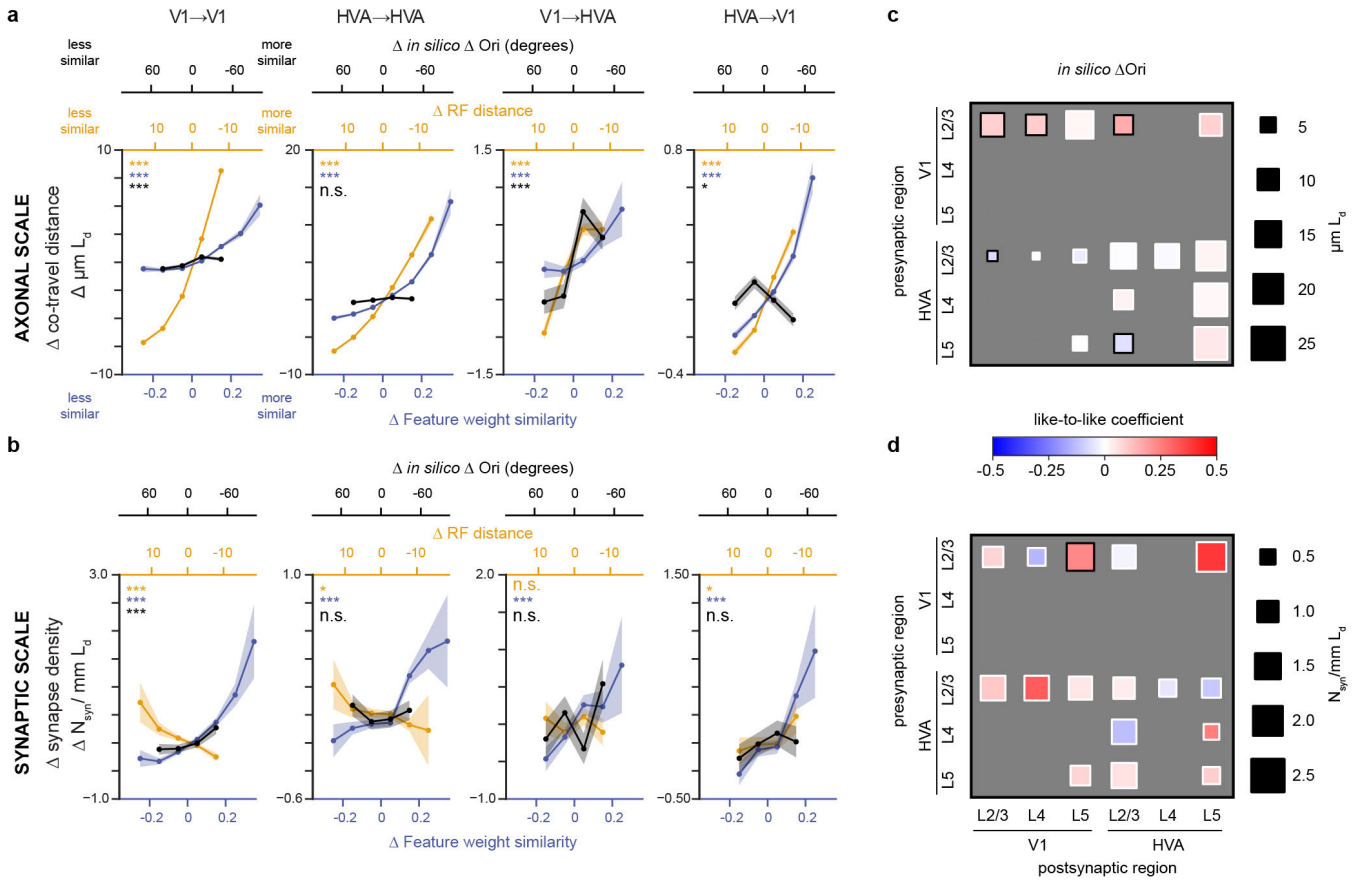

Supplemental Figure 8. Analysis repeated with *in silico* orientation preference. **a**, Difference in preferred orientation (Δ Ori) derived from *in silico* responses to parametric stimuli for tuned (gOSI > 0.25) neurons along with both feature weight similarity and receptive field center distance (reproduced from Fig 3) at axonal scale. **b**, same as in **a**, at synaptic scale. **c**, Area/ layer joint membership breakout as in Fig 4 for *in silico* Δ ori at axonal scale. **d**, As in **c** but at synaptic scale. All analyses are centered per presyn by accounting for the presyn mean (e.g. Δ feature weight similarity). For details, see Supplemental Tab. 13, 14, 17, 18, 21, 22, 31, 32,

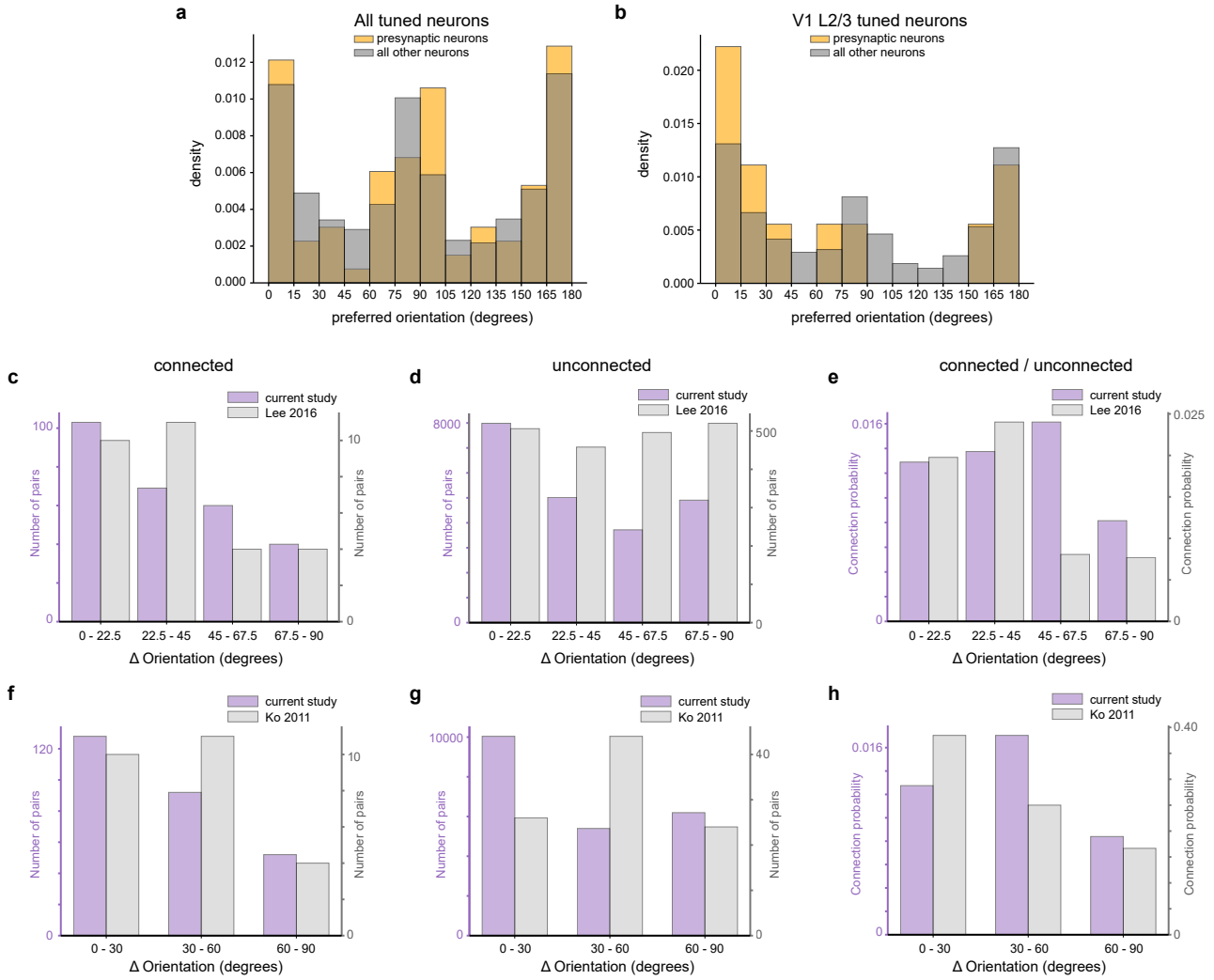

Supplemental Figure 9. Distribution of *in silico* orientation preference and comparison to previous literature. **a**, Distribution of orientation preference of tuned neurons (gOSI > 0.25) derived from *in silico* responses to parametric stimuli (see Methods). Note the cardinal bias in orientation preference distribution, in which orientation preference for 0 and 90 degree angles is overrepresented. Gold: presynaptic neurons, Gray: all other neurons. **b**, As in **a** but for tuned neurons in V1 L2/3. Difference in preferred orientation (Δ Orientation) for neurons in V1 L2/3 for connected pairs (**c, f**), unconnected pairs (**d, g**), and the ratio of connected / unconnected ("connection probability", **e, h**) for our study vs Lee et al. 2016 (**c-e**) and vs Ko et al. 2011 (**f-h**). The connected V1 L2/3 neurons in our study show a strong like-to-like effect, consistent with both Lee et al. 2016 and Ko et al. 2011 (**c, f**), however unlike Lee et al. 2016 and Ko et al. 2011, the unconnected neurons in our study also show a strong like-to-like effect (**d, g**) indicating that the like-to-like effect seen in connected pairs results from an orientation preference bias. This bias likely explains why we do not observe significant a like-to-like effect between V1 L2/3 neurons at axonal scale or synaptic scale in Supplemental. Fig 8, (i.e. when pairs are tested against region-matched controls).

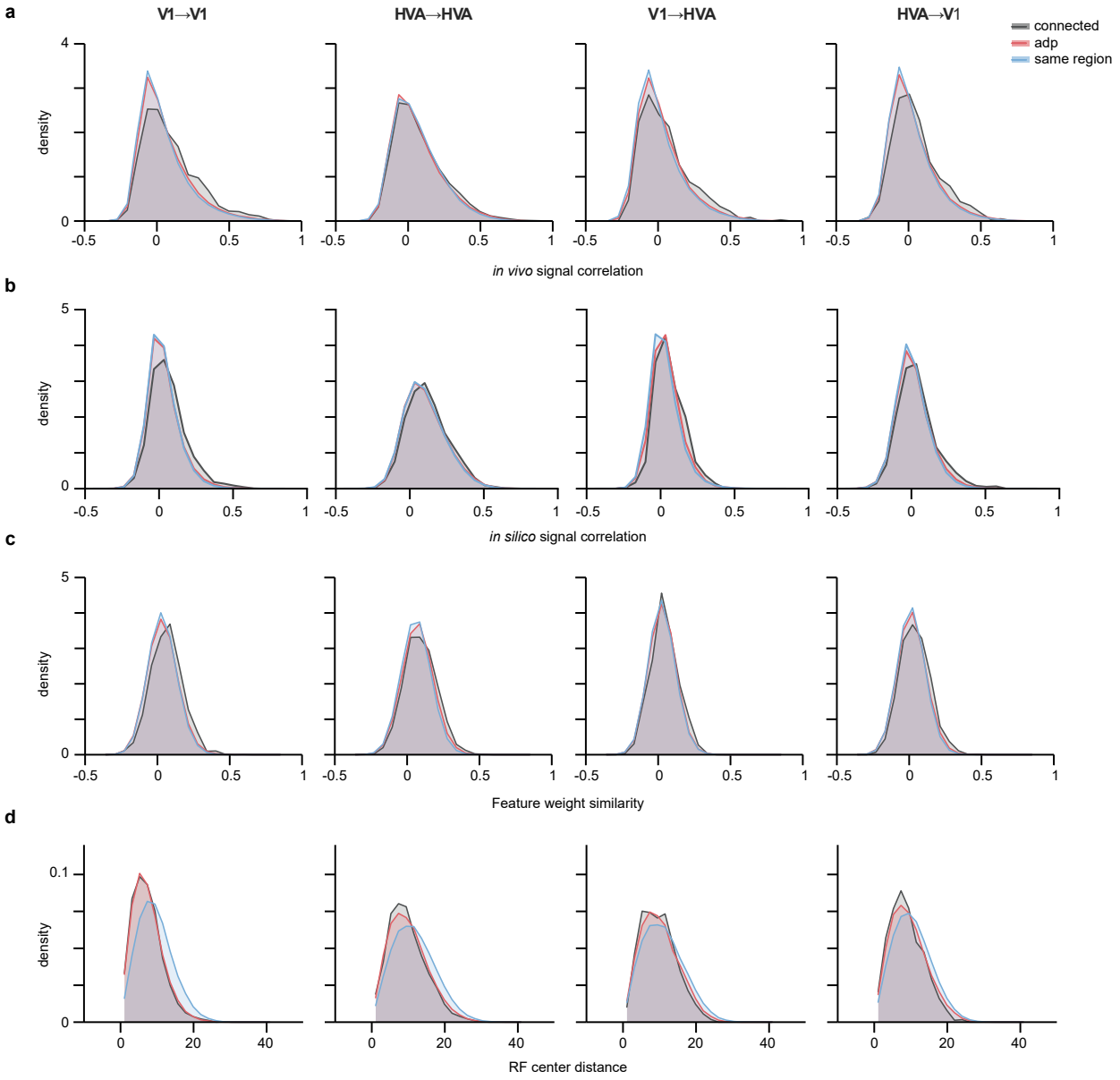

Supplemental Figure 10. Distribution of pairwise functional measurements. Density distribution of connected pairs (black), ADP control pairs (red) and same region control pairs (blue) for *in vivo* signal correlations (**a**), *in silico* signal correlations (**b**), feature weight similarity (**c**), and RF center distance (**d**) for all projection types.

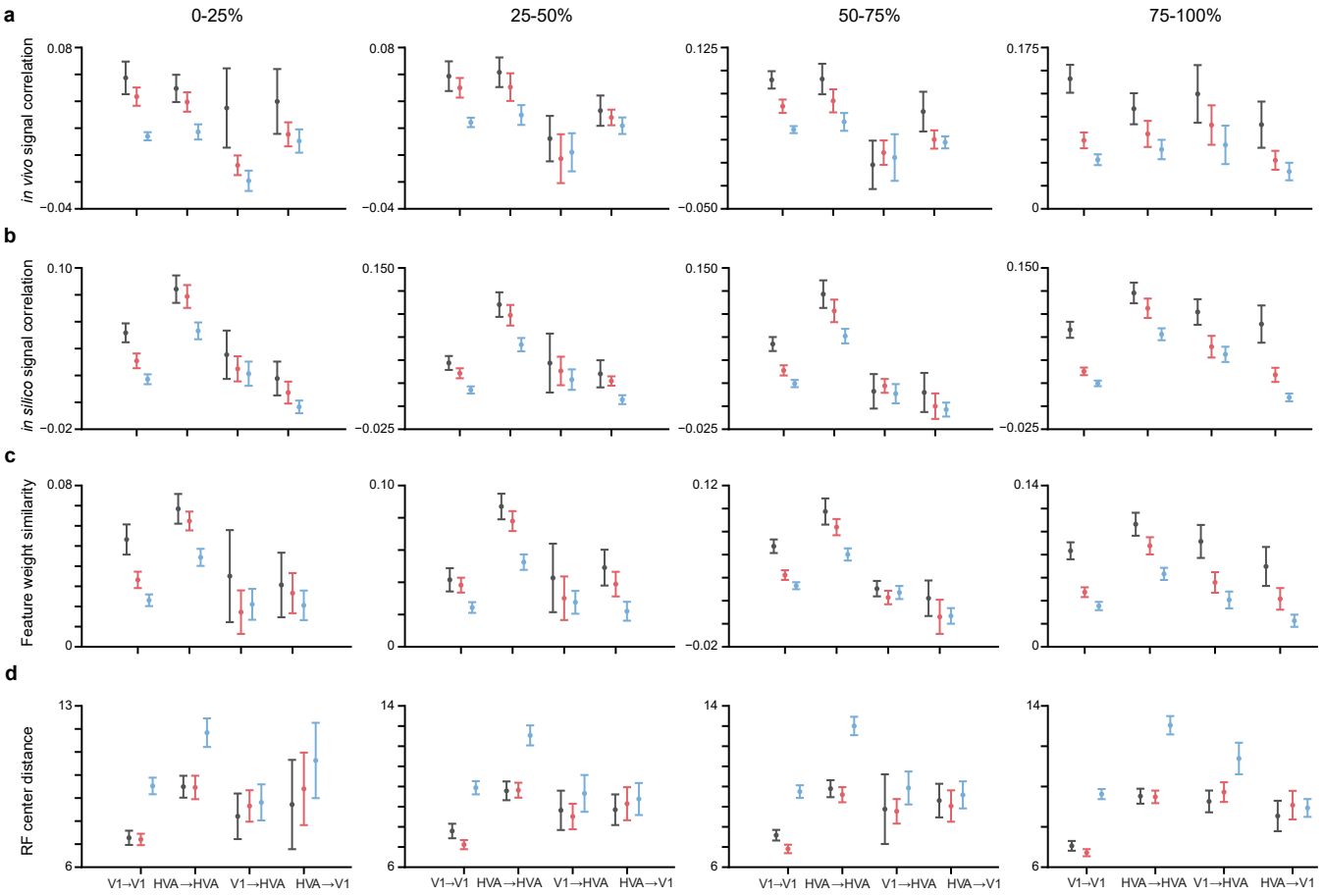

Supplemental Figure 11. Pairwise functional measurements across varying levels of model predictive performance. Mean of *in vivo* signal correlations (**a**), *in silico* signal correlations (**b**), feature weight similarity (**c**), and RF center distance (**d**) for all projection types across 4 quantiles of model predictive performance (CC_{abs}). All panels share a base filtering for visual responsiveness (CC_{max} > 0.4, 90% of neurons pass this threshold). Presynaptic neurons are filtered to CC_{abs} > 0.2 (4 did not pass this threshold).

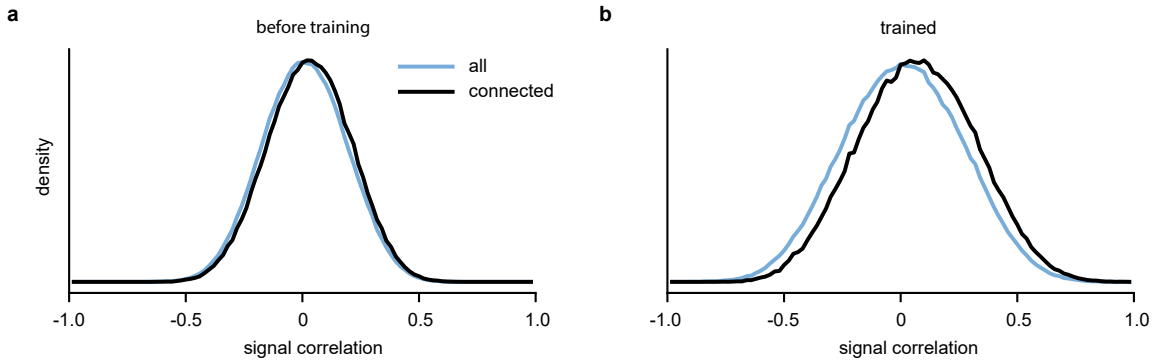

Supplemental Figure 12. Signal correlation distributions for connected neurons vs all neurons in the RNN before and after training.

a, Signal correlation distribution for connected neurons vs all neurons in the RNN before training. A neuron pair was classified as connected if the associated weight was in the top 35^{th} percentile of all weights. **b**, Same as **a** except after training.

Supplemental Table 1. Proofread presynaptic neuron nucleus ID's, area, layer, and proofreading strategy. nucleus_id's are from CAVE table `nucleus_detection_v0`

index	nucleus_id	area	layer	proofreading strategy
1	189149	V1	L2/3	full cleaning and extension
2	222998	V1	L2/3	full cleaning and extension
3	223037	V1	L2/3	full cleaning and extension
4	224565	V1	L2/3	full cleaning and extension
5	225498	V1	L4	full cleaning and extension
6	230236	V1	L5	full cleaning and extension
7	236197	V1	L6	full cleaning and extension
8	255217	V1	L2/3	full cleaning and extension
9	256443	V1	L2/3	full cleaning and extension
10	256576	V1	L2/3	full cleaning and extension
11	258307	V1	L2/3	full cleaning and extension
12	259167	V1	L2/3	full cleaning and extension
13	262773	V1	L4	full cleaning and extension
14	264870	V1	L4	full cleaning and extension
15	269247	V1	L6	full cleaning and extension
16	269380	V1	L6	full cleaning and extension
17	271518	V1	L6	full cleaning and extension
18	292676	V1	L2/3	full cleaning and extension
19	292685	V1	L2/3	full cleaning and extension
20	292713	V1	L2/3	full cleaning and extension
21	294484	V1	L2/3	full cleaning and extension
22	294545	V1	L2/3	full cleaning and extension
23	294657	V1	L2/3	full cleaning and extension
24	294776	V1	L2/3	full cleaning and extension
25	294858	V1	L2/3	full cleaning and extension
26	294897	V1	L2/3	full cleaning and extension
27	296726	V1	L2/3	full cleaning and extension
28	300763	V1	L5	full cleaning and extension
29	301095	V1	L5	full cleaning and extension
30	301189	V1	L5	full cleaning and extension
31	327859	V1	L2/3	full cleaning and extension
32	330079	V1	L4	full cleaning and extension
33	330326	V1	L4	full cleaning and extension
34	331945	V1	L5	full cleaning and extension
35	332199	V1	L4	full cleaning and extension
36	335175	V1	L5	full cleaning and extension
37	460053	RL	L4	full cleaning and extension
38	460391	RL	L5	full cleaning and extension
39	487512	RL	L2/3	full cleaning and extension
40	489675	RL	L2/3	full cleaning and extension
41	493419	RL	L5	full cleaning and extension
42	493806	RL	L5	full cleaning and extension
43	493885	RL	L5	full cleaning and extension
44	493968	RL	L4	full cleaning and extension
45	516758	RL	L2/3	full cleaning and extension
46	517056	RL	L2/3	full cleaning and extension
47	518848	RL	L2/3	full cleaning and extension
48	518853	AL	L2/3	full cleaning and extension
49	518898	RL	L2/3	full cleaning and extension
50	520364	RL	L4	full cleaning and extension
51	522656	RL	L4	full cleaning and extension
52	524491	RL	L5	full cleaning and extension
53	525405	RL	L5	full cleaning and extension
54	525498	RL	L5	full cleaning and extension
55	525758	RL	L5	full cleaning and extension
56	553325	RL	L2/3	full cleaning and extension
57	554200	AL	L2/3	full cleaning and extension
58	554741	RL	L2/3	full cleaning and extension
59	554833	RL	L4	full cleaning and extension
60	554921	RL	L2/3	full cleaning and extension
61	556823	RL	L4	full cleaning and extension
62	557030	RL	L4	full cleaning and extension
63	557121	RL	L4	full cleaning and extension
64	558684	RL	L5	full cleaning and extension
65	558709	RL	L4	full cleaning and extension
66	559081	RL	L5	full cleaning and extension

Continued on next page

Supplemental Table 1. Proofread presynaptic neuron nucleus ID's, area, layer, and proofreading strategy

index	nucleus_id	area	layer	proofreading strategy
67	559381	RL	L5	full cleaning and extension
68	560109	RL	L5	full cleaning and extension
69	560217	RL	L5	full cleaning and extension
70	560530	RL	L5	full cleaning and extension
71	560732	RL	L5	full cleaning and extension
72	562808	RL	L5	full cleaning and extension
73	581967	AL	L2/3	full cleaning and extension
74	582056	AL	L2/3	full cleaning and extension
75	582129	AL	L2/3	full cleaning and extension
76	582210	AL	L2/3	full cleaning and extension
77	583848	AL	L2/3	full cleaning and extension
78	583961	RL	L2/3	full cleaning and extension
79	585723	RL	L4	full cleaning and extension
80	587426	AL	L4	full cleaning and extension
81	588839	RL	L5	full cleaning and extension
82	588983	AL	L5	full cleaning and extension
83	610498	AL	L2/3	full cleaning and extension
84	616159	AL	L5	full cleaning and extension
85	516621	RL	L2/3	full cleaning and partial axonal extension
86	516988	RL	L2/3	full cleaning and partial axonal extension
87	517993	RL	L2/3	full cleaning and partial axonal extension
88	518004	RL	L2/3	full cleaning and partial axonal extension
89	518134	RL	L2/3	full cleaning and partial axonal extension
90	518224	RL	L2/3	full cleaning and partial axonal extension
91	518312	RL	L2/3	full cleaning and partial axonal extension
92	518623	RL	L2/3	full cleaning and partial axonal extension
93	518632	RL	L2/3	full cleaning and partial axonal extension
94	519746	RL	L2/3	full cleaning and partial axonal extension
95	520027	RL	L4	full cleaning and partial axonal extension
96	520182	RL	L2/3	full cleaning and partial axonal extension
97	551802	RL	L2/3	full cleaning and partial axonal extension
98	553216	RL	L2/3	full cleaning and partial axonal extension
99	553283	RL	L2/3	full cleaning and partial axonal extension
100	553321	RL	L2/3	full cleaning and partial axonal extension
101	553339	RL	L2/3	full cleaning and partial axonal extension
102	553360	RL	L2/3	full cleaning and partial axonal extension
103	553469	RL	L2/3	full cleaning and partial axonal extension
104	553556	RL	L2/3	full cleaning and partial axonal extension
105	553585	RL	L2/3	full cleaning and partial axonal extension
106	553589	RL	L2/3	full cleaning and partial axonal extension
107	554734	RL	L2/3	full cleaning and partial axonal extension
108	554775	RL	L2/3	full cleaning and partial axonal extension
109	554891	RL	L2/3	full cleaning and partial axonal extension
110	554900	RL	L2/3	full cleaning and partial axonal extension
111	555010	RL	L2/3	full cleaning and partial axonal extension
112	580774	AL	L2/3	full cleaning and partial axonal extension
113	580826	AL	L2/3	full cleaning and partial axonal extension
114	580905	AL	L2/3	full cleaning and partial axonal extension
115	580948	RL	L2/3	full cleaning and partial axonal extension
116	580988	AL	L2/3	full cleaning and partial axonal extension
117	581988	AL	L2/3	full cleaning and partial axonal extension
118	581998	AL	L2/3	full cleaning and partial axonal extension
119	582011	AL	L2/3	full cleaning and partial axonal extension
120	582091	AL	L2/3	full cleaning and partial axonal extension
121	582294	AL	L2/3	full cleaning and partial axonal extension
122	582313	RL	L2/3	full cleaning and partial axonal extension
123	582353	AL	L2/3	full cleaning and partial axonal extension
124	582388	RL	L2/3	full cleaning and partial axonal extension
125	582390	RL	L2/3	full cleaning and partial axonal extension
126	582409	RL	L2/3	full cleaning and partial axonal extension
127	582412	RL	L2/3	full cleaning and partial axonal extension
128	582414	RL	L2/3	full cleaning and partial axonal extension
129	582444	RL	L2/3	full cleaning and partial axonal extension
130	582468	RL	L2/3	full cleaning and partial axonal extension
131	582471	RL	L2/3	full cleaning and partial axonal extension
132	583659	AL	L2/3	full cleaning and partial axonal extension
133	583739	AL	L2/3	full cleaning and partial axonal extension
134	583741	AL	L2/3	full cleaning and partial axonal extension

Continued on next page

Supplemental Table 1. Proofread presynaptic neuron nucleus ID's, area, layer, and proofreading strategy

index	nucleus_id	area	layer	proofreading strategy
135	583792	AL	L2/3	full cleaning and partial axonal extension
136	583891	RL	L2/3	full cleaning and partial axonal extension
137	584004	RL	L2/3	full cleaning and partial axonal extension
138	608166	AL	L2/3	full cleaning and partial axonal extension
139	608213	AL	L2/3	full cleaning and partial axonal extension
140	610396	AL	L2/3	full cleaning and partial axonal extension
141	610403	AL	L2/3	full cleaning and partial axonal extension
142	610434	AL	L2/3	full cleaning and partial axonal extension
143	610535	AL	L2/3	full cleaning and partial axonal extension
144	610607	AL	L2/3	full cleaning and partial axonal extension
145	610615	AL	L2/3	full cleaning and partial axonal extension
146	612143	AL	L2/3	full cleaning and partial axonal extension
147	612266	AL	L2/3	full cleaning and partial axonal extension
148	612352	AL	L2/3	full cleaning and partial axonal extension

Supplemental Table 2. Pairwise comparison of the presynaptic mean in silico signal correlation between different neuron pair populations. For each comparison, a pairwise t-test was performed to test the null hypothesis that for each presynaptic neuron, the mean in silico signal correlation is the same between two postsynaptic populations. adjusted p-value is the adjusted p-value through the BH multicomparison correction procedure.

Comparison	Projection type	Mean pairwise difference	p-value	adjusted p-value	t statistic	n
ADP vs Same region	HVA->HVA	0.015	5.30e-05	7.96e-05	4.405	53
ADP vs Same region	HVA->V1	0.007	1.14e-02	1.14e-02	2.661	39
ADP vs Same region	V1->HVA	0.011	3.12e-03	3.41e-03	3.475	17
ADP vs Same region	V1->V1	0.009	3.18e-05	5.45e-05	4.793	35
Connected vs ADP	HVA->HVA	0.026	3.58e-08	2.15e-07	6.460	53
Connected vs ADP	HVA->V1	0.029	7.85e-06	1.57e-05	5.168	39
Connected vs ADP	V1->HVA	0.023	1.25e-03	1.50e-03	3.908	17
Connected vs ADP	V1->V1	0.030	7.33e-06	1.57e-05	5.285	35
Connected vs Same region	HVA->HVA	0.042	3.37e-10	4.04e-09	7.733	53
Connected vs Same region	HVA->V1	0.036	5.77e-06	1.57e-05	5.266	39
Connected vs Same region	V1->HVA	0.034	9.21e-05	1.23e-04	5.175	17
Connected vs Same region	V1->V1	0.039	4.05e-07	1.62e-06	6.253	35

Supplemental Table 3. Number of neurons and neuron pairs invovled in the visualization of the correlation between in silico signal correlation and L_d / neuron pair (synapses excluded) in different projection types across brain areas.

Projection type	Δ in silico signal correlation bin	# of presynaptic neurons	# of postsynaptic neurons	# of ADP control neurons	# of same region control neurons	# of pre-post pairs	# of pre-ADP pairs	# of pre-'same region' pairs	# of synapses	totalL_d (mm)
$V1 \rightarrow V1$	-0.30 - -0.20	27	0	427	27	0	570	1518	0	14.618620
$V1 \rightarrow V1$	-0.20 - -0.10	36	0	3624	36	0	8358	22716	0	235.352922
$V1 \rightarrow V1$	-0.10 - -0.00	36	0	5939	36	0	31843	82271	0	943.324036
$V1 \rightarrow V1$	-0.00 - 0.10	36	0	5575	36	0	22037	53619	0	704.008419
$V1 \rightarrow V1$	0.10 - 0.20	36	0	3884	36	0	8136	18497	0	268.080820
$V1 \rightarrow V1$	0.20 - 0.30	36	0	1938	36	0	2662	5310	0	86.811831
$V1 \rightarrow V1$	0.30 - 0.40	36	0	754	36	0	862	1373	0	29.303881
$V1 \rightarrow V1$	0.40 - 0.50	34	0	245	27	0	256	350	0	8.436686
$HVA \rightarrow HVA$	-0.30 - -0.20	100	0	737	98	0	2642	9566	0	76.177507
$HVA \rightarrow HVA$	-0.20 - -0.10	102	0	2207	102	0	13596	36699	0	417.557033
$HVA \rightarrow HVA$	-0.10 - -0.00	102	0	2593	102	0	29335	70079	0	994.561220
$HVA \rightarrow HVA$	-0.00 - 0.10	102	0	2549	102	0	24611	58614	0	853.487712
$HVA \rightarrow HVA$	0.10 - 0.20	102	0	2264	102	0	13152	29881	0	484.795597
$HVA \rightarrow HVA$	0.20 - 0.30	102	0	1677	102	0	5266	10534	0	203.187307
$HVA \rightarrow HVA$	0.30 - 0.40	102	0	828	102	0	1469	2700	0	57.001171
$V1 \rightarrow HVA$	-0.20 - -0.10	29	0	958	29	0	1430	7995	0	30.452029
$V1 \rightarrow HVA$	-0.10 - -0.00	29	0	2203	29	0	5725	32680	0	141.454788
$V1 \rightarrow HVA$	-0.00 - 0.10	29	0	2027	29	0	4825	23561	0	123.475999
$V1 \rightarrow HVA$	0.10 - 0.20	29	0	1038	29	0	1541	7314	0	38.443692
$V1 \rightarrow HVA$	0.20 - 0.30	29	0	348	29	0	398	1794	0	9.596663
$HVA \rightarrow V1$	-0.30 - -0.20	87	0	450	87	0	731	8861	0	13.161841
$HVA \rightarrow V1$	-0.20 - -0.10	92	0	2834	92	0	6850	88153	0	123.501498
$HVA \rightarrow V1$	-0.10 - -0.00	92	0	5315	92	0	17932	245585	0	345.186645
$HVA \rightarrow V1$	-0.00 - 0.10	92	0	4582	92	0	13701	180600	0	279.289998
$HVA \rightarrow V1$	0.10 - 0.20	92	0	2753	92	0	5823	70851	0	119.710286
$HVA \rightarrow V1$	0.20 - 0.30	92	0	1345	92	0	2135	21317	0	44.995031
$HVA \rightarrow V1$	0.30 - 0.40	92	0	479	92	0	616	5487	0	13.275195

Supplemental Table 4. Number of neurons and neuron pairs invovled in the visualization of the correlation between in silico signal correlation and $N_{syn}/mm\ L_d$ in different projection types across brain areas.

Projection type	Δ in silico signal correlation bin	# of presynaptic neurons	# of postsynaptic neurons	# of ADP control neurons	# of same region control neurons	# of pre-post pairs	# of pre-ADP pairs	# of pre-'same region' pairs	# of synapses	totalL_d (mm)
$V1 \rightarrow V1$	-0.30 - -0.20	25	14	519	0	14	723	0	15	18.799029
$V1 \rightarrow V1$	-0.20 - -0.10	36	205	3928	0	214	9922	0	232	283.947056
$V1 \rightarrow V1$	-0.10 - -0.00	36	736	5943	0	850	33384	0	945	1018.234754
$V1 \rightarrow V1$	-0.00 - 0.10	36	664	5534	0	767	21646	0	881	721.429779
$V1 \rightarrow V1$	0.10 - 0.20	36	305	3713	0	337	7791	0	392	267.558394
$V1 \rightarrow V1$	0.20 - 0.30	36	135	1817	0	145	2574	0	182	86.912818
$V1 \rightarrow V1$	0.30 - 0.40	36	46	693	0	47	823	0	54	29.728849
$V1 \rightarrow V1$	0.40 - 0.50	29	27	220	0	27	256	0	32	8.926083
$HVA \rightarrow HVA$	-0.30 - -0.20	92	49	830	0	52	3241	0	59	94.472855
$HVA \rightarrow HVA$	-0.20 - -0.10	99	285	2252	0	328	14928	0	359	481.976078
$HVA \rightarrow HVA$	-0.10 - -0.00	99	624	2596	0	778	30495	0	836	1077.808884
$HVA \rightarrow HVA$	-0.00 - 0.10	99	584	2538	0	755	24558	0	841	893.638912
$HVA \rightarrow HVA$	0.10 - 0.20	99	324	2231	0	392	12399	0	440	472.381883
$HVA \rightarrow HVA$	0.20 - 0.30	99	160	1590	0	169	4537	0	194	180.483568
$HVA \rightarrow HVA$	0.30 - 0.40	95	52	714	0	54	1168	0	59	49.267130
$V1 \rightarrow HVA$	-0.20 - -0.10	28	38	1053	0	38	1684	0	39	37.691653
$V1 \rightarrow HVA$	-0.10 - -0.00	29	187	2231	0	200	6180	0	226	156.738585
$V1 \rightarrow HVA$	-0.00 - 0.10	29	159	1975	0	169	4723	0	194	126.623281
$V1 \rightarrow HVA$	0.10 - 0.20	28	76	938	0	80	1468	0	94	38.089134
$V1 \rightarrow HVA$	0.20 - 0.30	26	24	301	0	24	368	0	26	9.252531
$HVA \rightarrow V1$	-0.30 - -0.20	69	13	531	0	13	879	0	13	15.455242
$HVA \rightarrow V1$	-0.20 - -0.10	90	133	3029	0	138	7559	0	150	142.347339
$HVA \rightarrow V1$	-0.10 - -0.00	90	364	5363	0	385	18588	0	425	370.298550
$HVA \rightarrow V1$	-0.00 - 0.10	90	327	4534	0	349	13530	0	370	281.465665
$HVA \rightarrow V1$	0.10 - 0.20	90	142	2648	0	146	5607	0	168	118.052918
$HVA \rightarrow V1$	0.20 - 0.30	90	67	1257	0	70	2008	0	77	43.367913
$HVA \rightarrow V1$	0.30 - 0.40	76	25	423	0	27	559	0	38	12.949679

Supplemental Table 5. Estimated marginal means of linear trends for the effect of in silico signal correlation on L_d / neuron pair (synapses excluded) in different projection types across brain areas. z and p-value are the z statistics and p-value of the marginal mean linear trends estimated from the fitted GLMMs. adjusted p-value is the adjusted p value through the BH multicomparison correction procedure.

Projection type	Coefficient	adjusted p-value	p-value	# of presynaptic neurons	# of postsynaptic neurons	# of ADP control neurons	# of same region control neurons	# of synapses	# of pre-post pairs	# of pre-ADP pairs	# of pre-'same region' pairs
$V1 \rightarrow V1$	1.125	5.18e-160	2.59e-160	36	0	6237	36	0	0	74829	185807
$HVA \rightarrow HVA$	1.109	4.24e-278	1.06e-278	99	0	2635	99	0	0	89611	212583
$V1 \rightarrow HVA$	1.101	5.36e-25	5.36e-25	29	0	2525	29	0	0	14126	74633
$HVA \rightarrow V1$	0.872	1.48e-82	1.11e-82	90	0	6148	90	0	0	47811	608388

Supplemental Table 6. Estimated marginal means of linear trends for the effect of in silico signal correlation on $N_{syn}/mm\ L_d$ in different projection types across brain areas. z and p-value are the z statistics and p-value of the marginal mean linear trends estimated from the fitted GLMMs. adjusted p-value is the adjusted p value through the BH multicomparison correction procedure.

Projection type	Coefficient	adjusted p-value	p-value	# of presynaptic neurons	# of postsynaptic neurons	# of ADP control neurons	# of same region control neurons	# of synapses	# of pre-post pairs	# of pre-ADP pairs	# of pre-'same region' pairs
$V1 \rightarrow V1$	2.297	9.17e-50	2.29e-50	36	1719	6237	0	2744	2411	77240	0
$HVA \rightarrow HVA$	1.043	3.84e-12	2.88e-12	99	1396	2635	0	2803	2543	92154	0
$V1 \rightarrow HVA$	1.985	8.57e-07	8.57e-07	29	448	2525	0	584	515	14641	0
$HVA \rightarrow V1$	1.603	2.59e-12	1.29e-12	90	974	6148	0	1255	1139	48950	0

Supplemental Table 7. Number of neurons and neuron pairs invovled in the visualization of the correlation between in vivo signal correlation and L_d / neuron pair (synapses excluded) in different projection types across brain areas.

Projection type	Δ in vivo signal correlation bin	# of presynaptic neurons	# of postsynaptic neurons	# of ADP control neurons	# of same region control neurons	# of pre-post pairs	# of pre-ADP pairs	# of pre-'same region' pairs	# of synapses	totalL_d (mm)
$V1 \rightarrow V1$	-0.30 - -0.20	36	0	1552	36	0	2656	9132	0	69.390757
$V1 \rightarrow V1$	-0.20 - -0.10	36	0	5565	36	0	19022	54877	0	543.353655
$V1 \rightarrow V1$	-0.10 - -0.00	36	0	6114	36	0	23976	60410	0	728.386124
$V1 \rightarrow V1$	-0.00 - 0.10	36	0	5449	36	0	15642	37077	0	501.565276
$V1 \rightarrow V1$	0.10 - 0.20	36	0	4178	36	0	9062	20187	0	296.744655
$V1 \rightarrow V1$	0.20 - 0.30	36	0	2902	36	0	4947	10613	0	158.206795
$V1 \rightarrow V1$	0.30 - 0.40	36	0	1800	36	0	2584	5761	0	82.535045
$V1 \rightarrow V1$	0.40 - 0.50	36	0	1091	36	0	1399	3143	0	45.476341
$V1 \rightarrow V1$	0.50 - 0.60	35	0	625	35	0	768	1571	0	24.006232
$V1 \rightarrow V1$	0.60 - 0.70	31	0	317	29	0	384	747	0	12.507211
$HVA \rightarrow HVA$	-0.40 - -0.30	65	0	225	64	0	446	1904	0	11.872237
$HVA \rightarrow HVA$	-0.30 - -0.20	104	0	1212	104	0	4695	15354	0	141.825146
$HVA \rightarrow HVA$	-0.20 - -0.10	106	0	2805	106	0	20166	54570	0	653.240105
$HVA \rightarrow HVA$	-0.10 - -0.00	106	0	2972	106	0	32117	79749	0	1072.653987
$HVA \rightarrow HVA$	-0.00 - 0.10	106	0	2910	106	0	22291	56261	0	763.312753
$HVA \rightarrow HVA$	0.10 - 0.20	106	0	2621	106	0	12457	31246	0	436.743130
$HVA \rightarrow HVA$	0.20 - 0.30	106	0	2107	106	0	6603	15249	0	235.733457
$HVA \rightarrow HVA$	0.30 - 0.40	106	0	1408	106	0	3156	6797	0	120.009172
$HVA \rightarrow HVA$	0.40 - 0.50	106	0	842	106	0	1479	2788	0	57.110029
$HVA \rightarrow HVA$	0.50 - 0.60	99	0	417	95	0	575	977	0	24.809982
$V1 \rightarrow HVA$	-0.30 - -0.20	29	0	381	29	0	472	3237	0	11.502273
$V1 \rightarrow HVA$	-0.20 - -0.10	29	0	1740	29	0	3188	17931	0	77.885536
$V1 \rightarrow HVA$	-0.10 - -0.00	29	0	2299	29	0	5273	29111	0	131.740088
$V1 \rightarrow HVA$	-0.00 - 0.10	29	0	1896	29	0	3584	17887	0	87.290731
$V1 \rightarrow HVA$	0.10 - 0.20	29	0	1232	29	0	1850	8793	0	46.915050
$V1 \rightarrow HVA$	0.20 - 0.30	29	0	706	29	0	915	4306	0	23.142961
$V1 \rightarrow HVA$	0.30 - 0.40	29	0	376	29	0	432	2088	0	9.855496
$V1 \rightarrow HVA$	0.40 - 0.50	29	0	212	29	0	253	1004	0	6.288603
$HVA \rightarrow V1$	-0.30 - -0.20	92	0	1188	92	0	1960	24054	0	34.934123
$HVA \rightarrow V1$	-0.20 - -0.10	94	0	4640	94	0	12391	153177	0	234.769489
$HVA \rightarrow V1$	-0.10 - -0.00	94	0	5673	94	0	17333	227262	0	341.230850
$HVA \rightarrow V1$	-0.00 - 0.10	94	0	4812	94	0	11544	145012	0	230.704006
$HVA \rightarrow V1$	0.10 - 0.20	94	0	3291	94	0	6244	75588	0	127.891275
$HVA \rightarrow V1$	0.20 - 0.30	94	0	1974	94	0	3115	37057	0	64.396003
$HVA \rightarrow V1$	0.30 - 0.40	94	0	1167	94	0	1611	17422	0	31.785912
$HVA \rightarrow V1$	0.40 - 0.50	94	0	578	94	0	699	7804	0	14.966269

Supplemental Table 8. Number of neurons and neuron pairs invovled in the visualization of the correlation between in vivo signal correlation and $N_{syn}/mm\ L_d$ in different projection types across brain areas.

Projection type	Δ in vivo signal correlation bin	# of presynaptic neurons	# of postsynaptic neurons	# of ADP control neurons	# of same region control neurons	# of pre-post pairs	# of pre-ADP pairs	# of pre-'same region' pairs	# of synapses	totalL_d (mm)
$V1 \rightarrow V1$	-0.30 - -0.20	34	101	2202	0	104	4393	0	116	120.196380
$V1 \rightarrow V1$	-0.20 - -0.10	36	483	5747	0	520	20983	0	569	614.701246
$V1 \rightarrow V1$	-0.10 - -0.00	36	588	6111	0	657	23822	0	734	749.965351
$V1 \rightarrow V1$	-0.00 - 0.10	36	477	5353	0	525	15389	0	582	510.116138
$V1 \rightarrow V1$	0.10 - 0.20	36	299	4038	0	327	8806	0	382	301.521896
$V1 \rightarrow V1$	0.20 - 0.30	36	205	2774	0	223	4735	0	263	160.163966
$V1 \rightarrow V1$	0.30 - 0.40	36	111	1665	0	112	2461	0	135	82.914655
$V1 \rightarrow V1$	0.40 - 0.50	36	64	1006	0	66	1325	0	79	43.172834
$V1 \rightarrow V1$	0.50 - 0.60	35	29	571	0	32	723	0	42	24.178848
$V1 \rightarrow V1$	0.60 - 0.70	30	21	286	0	22	367	0	33	12.753262
$HVA \rightarrow HVA$	-0.40 - -0.30	50	13	332	0	13	742	0	15	20.548477
$HVA \rightarrow HVA$	-0.30 - -0.20	99	87	1393	0	93	5788	0	103	180.512305
$HVA \rightarrow HVA$	-0.20 - -0.10	105	406	2837	0	471	21472	0	509	716.812856
$HVA \rightarrow HVA$	-0.10 - -0.00	105	688	2969	0	872	32905	0	947	1142.705436
$HVA \rightarrow HVA$	-0.00 - 0.10	105	552	2911	0	661	22349	0	715	794.109314
$HVA \rightarrow HVA$	0.10 - 0.20	105	304	2599	0	344	12079	0	391	435.790667
$HVA \rightarrow HVA$	0.20 - 0.30	105	173	2058	0	188	6251	0	218	234.891093
$HVA \rightarrow HVA$	0.30 - 0.40	105	104	1345	0	109	2938	0	126	117.834260
$HVA \rightarrow HVA$	0.40 - 0.50	101	46	781	0	48	1315	0	51	51.536756
$HVA \rightarrow HVA$	0.50 - 0.60	83	20	376	0	20	519	0	24	23.481751
$V1 \rightarrow HVA$	-0.30 - -0.20	24	18	450	0	18	593	0	21	14.369431
$V1 \rightarrow HVA$	-0.20 - -0.10	29	117	1875	0	123	3741	0	140	95.546797
$V1 \rightarrow HVA$	-0.10 - -0.00	29	168	2317	0	175	5532	0	196	141.870319
$V1 \rightarrow HVA$	-0.00 - 0.10	29	121	1822	0	125	3417	0	140	86.935079
$V1 \rightarrow HVA$	0.10 - 0.20	29	69	1139	0	71	1715	0	78	44.698868
$V1 \rightarrow HVA$	0.20 - 0.30	26	44	661	0	44	889	0	50	23.830929
$V1 \rightarrow HVA$	0.30 - 0.40	27	25	358	0	26	449	0	31	10.845062
$V1 \rightarrow HVA$	0.40 - 0.50	25	11	195	0	11	237	0	13	6.017091
$HVA \rightarrow V1$	-0.30 - -0.20	85	46	1263	0	46	2180	0	50	40.028150
$HVA \rightarrow V1$	-0.20 - -0.10	93	211	4711	0	220	12816	0	242	248.419138
$HVA \rightarrow V1$	-0.10 - -0.00	93	375	5690	0	400	17857	0	434	361.524099
$HVA \rightarrow V1$	-0.00 - 0.10	93	291	4804	0	305	11709	0	333	241.200378
$HVA \rightarrow V1$	0.10 - 0.20	93	159	3250	0	164	6214	0	181	129.824307
$HVA \rightarrow V1$	0.20 - 0.30	93	96	1933	0	98	3084	0	116	65.574084
$HVA \rightarrow V1$	0.30 - 0.40	91	44	1119	0	45	1531	0	49	31.773139
$HVA \rightarrow V1$	0.40 - 0.50	82	30	549	0	30	689	0	33	15.452123

Supplemental Table 9. Estimated marginal means of linear trends for the effect of in vivo signal correlation on L_d / neuron pair (synapses excluded) in different projection types across brain areas. z and p-value are the z statistics and p-value of the marginal mean linear trends estimated from the fitted GLMMs. adjusted p-value is the adjusted p value through the BH multicomparison correction procedure.

Projection type	Coefficient	adjusted p-value	p-value	# of presynaptic neurons	# of postsynaptic neurons	# of ADP control neurons	# of same region control neurons	# of synapses	# of pre-post pairs	# of pre-ADP pairs	# of pre-'same region' pairs
$V1 \rightarrow V1$	0.779	1.96e-210	4.89e-211	36	0	6807	36	0	0	80703	204150
$HVA \rightarrow HVA$	0.698	3.51e-198	1.75e-198	105	0	3010	105	0	0	103839	262309
$V1 \rightarrow HVA$	0.624	1.60e-23	1.60e-23	29	0	2887	29	0	0	16164	85137
$HVA \rightarrow V1$	0.428	5.69e-43	4.27e-43	93	0	6720	93	0	0	55313	685610

Supplemental Table 10. Estimated marginal means of linear trends for the effect of in vivo signal correlation on N_{syn}/mm L_d in different projection types across brain areas. z and p-value are the z statistics and p-value of the marginal mean linear trends estimated from the fitted GLMMs. adjusted p-value is the adjusted p value through the BH multicomparison correction procedure.

Projection type	Coefficient	adjusted p-value	p-value	# of presynaptic neurons	# of postsynaptic neurons	# of ADP control neurons	# of same region control neurons	# of synapses	# of pre-post pairs	# of pre-ADP pairs	# of pre-'same region' pairs
$V1 \rightarrow V1$	1.126	3.66e-30	9.16e-31	36	1865	6807	0	2947	2600	83303	0
$HVA \rightarrow HVA$	0.667	1.96e-09	9.79e-10	105	1566	3010	0	3114	2832	106671	0
$V1 \rightarrow HVA$	0.857	1.63e-04	1.63e-04	29	522	2887	0	679	602	16766	0
$HVA \rightarrow V1$	0.861	9.53e-08	7.15e-08	93	1116	6720	0	1445	1315	56628	0

Supplemental Table 11. Number of neurons and neuron pairs invovled in the visualization of the correlation between feature weight similarity and L_d / neuron pair (synapses excluded) in different projection types across brain areas.

Projection type	Δ feature weight similarity bin	# of presynaptic neurons	# of postsynaptic neurons	# of ADP control neurons	# of same region control neurons	# of pre-post pairs	# of pre-ADP pairs	# of pre-'same region' pairs	# of synapses	totalL_d (mm)
$V1 \rightarrow V1$	-0.30 - -0.20	36	0	1072	36	0	1295	3229	0	36.335238
$V1 \rightarrow V1$	-0.20 - -0.10	36	0	4396	36	0	9834	25779	0	285.168739
$V1 \rightarrow V1$	-0.10 - 0.00	36	0	5808	36	0	25602	67324	0	768.876584
$V1 \rightarrow V1$	0.00 - 0.10	36	0	5735	36	0	25230	62013	0	783.990533
$V1 \rightarrow V1$	0.10 - 0.20	36	0	4410	36	0	10333	22756	0	335.696665
$V1 \rightarrow V1$	0.20 - 0.30	36	0	1629	36	0	2112	4129	0	69.293019
$V1 \rightarrow V1$	0.30 - 0.40	36	0	301	35	0	318	436	0	10.072933
$HVA \rightarrow HVA$	-0.30 - -0.20	102	0	815	102	0	1392	4489	0	41.334690
$HVA \rightarrow HVA$	-0.20 - -0.10	102	0	2359	102	0	10985	31232	0	335.521478
$HVA \rightarrow HVA$	-0.10 - 0.00	102	0	2619	102	0	30066	78862	0	988.398935
$HVA \rightarrow HVA$	0.00 - 0.10	102	0	2600	102	0	31946	74147	0	1124.617864
$HVA \rightarrow HVA$	0.10 - 0.20	102	0	2358	102	0	13356	27119	0	493.620990
$HVA \rightarrow HVA$	0.20 - 0.30	102	0	1339	102	0	2686	4189	0	109.398149
$HVA \rightarrow HVA$	0.30 - 0.40	90	0	250	76	0	289	358	0	14.959203
$V1 \rightarrow HVA$	-0.20 - -0.10	29	0	1136	29	0	1620	8739	0	40.188636
$V1 \rightarrow HVA$	-0.10 - 0.00	29	0	2146	29	0	5204	28801	0	128.424763
$V1 \rightarrow HVA$	0.00 - 0.10	29	0	2122	29	0	5175	26929	0	126.070146
$V1 \rightarrow HVA$	0.10 - 0.20	29	0	1134	29	0	1729	8279	0	43.275205
$V1 \rightarrow HVA$	0.20 - 0.30	29	0	224	29	0	248	1072	0	6.141092
$HVA \rightarrow V1$	-0.20 - -0.10	92	0	3143	92	0	5593	78638	0	104.073655
$HVA \rightarrow V1$	-0.10 - 0.00	92	0	5364	92	0	17167	231272	0	327.750993
$HVA \rightarrow V1$	0.00 - 0.10	92	0	5214	92	0	17054	220016	0	341.745469
$HVA \rightarrow V1$	0.10 - 0.20	92	0	3111	92	0	6369	73731	0	132.250047
$HVA \rightarrow V1$	0.20 - 0.30	92	0	846	92	0	1111	10568	0	24.540542

Supplemental Table 12. Number of neurons and neuron pairs invovled in the visualization of the correlation between feature weight similarity and N_{syn}/mm L_d in different projection types across brain areas.

Projection type	Δ feature weight similarity bin	# of presynaptic neurons	# of postsynaptic neurons	# of ADP control neurons	# of same region control neurons	# of pre-post pairs	# of pre-ADP pairs	# of pre-'same region' pairs	# of synapses	totalL_d (mm)
$V1 \rightarrow V1$	-0.30 - -0.20	36	36	1182	0	36	1509	0	38	43.620452
$V1 \rightarrow V1$	-0.20 - -0.10	36	230	4537	0	237	10895	0	258	322.934569
$V1 \rightarrow V1$	-0.10 - 0.00	36	630	5812	0	708	27056	0	794	833.029064
$V1 \rightarrow V1$	0.00 - 0.10	36	729	5720	0	852	25425	0	969	819.256558
$V1 \rightarrow V1$	0.10 - 0.20	36	388	4292	0	438	9940	0	509	337.394190
$V1 \rightarrow V1$	0.20 - 0.30	36	102	1496	0	112	2007	0	139	69.123548
$V1 \rightarrow V1$	0.30 - 0.40	33	24	259	0	24	294	0	31	10.411849
$HVA \rightarrow HVA$	-0.30 - -0.20	99	33	968	0	35	1852	0	37	55.775849
$HVA \rightarrow HVA$	-0.20 - -0.10	99	254	2421	0	276	12617	0	301	398.118425
$HVA \rightarrow HVA$	-0.10 - 0.00	99	663	2619	0	807	32094	0	876	1097.132235
$HVA \rightarrow HVA$	0.00 - 0.10	99	649	2594	0	847	31140	0	926	1149.553761
$HVA \rightarrow HVA$	0.10 - 0.20	99	386	2318	0	450	11911	0	514	461.647156
$HVA \rightarrow HVA$	0.20 - 0.30	98	104	1189	0	109	2216	0	128	98.577172
$HVA \rightarrow HVA$	0.30 - 0.40	71	15	183	0	15	213	0	16	11.813672
$V1 \rightarrow HVA$	-0.20 - -0.10	28	45	1187	0	47	1799	0	50	45.872386
$V1 \rightarrow HVA$	-0.10 - 0.00	29	174	2162	0	179	5474	0	196	139.731979
$V1 \rightarrow HVA$	0.00 - 0.10	29	196	2103	0	204	5296	0	242	132.939401
$V1 \rightarrow HVA$	0.10 - 0.20	29	67	1102	0	70	1684	0	80	44.564126
$V1 \rightarrow HVA$	0.20 - 0.30	27	13	196	0	13	227	0	14	5.948031
$HVA \rightarrow V1$	-0.20 - -0.10	90	106	3354	0	109	6261	0	121	120.205383
$HVA \rightarrow V1$	-0.10 - 0.00	90	370	5397	0	389	18035	0	429	355.383651
$HVA \rightarrow V1$	0.00 - 0.10	90	365	5192	0	396	16927	0	425	348.693858
$HVA \rightarrow V1$	0.10 - 0.20	90	187	2962	0	195	5992	0	218	128.408223
$HVA \rightarrow V1$	0.20 - 0.30	84	34	709	0	36	941	0	45	20.898991

Supplemental Table 13. Estimated marginal means of linear trends for the effect of feature weight similarity on L_d / neuron pair (synapses excluded) in different projection types across brain areas. z and p-value are the z statistics and p-value of the marginal mean linear trends estimated from the fitted GLMMs. adjusted p-value is the adjusted p value through the BH multicomparison correction procedure.

Projection type	Coefficient	adjusted p-value	p-value	# of presynaptic neurons	# of postsynaptic neurons	# of ADP control neurons	# of same region control neurons	# of synapses	# of pre-post pairs	# of pre-ADP pairs	# of pre-'same region' pairs
$V1 \rightarrow V1$	0.947	3.48e-107	1.74e-107	36	0	6237	36	0	0	74829	185807
$HVA \rightarrow HVA$	1.702	0.00e+00	0.00e+00	99	0	2635	99	0	0	89611	212583
$V1 \rightarrow HVA$	0.701	5.01e-10	5.01e-10	29	0	2525	29	0	0	14126	74633
$HVA \rightarrow V1$	1.109	3.18e-94	2.39e-94	90	0	6148	90	0	0	47811	608388

Supplemental Table 14. Estimated marginal means of linear trends for the effect of feature weight similarity on N_{syn}/mm L_d in different projection types across brain areas. z and p-value are the z statistics and p-value of the marginal mean linear trends estimated from the fitted GLMMs. adjusted p-value is the adjusted p value through the BH multicomparison correction procedure.

Projection type	Coefficient	adjusted p-value	p-value	# of presynaptic neurons	# of postsynaptic neurons	# of ADP control neurons	# of same region control neurons	# of synapses	# of pre-post pairs	# of pre-ADP pairs	# of pre-'same region' pairs
$V1 \rightarrow V1$	2.216	2.45e-35	6.12e-36	36	1719	6237	0	2744	2411	77240	0
$HVA \rightarrow HVA$	1.398	1.13e-13	5.64e-14	99	1396	2635	0	2803	2543	92154	0
$V1 \rightarrow HVA$	1.754	9.51e-05	9.51e-05	29	448	2525	0	584	515	14641	0
$HVA \rightarrow V1$	1.948	1.49e-11	1.11e-11	90	974	6148	0	1255	1139	48950	0

Supplemental Table 15. Number of neurons and neuron pairs invovled in the visualization of the correlation between receptive field center distance and L_d / neuron pair (synapses excluded) in different projection types across brain areas.

Projection type	Δ receptive field center distance bin	# of presynaptic neurons	# of postsynaptic neurons	# of ADP control neurons	# of same region control neurons	# of pre-post pairs	# of pre-ADP pairs	# of pre-'same region' pairs	# of synapses	totalL_d (mm)
$V1 \rightarrow V1$	-10.55 - -5.28	36	0	3587	36	0	13098	16616	0	504.444179
$V1 \rightarrow V1$	-5.28 - 0.00	36	0	5491	36	0	36890	71763	0	1189.389824
$V1 \rightarrow V1$	0.00 - 5.28	36	0	5010	36	0	19930	68768	0	498.660138
$V1 \rightarrow V1$	5.28 - 10.55	36	0	1599	36	0	4266	24166	0	86.320064
$V1 \rightarrow V1$	10.55 - 15.83	36	0	211	36	0	538	4188	0	9.094726
$HVA \rightarrow HVA$	-15.83 - -10.55	44	0	513	44	0	1213	1456	0	53.734766
$HVA \rightarrow HVA$	-10.55 - -5.28	102	0	2281	102	0	17614	26718	0	723.876676
$HVA \rightarrow HVA$	-5.28 - 0.00	102	0	2555	102	0	37564	77929	0	1331.043600
$HVA \rightarrow HVA$	0.00 - 5.28	102	0	2449	102	0	25371	76129	0	770.831112
$HVA \rightarrow HVA$	5.28 - 10.55	102	0	1177	102	0	7797	32087	0	202.978877
$HVA \rightarrow HVA$	10.55 - 15.83	102	0	254	102	0	1139	5848	0	25.291692
$V1 \rightarrow HVA$	-10.55 - -5.28	29	0	985	29	0	2253	11576	0	58.076011
$V1 \rightarrow HVA$	-5.28 - 0.00	29	0	1835	29	0	5668	26875	0	146.551732
$V1 \rightarrow HVA$	0.00 - 5.28	29	0	1623	29	0	4369	23177	0	104.541012
$V1 \rightarrow HVA$	5.28 - 10.55	29	0	620	29	0	1562	10214	0	33.327909
$HVA \rightarrow V1$	-10.55 - -5.28	92	0	3503	92	0	5944	68076	0	127.650382
$HVA \rightarrow V1$	-5.28 - 0.00	92	0	5412	92	0	20967	251016	0	422.868388
$HVA \rightarrow V1$	0.00 - 5.28	92	0	4764	92	0	15792	226867	0	297.769153
$HVA \rightarrow V1$	5.28 - 10.55	92	0	1734	92	0	4574	68340	0	82.355277

Supplemental Table 16. Number of neurons and neuron pairs invovled in the visualization of the correlation between receptive field center distance and $N_{syn}/mm\ L_d$ in different projection types across brain areas.

Projection type	Δ receptive field center distance bin	# of presynaptic neurons	# of postsynaptic neurons	# of ADP control neurons	# of same region control neurons	# of pre-post pairs	# of pre-ADP pairs	# of pre-'same region' pairs	# of synapses	totalL_d (mm)
$V1 \rightarrow V1$	-10.55 - -5.28	35	168	2274	0	178	5317	0	194	210.846986
$V1 \rightarrow V1$	-5.28 - 0.00	36	909	5290	0	1202	36735	0	1380	1313.420605
$V1 \rightarrow V1$	0.00 - 5.28	36	695	5647	0	811	27327	0	929	753.483234
$V1 \rightarrow V1$	5.28 - 10.55	36	173	2336	0	186	6783	0	204	142.873189
$V1 \rightarrow V1$	10.55 - 15.83	34	30	406	0	32	1006	0	35	18.160384
$HVA \rightarrow HVA$	-15.83 - -10.55	28	10	243	0	11	416	0	14	17.918761
$HVA \rightarrow HVA$	-10.55 - -5.28	99	321	2096	0	378	11349	0	428	500.622918
$HVA \rightarrow HVA$	-5.28 - 0.00	99	774	2530	0	1107	37168	0	1220	1438.852620
$HVA \rightarrow HVA$	0.00 - 5.28	99	609	2581	0	756	30304	0	827	980.251453
$HVA \rightarrow HVA$	5.28 - 10.55	99	199	1584	0	246	10984	0	267	294.805748
$HVA \rightarrow HVA$	10.55 - 15.83	99	39	384	0	43	1765	0	45	39.990970
$V1 \rightarrow HVA$	-10.55 - -5.28	27	58	819	0	61	1816	0	66	47.293930
$V1 \rightarrow HVA$	-5.28 - 0.00	29	203	1796	0	228	5917	0	263	157.158156
$V1 \rightarrow HVA$	0.00 - 5.28	29	153	1809	0	158	4861	0	181	123.251450
$V1 \rightarrow HVA$	5.28 - 10.55	29	58	754	0	62	1775	0	67	40.294284
$HVA \rightarrow V1$	-10.55 - -5.28	86	92	2385	0	93	3677	0	106	73.522190
$HVA \rightarrow V1$	-5.28 - 0.00	90	494	5289	0	535	21967	0	584	458.510473
$HVA \rightarrow V1$	0.00 - 5.28	90	382	5185	0	416	18503	0	467	368.061118
$HVA \rightarrow V1$	5.28 - 10.55	90	85	1770	0	89	4319	0	91	80.279113

Supplemental Table 17. Estimated marginal means of linear trends for the effect of receptive field center distance on L_d / neuron pair (synapses excluded) in different projection types across brain areas. z and p-value are the z statistics and p-value of the marginal mean linear trends estimated from the fitted GLMMs. adjusted p-value is the adjusted p value through the BH multicomparison correction procedure.

Projection type	Coefficient	adjusted p-value	p-value	# of presynaptic neurons	# of postsynaptic neurons	# of ADP control neurons	# of same region control neurons	# of synapses	# of pre-post pairs	# of pre-ADP pairs	# of pre-'same region' pairs
$V1 \rightarrow V1$	-0.127	0.00e+00	0.00e+00	36	0	6237	36	0	0	74829	185807
$HVA \rightarrow HVA$	-0.080	0.00e+00	0.00e+00	99	0	2635	99	0	0	89611	212583
$V1 \rightarrow HVA$	-0.022	1.01e-27	1.01e-27	29	0	2525	29	0	0	14126	74633
$HVA \rightarrow V1$	-0.027	8.19e-119	6.14e-119	90	0	6148	90	0	0	47811	608388

Supplemental Table 18. Estimated marginal means of linear trends for the effect of receptive field center distance on N_{syn}/mm L_d in different projection types across brain areas. z and p-value are the z statistics and p-value of the marginal mean linear trends estimated from the fitted GLMMs. adjusted p-value is the adjusted p value through the BH multicomparison correction procedure.

Projection type	Coefficient	adjusted p-value	p-value	# of presynaptic neurons	# of postsynaptic neurons	# of ADP control neurons	# of same region control neurons	# of synapses	# of pre-post pairs	# of pre-ADP pairs	# of pre-'same region' pairs
$V1 \rightarrow V1$	0.030	1.89e-09	4.72e-10	36	1719	6237	0	2744	2411	77240	0
$HVA \rightarrow HVA$	0.010	1.54e-02	1.15e-02	99	1396	2635	0	2803	2543	92154	0
$V1 \rightarrow HVA$	-0.002	8.34e-01	8.34e-01	29	448	2525	0	584	515	14641	0
$HVA \rightarrow V1$	-0.018	1.54e-02	9.65e-03	90	974	6148	0	1255	1139	48950	0

Supplemental Table 19. Number of neurons and neuron pairs invovled in the visualization of the correlation between in silico ΔOri and L_d / neuron pair (synapses excluded) in different projection types across brain areas.

Projection type	Δ in silico ΔOri bin	# of presynaptic neurons	# of postsynaptic neurons	# of ADP control neurons	# of same region control neurons	# of pre-post pairs	# of pre-ADP pairs	# of pre-'same region' pairs	# of synapses	totalL_d (mm)
$V1 \rightarrow V1$	-57.16 - -28.58	24	0	2307	24	0	5415	15129	0	171.067847
$V1 \rightarrow V1$	-28.58 - 0.00	24	0	2537	24	0	8817	21968	0	295.986023
$V1 \rightarrow V1$	0.00 - 28.58	24	0	2743	24	0	7084	17610	0	221.974391
$V1 \rightarrow V1$	28.58 - 57.16	24	0	2059	24	0	5518	16021	0	162.495971
$HVA \rightarrow HVA$	-57.16 - -28.58	60	0	1125	60	0	5729	13469	0	194.286636
$HVA \rightarrow HVA$	-28.58 - 0.00	60	0	1175	60	0	6887	15960	0	235.669897
$HVA \rightarrow HVA$	0.00 - 28.58	60	0	1179	60	0	6905	16323	0	231.975979
$HVA \rightarrow HVA$	28.58 - 57.16	60	0	1129	60	0	5634	13479	0	185.273829
$V1 \rightarrow HVA$	-57.16 - -28.58	18	0	502	18	0	1017	4946	0	26.483564
$V1 \rightarrow HVA$	-28.58 - 0.00	18	0	663	18	0	1232	5295	0	35.218815
$V1 \rightarrow HVA$	0.00 - 28.58	18	0	654	18	0	1179	5792	0	31.287205
$V1 \rightarrow HVA$	28.58 - 57.16	18	0	463	18	0	797	5100	0	20.293288
$HVA \rightarrow V1$	-57.16 - -28.58	53	0	1937	53	0	3351	41162	0	66.825000
$HVA \rightarrow V1$	-28.58 - 0.00	53	0	2540	53	0	5802	59529	0	120.864783
$HVA \rightarrow V1$	0.00 - 28.58	53	0	2630	53	0	5786	56326	0	123.706798
$HVA \rightarrow V1$	28.58 - 57.16	53	0	2011	53	0	3495	41530	0	70.913483

Supplemental Table 20. Number of neurons and neuron pairs invovled in the visualization of the correlation between in silico ΔOri and $N_{syn}/mm\ L_d$ in different projection types across brain areas.

Projection type	Δ in silico ΔOri bin	# of presynaptic neurons	# of postsynaptic neurons	# of ADP control neurons	# of same region control neurons	# of pre-post pairs	# of pre-ADP pairs	# of pre-'same region' pairs	# of synapses	totalL_d (mm)
$V1 \rightarrow V1$	-57.16 - -28.58	24	184	2256	0	203	5252	0	254	171.406452
$V1 \rightarrow V1$	-28.58 - 0.00	24	302	2524	0	336	9435	0	394	329.222605
$V1 \rightarrow V1$	0.00 - 28.58	24	217	2816	0	241	7546	0	268	245.866967
$V1 \rightarrow V1$	28.58 - 57.16	24	144	1979	0	157	5538	0	180	166.321087
$HVA \rightarrow HVA$	-57.16 - -28.58	52	134	1113	0	155	5274	0	169	190.852637
$HVA \rightarrow HVA$	-28.58 - 0.00	52	169	1165	0	180	6698	0	193	241.124324
$HVA \rightarrow HVA$	0.00 - 28.58	52	157	1179	0	173	6701	0	181	240.263087
$HVA \rightarrow HVA$	28.58 - 57.16	52	129	1122	0	150	5299	0	165	182.145706
$V1 \rightarrow HVA$	-57.16 - -28.58	16	39	479	0	40	854	0	48	23.297975
$V1 \rightarrow HVA$	-28.58 - 0.00	16	35	655	0	36	1373	0	45	40.063947
$V1 \rightarrow HVA$	0.00 - 28.58	16	50	678	0	51	1216	0	54	34.018144
$V1 \rightarrow HVA$	28.58 - 57.16	16	28	481	0	30	925	0	33	24.334127
$HVA \rightarrow V1$	-57.16 - -28.58	46	73	1831	0	75	3198	0	81	66.090308
$HVA \rightarrow V1$	-28.58 - 0.00	47	138	2502	0	140	5974	0	159	128.419254
$HVA \rightarrow V1$	0.00 - 28.58	47	140	2641	0	149	5964	0	158	129.941363
$HVA \rightarrow V1$	28.58 - 57.16	47	63	1867	0	64	3187	0	69	67.486736

Supplemental Table 21. Estimated marginal means of linear trends for the effect of in silico ΔOri on L_d / neuron pair (synapses excluded) in different projection types across brain areas. z and p-value are the z statistics and p-value of the marginal mean linear trends estimated from the fitted GLMMs. adjusted p-value is the adjusted p value through the BH multicomparison correction procedure.

Projection type	Coefficient	adjusted p-value	p-value	# of presynaptic neurons	# of postsynaptic neurons	# of ADP control neurons	# of same region control neurons	# of synapses	# of pre-post pairs	# of pre-ADP pairs	# of pre-'same region' pairs
$V1 \rightarrow V1$	-0.001	1.22e-05	6.11e-06	24	0	3456	24	0	0	26834	70728
$HVA \rightarrow HVA$	-0.001	4.70e-02	4.70e-02	52	0	1222	52	0	0	23314	49735
$V1 \rightarrow HVA$	-0.004	4.65e-08	1.16e-08	16	0	1123	16	0	0	4211	18313
$HVA \rightarrow V1$	0.001	3.02e-02	2.27e-02	47	0	3392	47	0	0	17907	174465

Supplemental Table 22. Estimated marginal means of linear trends for the effect of in silico ΔOri on N_{syn}/mm L_d in different projection types across brain areas. z and p-value are the z statistics and p-value of the marginal mean linear trends estimated from the fitted GLMMs. adjusted p-value is the adjusted p value through the BH multicomparison correction procedure.

Projection type	Coefficient	adjusted p-value	p-value	# of presynaptic neurons	# of postsynaptic neurons	# of ADP control neurons	# of same region control neurons	# of synapses	# of pre-post pairs	# of pre-ADP pairs	# of pre-'same region' pairs
$V1 \rightarrow V1$	-0.004	1.12e-03	2.79e-04	24	739	3456	0	1096	937	27771	0
$HVA \rightarrow HVA$	0.000	9.36e-01	9.36e-01	52	452	1222	0	708	658	23972	0
$V1 \rightarrow HVA$	-0.004	2.33e-01	1.75e-01	16	147	1123	0	180	157	4368	0
$HVA \rightarrow V1$	-0.002	2.33e-01	1.68e-01	47	392	3392	0	467	428	18335	0

Supplemental Table 23. Estimated marginal means of linear trends for the effect of in vivo signal correlation on L_d / neuron pair (synapses excluded) in different projection types across brain areas and layers. z and p-value are the z statistics and p-value of the marginal mean linear trends estimated from the fitted GLMMs. adjusted p-value is the adjusted p value through the BH multicomparison correction procedure.

Projection type	Coefficient	adjusted p-value	p-value	# of presynaptic neurons	# of postsynaptic neurons	# of ADP control neurons	# of same region control neurons	# of synapses	# of pre-post pairs	# of pre-ADP pairs	# of pre-'same region' pairs
$V1L2/3 \rightarrow V1L2/3$	1.074	2.49e-109	2.08e-110	20	0	2670	20	0	0	20511	44349
$V1L2/3 \rightarrow V1L4$	0.341	1.52e-07	7.59e-08	19	0	2090	19	0	0	13791	32623
$V1L2/3 \rightarrow V1L5$	0.580	6.10e-18	1.27e-18	20	0	1185	20	0	0	11845	14652
$V1L2/3 \rightarrow HVAL2/3$	1.210	1.21e-25	2.02e-26	15	0	1169	15	0	0	4610	18075
$V1L2/3 \rightarrow HVAL4$	0.798	1.26e-07	5.78e-08	14	0	856	14	0	0	3202	10900
$V1L2/3 \rightarrow HVAL5$	1.136	1.84e-11	4.61e-12	13	0	429	13	0	0	2444	4028
$V1L4 \rightarrow V1L2/3$	0.335	5.41e-03	4.51e-03	6	0	1784	6	0	0	3107	16451
$V1L4 \rightarrow V1L4$	0.422	1.22e-04	8.12e-05	6	0	1865	6	0	0	4503	10073
$V1L4 \rightarrow V1L5$	0.435	1.04e-04	6.51e-05	6	0	1138	6	0	0	3365	4636
$V1L5 \rightarrow V1L4$	0.407	1.85e-04	1.31e-04	6	0	1769	6	0	0	3980	10686
$V1L5 \rightarrow V1L5$	0.523	6.94e-09	2.60e-09	6	0	1145	6	0	0	3721	4280
$HVAL2/3 \rightarrow V1L2/3$	0.067	3.37e-01	3.09e-01	36	0	2626	36	0	0	12670	104893
$HVAL2/3 \rightarrow V1L4$	-0.024	8.66e-01	8.30e-01	28	0	1882	28	0	0	5122	63511
$HVAL2/3 \rightarrow V1L5$	0.361	4.28e-08	1.78e-08	59	0	1172	59	0	0	12966	66476
$HVAL2/3 \rightarrow HVAL2/3$	1.089	3.19e-121	1.33e-122	45	0	1264	45	0	0	19194	48691
$HVAL2/3 \rightarrow HVAL4$	0.831	3.91e-42	4.89e-43	38	0	893	38	0	0	13326	24937
$HVAL2/3 \rightarrow HVAL5$	0.280	1.10e-05	6.07e-06	62	0	439	62	0	0	13451	17560
$HVAL4 \rightarrow HVAL2/3$	0.633	5.28e-09	1.76e-09	12	0	1233	12	0	0	5899	12092
$HVAL4 \rightarrow HVAL4$	0.679	1.93e-09	5.62e-10	12	0	893	12	0	0	5266	6729
$HVAL4 \rightarrow HVAL5$	0.355	7.93e-03	6.94e-03	11	0	434	11	0	0	2992	2477
$HVAL5 \rightarrow V1L5$	-0.013	9.11e-01	9.11e-01	14	0	1093	14	0	0	3539	15315
$HVAL5 \rightarrow HVAL2/3$	0.332	1.38e-03	1.04e-03	17	0	1236	17	0	0	7564	18063
$HVAL5 \rightarrow HVAL4$	0.326	4.43e-03	3.51e-03	17	0	896	17	0	0	6110	11017
$HVAL5 \rightarrow HVAL5$	0.458	1.10e-05	6.39e-06	19	0	439	19	0	0	5390	4009

Supplemental Table 24. Estimated marginal means of linear trends for the effect of in vivo signal correlation on $N_{syn}/mm\ L_d$ in different projection types across brain areas and layers. z and p-value are the z statistics and p-value of the marginal mean linear trends estimated from the fitted GLMMs. adjusted p-value is the adjusted p value through the BH multicomparison correction procedure.

Projection type	Coefficient	adjusted p-value	p-value	# of presynaptic neurons	# of postsynaptic neurons	# of ADP control neurons	# of same region control neurons	# of synapses	# of pre-post pairs	# of pre-ADP pairs	# of pre-'same region' pairs
$V1L2/3 \rightarrow V1L2/3$	1.110	2.08e-06	1.73e-07	20	604	2670	0	792	736	21247	0
$V1L2/3 \rightarrow V1L4$	0.617	1.33e-01	8.35e-02	19	197	2090	0	235	219	14010	0
$V1L2/3 \rightarrow V1L5$	1.820	3.11e-19	1.29e-20	20	311	1185	0	687	539	12384	0
$V1L2/3 \rightarrow HVAL2/3$	0.618	2.18e-01	1.54e-01	15	176	1169	0	208	196	4806	0
$V1L2/3 \rightarrow HVAL4$	1.080	1.33e-01	8.90e-02	14	80	856	0	89	82	3284	0
$V1L2/3 \rightarrow HVAL5$	1.225	3.34e-02	1.81e-02	13	91	429	0	131	106	2550	0
$V1L4 \rightarrow V1L2/3$	0.674	2.20e-01	1.65e-01	6	108	1784	0	120	110	3217	0
$V1L4 \rightarrow V1L4$	1.162	1.10e-02	4.57e-03	6	141	1865	0	155	146	4649	0
$V1L4 \rightarrow V1L5$	1.759	4.71e-05	7.85e-06	6	101	1138	0	130	110	3475	0
$V1L5 \rightarrow V1L4$	-1.058	2.24e-01	1.78e-01	6	64	1769	0	65	64	4044	0
$V1L5 \rightarrow V1L5$	0.916	2.64e-02	1.21e-02	6	103	1145	0	121	104	3825	0
$HVAL2/3 \rightarrow V1L2/3$	0.880	8.21e-03	3.08e-03	36	381	2626	0	436	411	13081	0
$HVAL2/3 \rightarrow V1L4$	1.346	6.96e-02	4.06e-02	28	79	1882	0	88	81	5203	0
$HVAL2/3 \rightarrow V1L5$	1.378	4.12e-05	5.16e-06	59	213	1172	0	324	278	13244	0
$HVAL2/3 \rightarrow HVAL2/3$	-0.083	7.29e-01	6.98e-01	45	519	1264	0	801	732	19926	0
$HVAL2/3 \rightarrow HVAL4$	1.223	4.13e-04	1.03e-04	38	204	893	0	301	258	13584	0
$HVAL2/3 \rightarrow HVAL5$	1.188	5.20e-05	1.08e-05	62	216	439	0	410	361	13812	0
$HVAL4 \rightarrow HVAL2/3$	0.843	3.34e-02	1.70e-02	12	259	1233	0	334	316	6215	0
$HVAL4 \rightarrow HVAL4$	1.349	8.21e-03	2.89e-03	12	138	893	0	174	155	5421	0
$HVAL4 \rightarrow HVAL5$	1.836	4.71e-03	1.37e-03	11	89	434	0	108	97	3089	0
$HVAL5 \rightarrow V1L5$	-0.416	6.32e-01	5.79e-01	14	59	1093	0	67	62	3601	0
$HVAL5 \rightarrow HVAL2/3$	0.094	8.17e-01	8.17e-01	17	260	1236	0	331	308	7872	0
$HVAL5 \rightarrow HVAL4$	0.672	3.11e-01	2.62e-01	17	92	896	0	110	102	6212	0
$HVAL5 \rightarrow HVAL5$	0.460	3.11e-01	2.72e-01	19	148	439	0	214	196	5586	0

Supplemental Table 25. Estimated marginal means of linear trends for the effect of in silico signal correlation on L_d / neuron pair (synapses excluded) in different projection types across brain areas and layers. z and p-value are the z statistics and p-value of the marginal mean linear trends estimated from the fitted GLMMs. adjusted p-value is the adjusted p value through the BH multicomparison correction procedure.

Projection type	Coefficient	adjusted p-value	p-value	# of presynaptic neurons	# of postsynaptic neurons	# of ADP control neurons	# of same region control neurons	# of synapses	# of pre-post pairs	# of pre-ADP pairs	# of pre-'same region' pairs
$V1L2/3 \rightarrow V1L2/3$	1.692	6.20e-109	5.17e-110	20	0	2670	20	0	0	20511	44349
$V1L2/3 \rightarrow V1L4$	0.632	9.58e-10	5.19e-10	19	0	2090	19	0	0	13791	32623
$V1L2/3 \rightarrow V1L5$	0.929	1.39e-17	5.23e-18	20	0	1185	20	0	0	11845	14652
$V1L2/3 \rightarrow HVAL2/3$	2.276	5.44e-33	9.06e-34	15	0	1169	15	0	0	4610	18075
$V1L2/3 \rightarrow HVAL4$	1.520	4.26e-10	2.13e-10	14	0	856	14	0	0	3202	10900
$V1L2/3 \rightarrow HVAL5$	0.738	5.58e-03	4.65e-03	13	0	429	13	0	0	2444	4028
$V1L4 \rightarrow V1L2/3$	0.551	7.48e-03	6.54e-03	6	0	1784	6	0	0	3107	16451
$V1L4 \rightarrow V1L4$	0.525	1.65e-03	1.25e-03	6	0	1865	6	0	0	4503	10073
$V1L4 \rightarrow V1L5$	0.538	1.65e-03	1.31e-03	6	0	1138	6	0	0	3365	4636
$V1L5 \rightarrow V1L4$	0.491	7.49e-03	6.87e-03	6	0	1769	6	0	0	3980	10686
$V1L5 \rightarrow V1L5$	0.546	8.97e-04	5.98e-04	6	0	1145	6	0	0	3721	4280
$HVAL2/3 \rightarrow V1L2/3$	-0.020	8.30e-01	8.30e-01	36	0	2626	36	0	0	12670	104893
$HVAL2/3 \rightarrow V1L4$	0.473	1.45e-03	1.03e-03	28	0	1882	28	0	0	5122	63511
$HVAL2/3 \rightarrow V1L5$	0.973	7.73e-29	1.61e-29	59	0	1172	59	0	0	12966	66476
$HVAL2/3 \rightarrow HVAL2/3$	2.087	3.32e-246	1.38e-247	45	0	1264	45	0	0	19194	48691
$HVAL2/3 \rightarrow HVAL4$	1.410	2.16e-69	2.70e-70	38	0	893	38	0	0	13326	24937
$HVAL2/3 \rightarrow HVAL5$	0.116	1.45e-01	1.39e-01	62	0	439	62	0	0	13451	17560
$HVAL4 \rightarrow HVAL2/3$	1.264	2.34e-22	6.83e-23	12	0	1233	12	0	0	5899	12092
$HVAL4 \rightarrow HVAL4$	0.975	1.87e-13	8.58e-14	12	0	893	12	0	0	5266	6729
$HVAL4 \rightarrow HVAL5$	0.631	1.69e-04	1.05e-04	11	0	434	11	0	0	2992	2477
$HVAL5 \rightarrow V1L5$	0.873	5.35e-07	3.12e-07	14	0	1093	14	0	0	3539	15315
$HVAL5 \rightarrow HVAL2/3$	1.266	3.38e-24	8.45e-25	17	0	1236	17	0	0	7564	18063
$HVAL5 \rightarrow HVAL4$	1.146	1.40e-16	5.83e-17	17	0	896	17	0	0	6110	11017
$HVAL5 \rightarrow HVAL5$	1.215	9.66e-22	3.22e-22	19	0	439	19	0	0	5390	4009

Supplemental Table 26. Estimated marginal means of linear trends for the effect of in silico signal correlation on $N_{syn}/mm\ L_d$ in different projection types across brain areas and layers. z and p-value are the z statistics and p-value of the marginal mean linear trends estimated from the fitted GLMMs. adjusted p-value is the adjusted p value through the BH multicomparison correction procedure.

Projection type	Coefficient	adjusted p-value	p-value	# of presynaptic neurons	# of postsynaptic neurons	# of ADP control neurons	# of same region control neurons	# of synapses	# of pre-post pairs	# of pre-ADP pairs	# of pre-'same region' pairs
$V1L2/3 \rightarrow V1L2/3$	2.026	2.87e-09	3.58e-10	20	604	2670	0	792	736	21247	0
$V1L2/3 \rightarrow V1L4$	2.973	1.67e-07	3.47e-08	19	197	2090	0	235	219	14010	0
$V1L2/3 \rightarrow V1L5$	4.022	1.75e-39	7.29e-41	20	311	1185	0	687	539	12384	0
$V1L2/3 \rightarrow HVAL2/3$	0.808	3.52e-01	2.93e-01	15	176	1169	0	208	196	4806	0
$V1L2/3 \rightarrow HVAL4$	2.167	9.18e-02	6.12e-02	14	80	856	0	89	82	3284	0
$V1L2/3 \rightarrow HVAL5$	3.941	3.48e-06	1.16e-06	13	91	429	0	131	106	2550	0
$V1L4 \rightarrow V1L2/3$	1.097	2.48e-01	1.86e-01	6	108	1784	0	120	110	3217	0
$V1L4 \rightarrow V1L4$	2.180	5.08e-04	1.90e-04	6	141	1865	0	155	146	4649	0
$V1L4 \rightarrow V1L5$	3.194	7.21e-09	1.20e-09	6	101	1138	0	130	110	3475	0
$V1L5 \rightarrow V1L4$	-1.271	3.52e-01	2.87e-01	6	64	1769	0	65	64	4044	0
$V1L5 \rightarrow V1L5$	1.508	5.43e-02	2.94e-02	6	103	1145	0	121	104	3825	0
$HVAL2/3 \rightarrow V1L2/3$	0.837	9.18e-02	5.90e-02	36	381	2626	0	436	411	13081	0
$HVAL2/3 \rightarrow V1L4$	1.304	2.15e-01	1.52e-01	28	79	1882	0	88	81	5203	0
$HVAL2/3 \rightarrow V1L5$	2.730	1.70e-10	1.42e-11	59	213	1172	0	324	278	13244	0
$HVAL2/3 \rightarrow HVAL2/3$	-0.108	7.41e-01	7.19e-01	45	519	1264	0	801	732	19926	0
$HVAL2/3 \rightarrow HVAL4$	1.585	9.99e-04	4.16e-04	38	204	893	0	301	258	13584	0
$HVAL2/3 \rightarrow HVAL5$	1.834	2.24e-06	5.61e-07	62	216	439	0	410	361	13812	0
$HVAL4 \rightarrow HVAL2/3$	1.203	2.36e-02	1.18e-02	12	259	1233	0	334	316	6215	0
$HVAL4 \rightarrow HVAL4$	2.515	2.28e-06	6.64e-07	12	138	893	0	174	155	5421	0
$HVAL4 \rightarrow HVAL5$	2.154	5.01e-03	2.30e-03	11	89	434	0	108	97	3089	0
$HVAL5 \rightarrow V1L5$	1.878	8.64e-02	5.04e-02	14	59	1093	0	67	62	3601	0
$HVAL5 \rightarrow HVAL2/3$	0.308	5.91e-01	5.17e-01	17	260	1236	0	331	308	7872	0
$HVAL5 \rightarrow HVAL4$	0.248	7.41e-01	7.41e-01	17	92	896	0	110	102	6212	0
$HVAL5 \rightarrow HVAL5$	0.313	6.00e-01	5.50e-01	19	148	439	0	214	196	5586	0

Supplemental Table 27. Estimated marginal means of linear trends for the effect of feature weight similarity on L_d / neuron pair (synapses excluded) in different projection types across brain areas and layers. z and p-value are the z statistics and p-value of the marginal mean linear trends estimated from the fitted GLMMs. adjusted p-value is the adjusted p value through the BH multicomparison correction procedure.

Projection type	Coefficient	adjusted p-value	p-value	# of presynaptic neurons	# of postsynaptic neurons	# of ADP control neurons	# of same region control neurons	# of synapses	# of pre-post pairs	# of pre-ADP pairs	# of pre-'same region' pairs
$V1L2/3 \rightarrow V1L2/3$	1.005	8.41e-38	1.05e-38	20	0	2670	20	0	0	20511	44349
$V1L2/3 \rightarrow V1L4$	0.512	9.17e-07	4.59e-07	19	0	2090	19	0	0	13791	32623
$V1L2/3 \rightarrow V1L5$	0.602	8.40e-08	3.85e-08	20	0	1185	20	0	0	11845	14652
$V1L2/3 \rightarrow HVAL2/3$	0.849	1.12e-05	6.97e-06	15	0	1169	15	0	0	4610	18075
$V1L2/3 \rightarrow HVAL4$	0.804	1.27e-03	9.01e-04	14	0	856	14	0	0	3202	10900
$V1L2/3 \rightarrow HVAL5$	0.410	1.34e-01	1.28e-01	13	0	429	13	0	0	2444	4028
$V1L4 \rightarrow V1L2/3$	0.257	2.09e-01	2.09e-01	6	0	1784	6	0	0	3107	16451
$V1L4 \rightarrow V1L4$	0.769	1.79e-06	9.70e-07	6	0	1865	6	0	0	4503	10073
$V1L4 \rightarrow V1L5$	0.663	2.60e-04	1.73e-04	6	0	1138	6	0	0	3365	4636
$V1L5 \rightarrow V1L4$	0.465	1.66e-02	1.25e-02	6	0	1769	6	0	0	3980	10686
$V1L5 \rightarrow V1L5$	0.361	3.27e-02	2.87e-02	6	0	1145	6	0	0	3721	4280
$HVAL2/3 \rightarrow V1L2/3$	0.251	2.75e-02	2.17e-02	36	0	2626	36	0	0	12670	104893
$HVAL2/3 \rightarrow V1L4$	0.378	3.17e-02	2.64e-02	28	0	1882	28	0	0	5122	63511
$HVAL2/3 \rightarrow V1L5$	1.078	5.07e-22	1.06e-22	59	0	1172	59	0	0	12966	66476
$HVAL2/3 \rightarrow HVAL2/3$	2.692	3.67e-248	1.53e-249	45	0	1264	45	0	0	19194	48691
$HVAL2/3 \rightarrow HVAL4$	2.013	5.69e-83	4.74e-84	38	0	893	38	0	0	13326	24937
$HVAL2/3 \rightarrow HVAL5$	0.885	1.56e-17	5.20e-18	62	0	439	62	0	0	13451	17560
$HVAL4 \rightarrow HVAL2/3$	1.560	2.27e-24	3.78e-25	12	0	1233	12	0	0	5899	12092
$HVAL4 \rightarrow HVAL4$	1.436	1.03e-21	2.57e-22	12	0	893	12	0	0	5266	6729
$HVAL4 \rightarrow HVAL5$	0.884	2.15e-06	1.25e-06	11	0	434	11	0	0	2992	2477
$HVAL5 \rightarrow V1L5$	1.169	1.05e-09	4.38e-10	14	0	1093	14	0	0	3539	15315
$HVAL5 \rightarrow HVAL2/3$	0.273	6.10e-02	5.59e-02	17	0	1236	17	0	0	7564	18063
$HVAL5 \rightarrow HVAL4$	1.195	3.89e-14	1.46e-14	17	0	896	17	0	0	6110	11017
$HVAL5 \rightarrow HVAL5$	1.306	1.37e-19	3.99e-20	19	0	439	19	0	0	5390	4009

Supplemental Table 28. Estimated marginal means of linear trends for the effect of feature weight similarity on $N_{syn}/mm\ L_d$ in different projection types across brain areas and layers. z and p-value are the z statistics and p-value of the marginal mean linear trends estimated from the fitted GLMMs. adjusted p-value is the adjusted p value through the BH multicomparison correction procedure.

Projection type	Coefficient	adjusted p-value	p-value	# of presynaptic neurons	# of postsynaptic neurons	# of ADP control neurons	# of same region control neurons	# of synapses	# of pre-post pairs	# of pre-ADP pairs	# of pre-'same region' pairs
$V1L2/3 \rightarrow V1L2/3$	1.840	6.63e-07	1.11e-07	20	604	2670	0	792	736	21247	0
$V1L2/3 \rightarrow V1L4$	2.015	3.78e-03	1.57e-03	19	197	2090	0	235	219	14010	0
$V1L2/3 \rightarrow V1L5$	3.855	1.05e-25	4.39e-27	20	311	1185	0	687	539	12384	0
$V1L2/3 \rightarrow HVAL2/3$	0.715	3.77e-01	3.45e-01	15	176	1169	0	208	196	4806	0
$V1L2/3 \rightarrow HVAL4$	-0.143	9.04e-01	9.04e-01	14	80	856	0	89	82	3284	0
$V1L2/3 \rightarrow HVAL5$	3.330	4.87e-04	1.83e-04	13	91	429	0	131	106	2550	0
$V1L4 \rightarrow V1L2/3$	1.005	3.28e-01	2.59e-01	6	108	1784	0	120	110	3217	0
$V1L4 \rightarrow V1L4$	2.416	4.52e-04	1.51e-04	6	141	1865	0	155	146	4649	0
$V1L4 \rightarrow V1L5$	4.052	8.61e-08	7.18e-09	6	101	1138	0	130	110	3475	0
$V1L5 \rightarrow V1L4$	-1.410	3.11e-01	2.33e-01	6	64	1769	0	65	64	4044	0
$V1L5 \rightarrow V1L5$	0.304	7.36e-01	7.05e-01	6	103	1145	0	121	104	3825	0
$HVAL2/3 \rightarrow V1L2/3$	1.248	3.23e-02	1.89e-02	36	381	2626	0	436	411	13081	0
$HVAL2/3 \rightarrow V1L4$	3.178	8.70e-03	4.35e-03	28	79	1882	0	88	81	5203	0
$HVAL2/3 \rightarrow V1L5$	3.210	1.28e-07	1.59e-08	59	213	1172	0	324	278	13244	0
$HVAL2/3 \rightarrow HVAL2/3$	0.351	3.77e-01	3.44e-01	45	519	1264	0	801	732	19926	0
$HVAL2/3 \rightarrow HVAL4$	2.861	7.44e-06	1.86e-06	38	204	893	0	301	258	13584	0
$HVAL2/3 \rightarrow HVAL5$	2.452	3.18e-06	6.63e-07	62	216	439	0	410	361	13812	0
$HVAL4 \rightarrow HVAL2/3$	1.416	2.23e-02	1.21e-02	12	259	1233	0	334	316	6215	0
$HVAL4 \rightarrow HVAL4$	2.614	1.54e-04	4.51e-05	12	138	893	0	174	155	5421	0
$HVAL4 \rightarrow HVAL5$	2.486	8.70e-03	4.12e-03	11	89	434	0	108	97	3089	0
$HVAL5 \rightarrow V1L5$	1.423	2.89e-01	2.05e-01	14	59	1093	0	67	62	3601	0
$HVAL5 \rightarrow HVAL2/3$	0.794	2.51e-01	1.67e-01	17	260	1236	0	331	308	7872	0
$HVAL5 \rightarrow HVAL4$	-0.926	3.54e-01	2.95e-01	17	92	896	0	110	102	6212	0
$HVAL5 \rightarrow HVAL5$	1.090	1.09e-01	6.81e-02	19	148	439	0	214	196	5586	0

Supplemental Table 29. Estimated marginal means of linear trends for the effect of receptive field center distance on L_d / neuron pair (synapses excluded) in different projection types across brain areas and layers. z and p-value are the z statistics and p-value of the marginal mean linear trends estimated from the fitted GLMMs. adjusted p-value is the adjusted p value through the BH multicomparison correction procedure.

Projection type	Coefficient	adjusted p-value	p-value	# of presynaptic neurons	# of postsynaptic neurons	# of ADP control neurons	# of same region control neurons	# of synapses	# of pre-post pairs	# of pre-ADP pairs	# of pre-'same region' pairs
$V1L2/3 \rightarrow V1L2/3$	-0.167	0.00e+00	0.00e+00	20	0	2670	20	0	0	20511	44349
$V1L2/3 \rightarrow V1L4$	-0.141	0.00e+00	0.00e+00	19	0	2090	19	0	0	13791	32623
$V1L2/3 \rightarrow V1L5$	-0.111	0.00e+00	0.00e+00	20	0	1185	20	0	0	11845	14652
$V1L2/3 \rightarrow HVAL2/3$	-0.032	7.39e-21	6.16e-21	15	0	1169	15	0	0	4610	18075
$V1L2/3 \rightarrow HVAL4$	-0.030	5.27e-14	4.83e-14	14	0	856	14	0	0	3202	10900
$V1L2/3 \rightarrow HVAL5$	-0.014	4.94e-03	4.94e-03	13	0	429	13	0	0	2444	4028
$V1L4 \rightarrow V1L2/3$	-0.097	1.11e-68	7.42e-69	6	0	1784	6	0	0	3107	16451
$V1L4 \rightarrow V1L4$	-0.136	1.76e-189	5.14e-190	6	0	1865	6	0	0	4503	10073
$V1L4 \rightarrow V1L5$	-0.134	8.03e-134	4.01e-134	6	0	1138	6	0	0	3365	4636
$V1L5 \rightarrow V1L4$	-0.053	2.71e-27	2.14e-27	6	0	1769	6	0	0	3980	10686
$V1L5 \rightarrow V1L5$	-0.092	1.19e-80	7.44e-81	6	0	1145	6	0	0	3721	4280
$HVAL2/3 \rightarrow V1L2/3$	-0.015	7.37e-11	7.06e-11	36	0	2626	36	0	0	12670	104893
$HVAL2/3 \rightarrow V1L4$	-0.031	1.82e-16	1.60e-16	28	0	1882	28	0	0	5122	63511
$HVAL2/3 \rightarrow V1L5$	-0.035	1.25e-46	9.39e-47	59	0	1172	59	0	0	12966	66476
$HVAL2/3 \rightarrow HVAL2/3$	-0.099	0.00e+00	0.00e+00	45	0	1264	45	0	0	19194	48691
$HVAL2/3 \rightarrow HVAL4$	-0.083	0.00e+00	0.00e+00	38	0	893	38	0	0	13326	24937
$HVAL2/3 \rightarrow HVAL5$	-0.047	1.41e-112	7.63e-113	62	0	439	62	0	0	13451	17560
$HVAL4 \rightarrow HVAL2/3$	-0.084	4.83e-169	1.81e-169	12	0	1233	12	0	0	5899	12092
$HVAL4 \rightarrow HVAL4$	-0.093	2.33e-215	5.82e-216	12	0	893	12	0	0	5266	6729
$HVAL4 \rightarrow HVAL5$	-0.109	5.56e-172	1.85e-172	11	0	434	11	0	0	2992	2477
$HVAL5 \rightarrow V1L5$	-0.067	3.07e-53	2.18e-53	14	0	1093	14	0	0	3539	15315
$HVAL5 \rightarrow HVAL2/3$	-0.052	3.63e-86	2.12e-86	17	0	1236	17	0	0	7564	18063
$HVAL5 \rightarrow HVAL4$	-0.071	8.03e-134	3.74e-134	17	0	896	17	0	0	6110	11017
$HVAL5 \rightarrow HVAL5$	-0.082	4.99e-159	2.08e-159	19	0	439	19	0	0	5390	4009

Supplemental Table 30. Estimated marginal means of linear trends for the effect of receptive field center distance on N_{syn}/mm L_d in different projection types across brain areas and layers. z and p-value are the z statistics and p-value of the marginal mean linear trends estimated from the fitted GLMMs. adjusted p-value is the adjusted p value through the BH multicomparison correction procedure.

Projection type	Coefficient	adjusted p-value	p-value	# of presynaptic neurons	# of postsynaptic neurons	# of ADP control neurons	# of same region control neurons	# of synapses	# of pre-post pairs	# of pre-ADP pairs	# of pre-'same region' pairs
$V1L2/3 \rightarrow V1L2/3$	0.020	2.56e-01	4.26e-02	20	604	2670	0	792	736	21247	0
$V1L2/3 \rightarrow V1L4$	0.050	5.19e-02	2.16e-03	19	197	2090	0	235	219	14010	0
$V1L2/3 \rightarrow V1L5$	0.012	5.26e-01	2.27e-01	20	311	1185	0	687	539	12384	0
$V1L2/3 \rightarrow HVAL2/3$	0.008	8.34e-01	6.26e-01	15	176	1169	0	208	196	4806	0
$V1L2/3 \rightarrow HVAL4$	0.014	8.18e-01	5.11e-01	14	80	856	0	89	82	3284	0
$V1L2/3 \rightarrow HVAL5$	0.001	9.50e-01	9.50e-01	13	91	429	0	131	106	2550	0
$V1L4 \rightarrow V1L2/3$	0.020	8.10e-01	4.59e-01	6	108	1784	0	120	110	3217	0
$V1L4 \rightarrow V1L4$	0.060	6.82e-02	5.69e-03	6	141	1865	0	155	146	4649	0
$V1L4 \rightarrow V1L5$	0.042	3.98e-01	8.30e-02	6	101	1138	0	130	110	3475	0
$V1L5 \rightarrow V1L4$	-0.016	8.34e-01	6.22e-01	6	64	1769	0	65	64	4044	0
$V1L5 \rightarrow V1L5$	0.034	5.26e-01	2.02e-01	6	103	1145	0	121	104	3825	0
$HVAL2/3 \rightarrow V1L2/3$	-0.015	5.26e-01	2.19e-01	36	381	2626	0	436	411	13081	0
$HVAL2/3 \rightarrow V1L4$	0.004	9.39e-01	8.88e-01	28	79	1882	0	88	81	5203	0
$HVAL2/3 \rightarrow V1L5$	-0.020	5.26e-01	1.37e-01	59	213	1172	0	324	278	13244	0
$HVAL2/3 \rightarrow HVAL2/3$	0.004	8.49e-01	6.74e-01	45	519	1264	0	801	732	19926	0
$HVAL2/3 \rightarrow HVAL4$	-0.002	9.39e-01	8.99e-01	38	204	893	0	301	258	13584	0
$HVAL2/3 \rightarrow HVAL5$	-0.004	8.49e-01	7.08e-01	62	216	439	0	410	361	13812	0
$HVAL4 \rightarrow HVAL2/3$	0.013	5.26e-01	2.41e-01	12	259	1233	0	334	316	6215	0
$HVAL4 \rightarrow HVAL4$	0.014	6.51e-01	3.26e-01	12	138	893	0	174	155	5421	0
$HVAL4 \rightarrow HVAL5$	0.048	1.25e-01	1.57e-02	11	89	434	0	108	97	3089	0
$HVAL5 \rightarrow V1L5$	0.016	8.34e-01	5.74e-01	14	59	1093	0	67	62	3601	0
$HVAL5 \rightarrow HVAL2/3$	0.008	8.10e-01	4.72e-01	17	260	1236	0	331	308	7872	0
$HVAL5 \rightarrow HVAL4$	0.021	5.26e-01	2.11e-01	17	92	896	0	110	102	6212	0
$HVAL5 \rightarrow HVAL5$	-0.004	8.78e-01	7.69e-01	19	148	439	0	214	196	5586	0

Supplemental Table 31. Estimated marginal means of linear trends for the effect of in silico ΔOri on L_d / neuron pair (synapses excluded) in different projection types across brain areas and layers. z and p-value are the z statistics and p-value of the marginal mean linear trends estimated from the fitted GLMMs. adjusted p-value is the adjusted p value through the BH multicomparison correction procedure.

Projection type	Coefficient	adjusted p-value	p-value	# of presynaptic neurons	# of postsynaptic neurons	# of ADP control neurons	# of same region control neurons	# of synapses	# of pre-post pairs	# of pre-ADP pairs	# of pre-'same region' pairs
$V1L2/3 \rightarrow V1L2/3$	-0.003	1.22e-10	7.61e-12	12	0	1409	12	0	0	6927	14702
$V1L2/3 \rightarrow V1L4$	-0.004	3.52e-07	4.40e-08	9	0	1050	9	0	0	4190	7845
$V1L2/3 \rightarrow V1L5$	-0.001	5.15e-01	3.22e-01	12	0	701	12	0	0	4527	4791
$V1L2/3 \rightarrow HVAL2/3$	-0.006	3.69e-06	6.93e-07	7	0	487	7	0	0	1354	3258
$V1L2/3 \rightarrow HVAL5$	-0.003	9.32e-02	4.21e-02	8	0	224	8	0	0	786	1249
$HVAL2/3 \rightarrow V1L2/3$	0.003	4.97e-04	1.24e-04	20	0	1299	20	0	0	4401	31930
$HVAL2/3 \rightarrow V1L4$	-0.000	9.42e-01	9.42e-01	16	0	885	16	0	0	1706	19798
$HVAL2/3 \rightarrow V1L5$	0.001	9.32e-02	4.66e-02	30	0	689	30	0	0	4433	19345
$HVAL2/3 \rightarrow HVAL2/3$	0.000	8.54e-01	7.47e-01	17	0	557	17	0	0	4103	7038
$HVAL2/3 \rightarrow HVAL4$	0.000	8.41e-01	6.83e-01	16	0	397	16	0	0	2812	4472
$HVAL2/3 \rightarrow HVAL5$	-0.001	4.10e-01	2.31e-01	27	0	229	27	0	0	3420	3482
$HVAL4 \rightarrow HVAL2/3$	-0.001	6.16e-01	4.24e-01	7	0	499	7	0	0	1262	3344
$HVAL4 \rightarrow HVAL5$	-0.000	8.41e-01	6.74e-01	7	0	225	7	0	0	937	848
$HVAL5 \rightarrow V1L5$	0.000	9.42e-01	9.22e-01	9	0	603	9	0	0	1414	5725
$HVAL5 \rightarrow HVAL2/3$	0.002	2.94e-02	9.20e-03	12	0	541	12	0	0	2307	5594
$HVAL5 \rightarrow HVAL5$	-0.002	9.32e-02	4.49e-02	14	0	228	14	0	0	2125	1430

Supplemental Table 32. Estimated marginal means of linear trends for the effect of in silico ΔOri on $N_{syn}/mm\ L_d$ in different projection types across brain areas and layers. z and p-value are the z statistics and p-value of the marginal mean linear trends estimated from the fitted GLMMs. adjusted p-value is the adjusted p value through the BH multicomparison correction procedure.

Projection type	Coefficient	adjusted p-value	p-value	# of presynaptic neurons	# of postsynaptic neurons	# of ADP control neurons	# of same region control neurons	# of synapses	# of pre-post pairs	# of pre-ADP pairs	# of pre-'same region' pairs
$V1L2/3 \rightarrow V1L2/3$	-0.003	4.73e-01	1.80e-01	12	246	1409	0	296	272	7199	0
$V1L2/3 \rightarrow V1L4$	0.005	4.73e-01	1.82e-01	9	82	1050	0	91	83	4273	0
$V1L2/3 \rightarrow V1L5$	-0.009	1.66e-03	1.04e-04	12	165	701	0	323	245	4772	0
$V1L2/3 \rightarrow HVAL2/3$	0.001	8.89e-01	8.89e-01	7	52	487	0	54	53	1407	0
$V1L2/3 \rightarrow HVAL5$	-0.014	8.07e-02	1.01e-02	8	38	224	0	51	40	826	0
$HVAL2/3 \rightarrow V1L2/3$	-0.004	4.73e-01	2.37e-01	20	123	1299	0	134	129	4530	0
$HVAL2/3 \rightarrow V1L4$	-0.012	4.04e-01	7.57e-02	16	33	885	0	36	33	1739	0
$HVAL2/3 \rightarrow V1L5$	-0.002	7.20e-01	6.06e-01	30	97	689	0	123	109	4542	0
$HVAL2/3 \rightarrow HVAL2/3$	-0.001	7.20e-01	6.07e-01	17	145	557	0	192	177	4280	0
$HVAL2/3 \rightarrow HVAL4$	0.002	7.31e-01	6.85e-01	16	59	397	0	70	67	2879	0
$HVAL2/3 \rightarrow HVAL5$	0.004	4.73e-01	2.07e-01	27	80	229	0	122	106	3526	0
$HVAL4 \rightarrow HVAL2/3$	0.005	5.95e-01	3.35e-01	7	55	499	0	59	59	1321	0
$HVAL4 \rightarrow HVAL5$	-0.009	4.73e-01	1.49e-01	7	29	225	0	32	30	967	0
$HVAL5 \rightarrow V1L5$	-0.003	7.20e-01	6.30e-01	9	25	603	0	31	26	1440	0
$HVAL5 \rightarrow HVAL2/3$	-0.002	7.20e-01	5.38e-01	12	87	541	0	106	98	2405	0
$HVAL5 \rightarrow HVAL5$	-0.004	6.13e-01	3.83e-01	14	56	228	0	71	67	2192	0

Supplemental Table 33. Paired t-tests for comparing the mean presyn-postsyn functional similarity between observation in the MICrONS dataset and values expected by GLMMs fit on the MICrONS dataset

Projection type	Comparison	t-statistic	p-value	adjusted p-value
$HVA \to HVA$	observed vs expected	660.0	7.92e-01	9.81e-01
$HVA \to V1$	observed vs expected	362.0	9.09e-01	9.81e-01
$V1 \to HVA$	observed vs expected	62.0	5.17e-01	9.81e-01
$V1 \to V1$	observed vs expected	313.0	9.81e-01	9.81e-01
$HVA \to HVA$	observed vs expected (synaptic scale)	675.0	8.99e-01	9.81e-01
$HVA \to V1$	observed vs expected (synaptic scale)	349.0	7.63e-01	9.81e-01
$V1 \to HVA$	observed vs expected (synaptic scale)	71.0	8.18e-01	9.81e-01
$V1 \to V1$	observed vs expected (synaptic scale)	280.0	5.76e-01	9.81e-01
$HVA \to HVA$	observed vs expected (axonal scale)	629.0	5.85e-01	9.81e-01
$HVA \to V1$	observed vs expected (axonal scale)	349.0	7.63e-01	9.81e-01
$V1 \to HVA$	observed vs expected (axonal scale)	63.0	5.48e-01	9.81e-01
$V1 \to V1$	observed vs expected (axonal scale)	284.0	6.22e-01	9.81e-01

Supplemental Table 34. Paired t-tests for comparing the mean postsyn-postsyn functional similarity between observation in the MICrONS dataset and values expected by GLMMs fit on the MICrONS dataset

Projection type	Comparison	t-statistic	p-value	adjusted p-value
$HVA \to HVA$	observed vs expected	254.0	7.45e-05	1.79e-04
$HVA \to V1$	observed vs expected	46.0	1.39e-07	5.56e-07
$V1 \to HVA$	observed vs expected	53.0	2.84e-01	2.84e-01
$V1 \to V1$	observed vs expected	45.0	9.74e-07	2.92e-06
$HVA \to HVA$	observed vs expected (synaptic scale)	344.0	1.68e-03	2.52e-03
$HVA \to V1$	observed vs expected (synaptic scale)	125.0	2.00e-04	3.99e-04
$V1 \to HVA$	observed vs expected (synaptic scale)	32.0	3.48e-02	4.64e-02
$V1 \to V1$	observed vs expected (synaptic scale)	197.0	5.35e-02	6.42e-02
$HVA \to HVA$	observed vs expected (axonal scale)	344.0	1.68e-03	2.52e-03
$HVA \to V1$	observed vs expected (axonal scale)	19.0	2.23e-09	1.34e-08
$V1 \to HVA$	observed vs expected (axonal scale)	53.0	2.84e-01	2.84e-01
$V1 \to V1$	observed vs expected (axonal scale)	5.0	5.82e-10	6.98e-09